

**Attenuated Alpha Backgrounds in the DEAP-3600  
Dark Matter Search Experiment**

By

**Phillip DelGobbo**

A thesis submitted to the Faculty of Graduate and Postdoctoral Affairs  
in partial fulfillment of the requirements for the degree of

**Master of Science**

in

Particle Physics

Department of Physics

Carleton University

Ottawa, Ontario, Canada

©2021

Phillip DelGobbo

# Abstract

DEAP-3600 is a dark matter experiment using 3.3 tonnes of liquid argon as a scintillation target to directly detect Weakly Interacting Massive Particles (WIMPs), a dark matter candidate. Mitigating background sources is crucial to dark matter searches. A large background model contribution comes from attenuated alphas originating from  $^{210}\text{Po}$  decays within the acrylic vessel surfaces. Alphas from decays within the acrylic inner vessel and from the acrylic neck flowguide are analyzed. The activity of the inner vessel is separated into surface and bulk components, and determined to be  $0.22 \pm 0.02$  mBq/m<sup>2</sup> and  $3.68 \pm 0.06$  mBq. An event rate of  $53.5_{-4.6}^{+30}$   $\mu\text{Hz}$  is found for alphas originating from the neck flowguide. An optimized event selection is obtained, making use of machine-learning algorithms to reject neck flowguide alphas and maximize WIMP sensitivity. In 802 live-days of DEAP-3600 data, the expected upper limit on the spin-independent WIMP-nucleon interaction cross-section is  $1.9 \times 10^{-45}$  cm<sup>2</sup> (90% C.L.) for a 100 GeV/c<sup>2</sup> WIMP mass.

# Acknowledgements

This thesis is not possible without the support of those around me. Long nights of analysis and writing were made easier by the physics help provided by the DEAP collaboration, and the emotional help provided by my friends and family. I wish I could do more to show my gratitude to all of you, but a couple pages of rambling will have to suffice.

First and foremost I would like to thank Dr. Simon Viel, for providing me with this opportunity, but even more so for being such an incredible supervisor. His guidance over these last two years has been tremendous. No matter how busy he was with the array of other tasks, he always took time out to answer any questions I had, big or small, and his patience and kindness during this entire process did not go unnoticed.

I also owe a lot of thanks to other members of the DEAP Collaboration. Thank you to Alexey Grobov, who walked me through the MVA process, and kept me company at the pool table in Munich. Thanks to Guillaume Oliviero and Pushpa Adhikari for being so welcoming and patient with me as they taught me alpha analysis techniques. Finally thanks to David Gallacher, an incredible help with the alpha quenching work. I'm sure we would have had many more nights of drinks at Mike's Place if we were given the chance. And to the many many more people in the DEAP collaboration who answered my seemingly random questions on slack, thank you. I wish I could have gotten to know all of you better before we were all forced inside for 16 months. Despite this, you all treated me as a friend, and I am very grateful.

I would like to thank my friends outside of my work, Joe, Daniel and John. Weekly

D&D nights and mid-day Catan sessions kept me alive during this entire process, and this thesis would likely sound like the words of a madman without all three of you.

Most importantly, I want to thank my parents. I am incredibly lucky to have such supportive and caring parents, who were there for me through this whole process. You taught me how to put my full effort into my work, never give up, and be proud of my accomplishments. That knowledge is the most important lesson I have learned in my life. I will always be grateful for your unconditional love.

And to Shawna. It is incredible to me that you can somehow manage your own Masters, a full time job, and all of my nonsense, but you do, and I am grateful every day that you are with me. You are the rock in my life, and the first person I go to when I am excited or nervous. Now that we're both through, I can't wait to see what our life has in store.

# Contents

<b>Abstract</b>	<b>ii</b>
<b>Acknowledgements</b>	<b>iii</b>
<b>Contents</b>	<b>v</b>
<b>List of Tables</b>	<b>viii</b>
<b>List of Figures</b>	<b>x</b>
<b>Glossary</b>	<b>xiv</b>
<b>1 Introduction</b>	<b>1</b>
1.1 Evidence for Dark Matter . . . . .	1
1.2 WIMPs: A Dark Matter Candidate . . . . .	4
1.3 Dark Matter Detection . . . . .	7
1.4 Outline . . . . .	9
<b>2 DEAP-3600 Detector</b>	<b>11</b>
2.1 Scintillation in Noble Liquids . . . . .	11
2.2 DEAP-3600 Detector . . . . .	13
2.2.1 SNOLAB Facility . . . . .	14
2.2.2 Detector Design . . . . .	14

2.3	Pulseshape Discrimination . . . . .	21
<b>3</b>	<b>Background Sources in the DEAP-3600 Detector</b>	<b>25</b>
3.1	$^{39}\text{Ar}$ $\beta$ -Decays . . . . .	25
3.2	Cherenkov Radiation . . . . .	27
3.3	Radiogenic and Cosmogenic Neutrons . . . . .	27
3.4	Alphas . . . . .	28
3.4.1	From Acrylic Vessel Inner Surface and TPB Layer . . . . .	31
3.4.2	From Acrylic Neck Flowguide Surface . . . . .	31
3.4.3	From Dust Particulate Diffuse in LAr . . . . .	33
<b>4</b>	<b><math>\alpha</math>-Decays from the Inner Acrylic Vessel Surface and TPB Layer</b>	<b>35</b>
4.1	Activity Measurement . . . . .	35
4.1.1	Defining the Surface Alpha Control Region . . . . .	36
4.1.2	Activity Calculation . . . . .	40
4.2	Surface Alpha Positional Leakage . . . . .	50
4.2.1	Pentagonal Alphas . . . . .	51
4.2.2	Surface Leakage Measurement . . . . .	56
<b>5</b>	<b><math>\alpha</math>-Decays from the Neck Flowguide</b>	<b>62</b>
5.1	Control Regions and Fit . . . . .	63
5.2	Systematics on the Neck Alpha Trigger Rate . . . . .	70
<b>6</b>	<b>Impact on the Dark Matter Search</b>	<b>76</b>
6.1	Event Selection Optimization . . . . .	76
6.1.1	Event Selection Definition . . . . .	76
6.1.2	Introducing Multivariate Analysis . . . . .	82
6.1.3	Grid Scan . . . . .	86
6.1.4	New Event Selection Signal Acceptance . . . . .	91

6.2	Expected Alpha Background Yield in the DM Search ROI . . . . .	94
6.2.1	Neck Alpha Yield . . . . .	94
6.2.2	Dust Alpha Yield . . . . .	96
6.2.3	Surface Alpha Yield . . . . .	97
6.2.4	Summary and Exclusion Curves . . . . .	102
<b>7</b>	<b>Conclusion</b>	<b>105</b>
	<b>Bibliography</b>	<b>108</b>
<b>A</b>	<b>Appendix A Alpha Quenching in Liquid Argon</b>	<b>116</b>
A.1	Review of Alpha Quenching in LAr Scintillation Detectors . . . . .	116
A.2	Alpha Quenching in DEAP-3600 Simulations . . . . .	118
A.3	Fitting Birk's Constant to DEAP-3600 Alpha Data . . . . .	122
A.4	Validation and Summary . . . . .	124
<b>B</b>	<b>Appendix B Event Selection Optimization Heat Maps</b>	<b>127</b>
<b>C</b>	<b>Appendix C Systematic Variation Shape Analysis for Dust Alphas</b>	<b>131</b>

# List of Tables

4.1	Depth of $^{210}\text{Po}$ surface alpha components for simulations . . . . .	36
4.2	Definition of the surface alpha control region . . . . .	37
4.3	Component weights from $^{210}\text{Po}$ surface alpha fit . . . . .	44
4.4	Geometrical parameters of acrylic vessel and TPB layer necessary for activity calculation . . . . .	47
4.5	Activity calculation of different surface alpha components . . . . .	47
4.6	Surface alpha component trigger rates . . . . .	48
5.1	Definition of neck alpha preselection . . . . .	64
5.2	Definition of neck alpha control regions . . . . .	65
5.3	Neck alpha trigger rate compared to previous result . . . . .	72
6.1	Summary of trigger rates for all alpha sources . . . . .	77
6.2	Dark matter event selection for 231 liveday study . . . . .	78
6.3	Range of candidate values for event selection optimization . . . . .	86
6.4	Optimized event selection for each estimator, and combinations of two, sorted by sensitivity to $1 \text{ TeV}/c^2$ WIMP . . . . .	88
6.5	Contained mass calculations for new optimized event selection . . . . .	92
6.6	Signal acceptance for previous and optimized event selection . . . . .	93
6.7	Neck alpha estimates in the dark matter search region of interest . . . . .	96

6.8	Summary of alpha yields in dark matter search region of interest for 376 live days . . . . .	102
A.1	Measured quenching factor of high energy alpha decays in liquid argon	123

# List of Figures

1.1	Tangential velocity curve for NGC 6503 galaxy, showing need for dark matter to compensate for missing velocity . . . . .	2
1.2	Images of the Bullet cluster, a galaxy cluster merger, along with mass centers from measured gravitational lensing, and x-ray imaging . . . .	4
1.3	Parameter space of non-baryonic dark matter particle candidates . . .	6
1.4	Exclusion curves for various WIMP detection experiments . . . . .	8
1.5	Exclusion curves for some leading WIMP direct detection experiments	9
2.1	Map of the SNOLAB facilities . . . . .	14
2.2	Cross-section of DEAP-3600 detector design . . . . .	16
2.3	Flow chart of DEAP-3600 data acquisition system . . . . .	18
2.4	Fprompt distribution of events in the 120-200 PE range . . . . .	22
2.5	Dark matter region of interest from 231 liveday paper . . . . .	23
2.6	Fprompt:PE distribution of 4.4 live-day dataset . . . . .	24
3.1	$^{232}\text{Th}$ and $^{238}\text{U}$ decay chains . . . . .	29
3.2	Graphic breaking down outcomes of $^{210}\text{Po}$ surface alphas with different decay points . . . . .	32
3.3	Graphic of $\alpha$ -decay occurring within a dust particulate in the liquid argon bulk . . . . .	34
4.1	Z Position reconstruction consistency in surface alpha control region .	38

4.2	Three year dataset after surface alpha preselection, before clipping and saturation corrections . . . . .	39
4.3	Three year dataset after surface alpha preselection, with clipping and saturation corrections . . . . .	40
4.4	Results of $^{210}\text{Po}$ surface alpha fit . . . . .	43
4.5	Validation of surface alpha trigger rate estimate . . . . .	49
4.6	Reconstructed radius of $^{210}\text{Po}$ surface alpha simulations . . . . .	50
4.7	PMT map in $\cos \theta$ and $\phi$ , with gaps in PMT coverage labelled. . . . .	51
4.8	True angular distribution of surface alphas . . . . .	53
4.9	True angular distribution of surface alphas that reconstruct beneath 800 mm . . . . .	53
4.10	True angular distribution of surface alphas that reconstruct beneath 720 mm, with reconstructed position connected . . . . .	54
4.11	True angular distribution of surface alphas that reconstruct beneath 800, using version of RAT with some disabled PMTs . . . . .	55
4.12	True angular distribution of surface alphas that reconstruct beneath 720 mm, with reconstructed position connected, using version of RAT with some disabled PMTs . . . . .	56
4.13	TPB/LAr interface alpha leakage as a function of contained LAr mass	60
5.1	Illustration of the flowguide components in the AV neck . . . . .	63
5.2	Features in neck Monte Carlo samples . . . . .	65
5.3	Three dimensional neck control regions . . . . .	66
5.4	Two dimensional projection of neck control regions . . . . .	66
5.5	Stacked histogram of neck preselection comparing dust and neck alpha simulations to data . . . . .	68
5.6	Results of the neck alpha template fit, with mapped control regions .	69
5.7	Results of the neck alpha template fit, with stacked control regions .	70

5.8	Fprompt distributions of 25 $\mu\text{m}$ LAr layer and nominal samples . . .	72
5.9	PE distributions of neck alpha systematic variation samples . . . . .	74
5.10	Fprompt distributions of neck alpha systematic variation samples . .	75
6.1	Difference in position reconstruction algorithms for Z position, used to mitigate neck alpha events . . . . .	79
6.2	Impact of Z Position Consistency Cut on simulated background and signal samples . . . . .	81
6.3	Impact of 3D Position Consistency Cut on simulated background and signal samples . . . . .	81
6.4	Impact of upper Fprompt contour of ROI on simulated background and signal samples . . . . .	82
6.5	Random Forest estimator distribution for simulated background and signal samples . . . . .	84
6.6	Boosted Decision Tree estimator distribution for simulated background and signal samples . . . . .	85
6.7	Neural Network estimator distribution for simulated background and signal samples . . . . .	85
6.8	Event selection optimization grid scan results for RF and NN estimator combination . . . . .	90
6.9	Fprompt distribution of simulated surface alphas vs data in surface alpha validation region . . . . .	98
6.10	nHit/PE distribution of simulated $^{210}\text{Po}$ TPB/LAr interface samples .	99
6.11	nHit/PE distribution of 376 live days of data after low-level preselec- tion in dark matter search ROI . . . . .	100
6.12	Reconstructed radius of the 1,305 candidate events within nHit/PE contours and 30% ROI . . . . .	101

6.13 Preliminary exclusion curves using the optimized event selection and full livetime . . . . .	104
A.1 Nuclear quenching factor in liquid argon for a range of alpha starting energies . . . . .	120
A.2 PE distribution of bulk alphas using best fit to Mei et al. quenching model . . . . .	124
A.3 Hitachi luminescent quenching model fit to high energy alpha data . .	126
A.4 PE distribution of bulk alphas using best fit to Hitachi quenching model	126
B.1 Event selection optimization grid scan results for RF estimator . . . .	128
B.2 Event selection optimization grid scan results for XGB estimator . . .	129
B.3 Event selection optimization grid scan results for NN estimator . . . .	130
C.1 PE distributions of dust alpha systematic variation samples . . . . .	132
C.2 Fprompt distributions of dust alpha systematic variation samples . .	133
C.3 Reconstructed radius distributions of dust alpha systematic variation samples . . . . .	134

# Glossary

<b>AV</b>	<b>A</b> crylic <b>V</b> essel
<b>CL</b>	<b>C</b> onfidence <b>L</b> evel
<b>CMB</b>	<b>C</b> osmic <b>M</b> icrowave <b>B</b> ackground
<b>DAQ</b>	<b>D</b> ata <b>A</b> cquisition
<b>DEAP</b>	<b>D</b> ark Matter <b>E</b> xperiment using <b>A</b> rgon <b>P</b> ulse-shape discrimination
<b>ER</b>	<b>E</b> lectronic <b>R</b> ecoil
<b>GA</b> r	<b>G</b> aseous <b>A</b> rgon
<b>LA</b> r	<b>L</b> iquid <b>A</b> rgon
<b>MC</b>	<b>M</b> onte <b>C</b> arlo
<b>NR</b>	<b>N</b> uclear <b>R</b> ecoil
<b>PMT</b>	<b>P</b> hoto <b>M</b> ultiplier <b>T</b> ube
<b>PSD</b>	<b>P</b> ulse <b>S</b> hape <b>D</b> iscrimination
<b>PE</b>	<b>P</b> hoto <b>E</b> lectron
<b>RAT</b>	<b>R</b> eactor <b>A</b> nalysis <b>T</b> ool
<b>ROI</b>	<b>R</b> egion <b>O</b> f <b>I</b> nterest
<b>TPB</b>	<b>T</b> etraphenyl <b>B</b> utadiene
<b>WIMP</b>	<b>W</b> eakly <b>I</b> nteracting <b>M</b> assive <b>P</b> article

# Chapter 1

## Introduction

### 1.1 Evidence for Dark Matter

The existence of additional, non-luminous matter outside the Standard Model of particle physics has been postulated as an explanation for excess mass observed at galactic and cosmological scales. In particular, measurements done by the Planck collaboration indicate that only 4.8% of the Universe's energy density is composed of ordinary matter. Consequentially roughly 85% of mass in the Universe is composed of non-visible matter [1]. This matter is referred to as dark matter (DM), and its true nature is one of the biggest questions in modern physics. The need for dark matter is based on a large collection of evidence over the last 100 years. These effects all show a deficit in mass in galactic and cosmological scales that can not be explained by modified theories of gravity [2].

In 1933, astronomer Fritz Zwicky collected some of the first evidence in support of dark matter. Zwicky applied the Virial theorem and conservation of energy to structures in the Coma Cluster to find their properties. It was found that galaxies in the cluster rotate too fast to be held by their own gravity, and an invisible mass is required for the calculated velocities to be possible. This excess of density in

the galaxy is roughly 400 times more than what can be explained by visible matter [3, 4, 5].

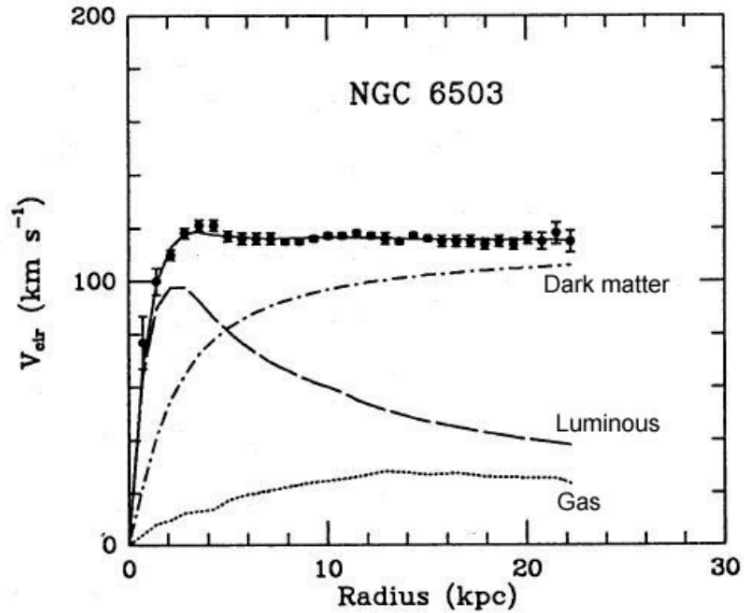


Figure 1.1: Tangential velocity versus radius from the centre of NGC 6503 galaxy. Data points are for the different structures in NGC 6503 galaxy. Contributions from luminous (ordinary) matter, gas, and dark matter are separated and displayed. [6]

In the 1970s and 1980s, Vera Rubin and Kent Ford found further evidence to support Zwicky's dark matter hypothesis. Using the Virial theorem again, Rubin measured the rotational velocities of many different spiral galaxies. It was found that these galaxies did not behave as expected from the theorem [7]. The rotational velocity of structures at the far radius of the spiral galaxy were measured with a larger velocity than can be explained with luminous matter (displayed for galaxy NGC 6503 in Figure 1.1). This measurement was repeated for many different galaxies, with the same conclusion each time [6]. Instead, a significant amount of added dark matter is necessary to compensate, and allow the outer regions to rotate at a similar velocity to central regions. This postulated amount is labelled as "dark matter" in the figure.

Gravitational lensing is another effect that displays the impacts of dark matter

at a galactic scale. Gravitational lensing is an effect in which a gravitational field from a large mass can bend the trajectory of light. The equation for the angle of this refraction,  $\theta_{GL}$ , is defined as [8]:

$$\theta_{GL} = \frac{4GM}{rc^2} \quad (1.1)$$

where  $G$  is the gravitational constant,  $M$  is the mass of the object causing the field,  $r$  is the minimal distance between the mass and light ray, and  $c$  is the speed of light. This equation gives a direct relationship between the mass of a large scale galactic structure, and an observable effect, the bend of the light.

The creation of the Bullet cluster, from the merging of two separate galaxy clusters, provided a tremendous opportunity for the measurement of DM via gravitational lensing. Clowe, et al. [9] measured the lensing from this cluster, displayed in Figure 1.2. The heat map gives an indication of where the baryonic (ordinary) matter is in the galaxy cluster merger. The matter is concentrated around the center of the two galaxies. The gravitational lensing effects, indicated by the green contours, shows that the actual galaxy centers are farther away from the center of the merger. This difference can be explained by a large mass of weakly interacting invisible matter [9].

Currently, the cosmic microwave background (CMB) radiation is used to measure the mass density of the Universe. CMB radiation is the distribution of the light in the early Universe just after matter recombination. The expansion of the Universe over time redshifts the radiation to the microwave frequency range. The temperature is nearly isotropic, but small temperature fluctuations within the radiation contain a large amount of information about the densities, structures, and types of particles present in the early Universe. By transforming these fluctuations into spherical harmonics, the data can be fit to the  $\Lambda$ CDM cosmological model. The mass density of the Universe is parameterized into four different density components: dark energy

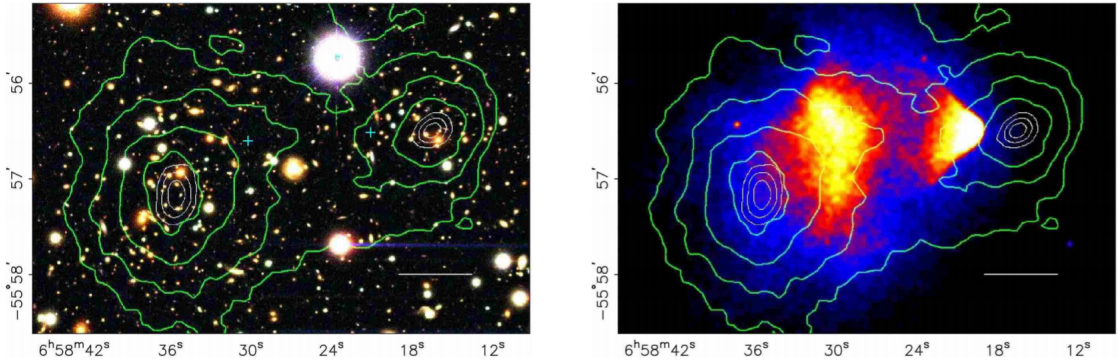


Figure 1.2: Two depictions of the Bullet cluster. The green contours indicate where the mass centers should be based on measured gravitational lensing. On the left is an image taken by the Magellan IMACS Telescope, and on the right an x-ray image from the Chandra X-ray Observatory. The heat map on the right shows where the mass should be based on x-ray emission. This heat map shows the location of baryonic matter in the cluster merger. [9]

( $\Omega_\Lambda$ ), dark matter ( $\Omega_c$ ), baryonic matter ( $\Omega_b$ ), and radiation ( $\Omega_{rad}$ ). The CMB fluctuations are used by the Planck Collaboration to constrain these parameters, and get an estimate of the make up of the Universe.

From the 2018 Planck Cosmological parameter calculations [1] a dark matter density of  $\Omega_c h^2 = 0.12011$  is found, compared to an ordinary matter density of  $\Omega_b h^2 = 0.022383$ . In these parameters,  $h$  is the dimensionless Hubble parameter, dependent on the Hubble Constant  $H_0$ .

## 1.2 WIMPs: A Dark Matter Candidate

The existence of non-luminous matter in the Universe is well accepted. Instead, the nature of this matter is the current mystery of the cosmological model. There are many theories, both at a particle level and a galactic level. Originally, astronomers theorized large structures that emit little to no radiation, now labelled as MACHOs (**MA**ssive **C**ompact **H**alo **O**bjects). These objects are baryonic in nature, and can include black holes or neutron stars. It is more likely that dark matter is non-baryonic.

Theoretical work shows that the early Universe could not produce enough baryonic

matter to still be consistent with the amount of mass required by dark matter, and a large fraction of non-baryonic matter is required in the Universe [10]. For particle physics dark matter candidates, choices are limited to massive, weakly interacting, non-baryonic particles.

This omits the majority of the Standard Model. The only potential dark matter candidate among the current fundamental particles is the neutrino, which is massive, and weakly interacting. However, the extremely small mass scale of the neutrino requires it to be hot dark matter (HDM). Dark matter candidates can be classified as hot, cold, or warm depending on how relativistic they were in the early Universe. Hot dark matter, which has a mass in the range of tens of eV, is too relativistic to be compatible with the current formation of galaxies and clusters, and can therefore only be a small fraction of the total dark matter density. Instead, cold dark matter candidates are preferred, as their large mass scale ( $\text{GeV}/c^2$ - $\text{TeV}/c^2$ ) is in agreement with current galactic structures [2].

The prevailing theory is that dark matter comprises new, fundamental, beyond the Standard Model particles. A plot of different particle dark matter candidates in mass and cross-section space can be seen in Figure 1.3 [11]. These candidates include WIMPs (purple), axions (green), SuperWIMPs (red), and other more exotic candidates. Figure 1.3 has the neutrino listed as well for reference. WIMPs are **Weakly-Interacting Massive Particles**. They are non-baryonic, heavy particles interacting exclusively through gravity and the weak force.

It is theorized that these heavy particles were produced thermally in the early Universe. Self-annihilation interactions allowed for conversion between WIMPs and ordinary matter. This only occurred at the extremely high energies of the early Universe [12]. In these high temperatures, dark matter and Standard Model particles were in thermal equilibrium. As the Universe cooled, WIMPs reached a thermal freeze-out, where they fell out of equilibrium with SM particles. The density of

WIMPs now remains essentially constant, and is abundant in the Universe.

SuperWIMPs are a lighter form of WIMP with an interaction cross-section closer to the gravitational scale. These candidates are considered warm dark matter, being lower in mass than cold dark matter and more relativistic. The cross-section of the particles are so low that thermal equilibrium could not have been reached in the early Universe. Instead it is theorized that these particles were produced through decays of heavier nuclei, including potential WIMP decays [2]. An alternative dark matter candidate to the WIMP is the axion. Axions are extremely light (less than an eV), and are the result of a potential solution to the strong CP (charge-parity) problem. The axion would be very small, yet slow-moving, making it cold dark matter [2]. While all of these are potential candidates, the focus of the DEAP-3600 experiment, and in turn this thesis, will be on WIMPs. In this way, any reference to "dark matter" from this point on is specifically referencing WIMPs.

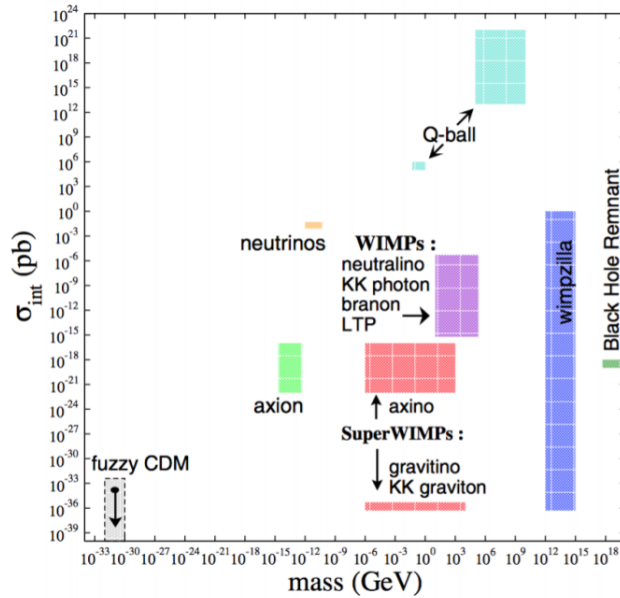


Figure 1.3: Dark matter particle candidates in parameter space (cross-section on y-axis, mass on x-axis) [11]. Note 1 picobarn (pb) =  $10^{-36}$  cm<sup>2</sup>.

## 1.3 Dark Matter Detection

The detection of WIMPs, and other candidate particles, is difficult given that the defining characteristic of dark matter is its low cross-section. There are currently three major ways to detect dark matter: direct, indirect and pair production.

In the case of pair-production, extremely high energy baryonic matter can be collided in hopes of reproducing the annihilation interaction theorized to exist in the early Universe. In this way dark matter can be produced, and the missing transverse energy in the detector can be measured. This is difficult given the high luminosity necessary to reach the low dark matter self-annihilation cross-section. Pair production is currently being explored at the CMS and ATLAS Collaborations at the Large Hadron Collider [13].

For indirect detection the goal is to observe signs of dark matter self-annihilation or decay. WIMPs that pass through the Sun or a large stellar body would be slowed enough to be captured, eventually decaying or annihilating. These interactions would result in a higher flux of Standard Model particles. Experiments designed to optimize neutrino sensitivity would be able to measure this change in flux, and can monitor this for a potential indication of dark matter. Neutrino experiments like SuperKamiokande [14] and IceCube [15] are examples of this method.

Finally, direct detection revolves around using a target material to elastically scatter with dark matter. The WIMP nucleus deposits energy into the target material, creating a nuclear recoil (NR). The evidence of those interactions can come in the form of heat, charge or scintillation light. This evidence is used to distinguish between a potential WIMP scatter and background events [10].

There are different experiments tackling each of these methods in different ways. In this way, the WIMP parameter space is being fully explored. As these experiments continue to search for WIMPs, upper limits to the WIMP-nucleon cross-section can be attained. Figure 1.4 shows the exclusion curves (the lower limit of the explored

parameter space) for some major WIMP detection experiments [2]. The full extent of this parameter space is limited by the neutrino floor, shaded in yellow in Figure 1.4. In this space, coherent neutrino-nucleus scattering events become an irreducible background, as they can not be distinguished from WIMP-nuclei interactions. This background drastically reduces WIMP sensitivity, and represents the limit of the WIMP direct detection parameter space.

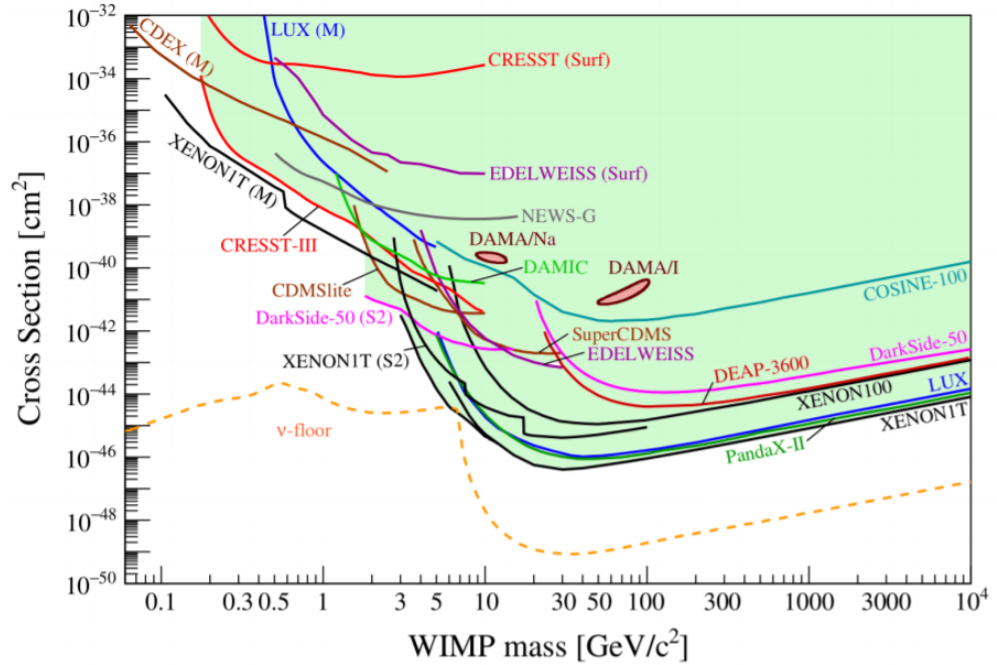


Figure 1.4: Spin-independent elastic WIMP-nucleus scattering exclusion curves for various WIMP detection experiments. Parameter space where coherent neutrino scattering background becomes problematic is found beneath the orange dotted line. [2]

A figure from the most recent dark matter search results from DEAP-3600 [16] shows some leading exclusion curves from direct detection experiments (Figure 1.5). The exclusion curves in this figure come from noble liquid detectors, to directly compare with DEAP-3600. These experiments use low background noble liquid detectors in large mass and measure scintillation light from the material. This is often done with either argon or xenon as the target mass.

XENON1T [17], PANDAX-II [18], LUX [19], and DarkSide-50 [20] are all dual-

phase time projection chambers. These experiments employ xenon (and argon in the case of DarkSide-50) in both the liquid and gas phases within the chamber. An electric field is applied to the scintillation material, allowing for electron acceleration and consequentially noble gas excitation. This causes an event to create a secondary scintillation signal along with the scintillation signal in the noble liquid. These signals are combined with the measured charge of the event, allowing for three dimensional track reconstruction. DEAP-3600 varies from these experiments in multiple ways. DEAP-3600 employs single-phase liquid argon, and applies no electric field to the chamber. Only scintillation signals are measured, and only from liquid scintillation responses. This scintillation process, and how the DEAP-3600 detector is designed to measure it, is explained in the next chapter.

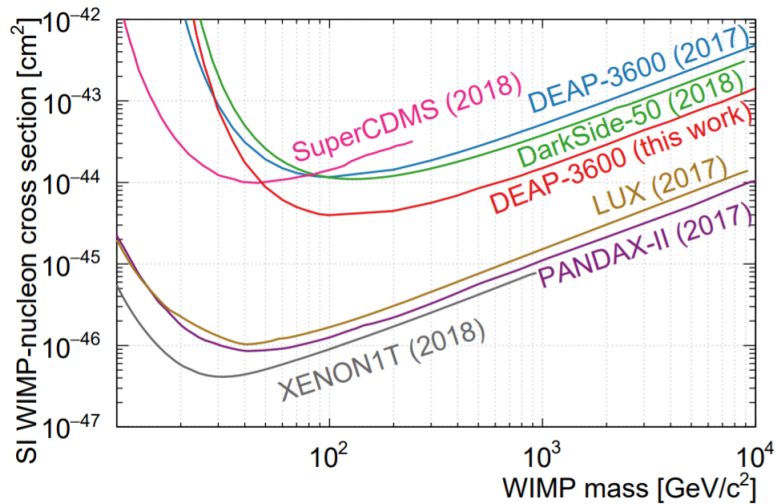


Figure 1.5: Exclusion curves for some leading WIMP direct detection experiments. This figure comes from the 231 live day DEAP-3600 publication from 2019. Included are a number of noble liquid detectors. [16]

## 1.4 Outline

DEAP-3600 is a liquid argon based noble liquid detector. Such an experiment requires an extremely low background in order to achieve the high sensitivities necessary

to probe low cross-sections. A large portion of backgrounds are mitigated through the design of the detector. Backgrounds are further mitigated using an analysis of the different excited argon states, and their different lifetimes. It is impossible to remove all backgrounds in the WIMP search with these effects alone, and added analysis is needed for the remaining sources in the background model. The focus of this thesis will be on one type of these remaining background components in the DEAP-3600 WIMP search, alpha backgrounds. An attenuated alpha particle passing through the scintillation material has the potential to mimic a WIMP-nucleus interaction, and these alphas become the major background in the WIMP search after electronic recoil (ER) discrimination. Quantifying and limiting these alpha backgrounds will be explored in detail.

Chapter 2 will provide an overview of the DEAP-3600 experiment, including the important components of its construction and design, and an explanation of the excited argon livetime analysis that leads to pulshape discrimination (PSD). Chapter 3 will explore the current DEAP-3600 background model, with an extended focus on the role of attenuated alphas in the model. Chapters 4 and 5 will quantify two of these sources of alpha background, determining an event rate and in some cases an activity. Chapter 6 will use these rates, along with the remainder of the background model, to create an event selection to reject background events and select candidate WIMP-nucleus interactions, maximizing WIMP sensitivity.

# Chapter 2

## DEAP-3600 Detector

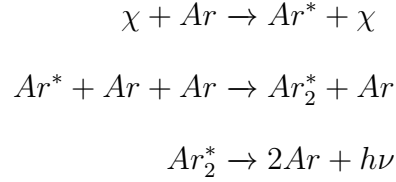
The DEAP-3600 experiment in Sudbury, ON uses liquid argon (LAr) to directly detect WIMP signals using scintillation light. This chapter will explain the physics behind this scintillation process, and how it allows for the measurement of a WIMP signal. This process educates the choices made in the detector design. A description of the DEAP-3600 experiment and detector, highlighting the components relevant to alpha background discrimination, is given. Finally an argument for liquid argon as a scintillation material is made, focusing on the strong pulshape discrimination LAr provides. This process is crucial to limiting electronic recoil backgrounds.

### 2.1 Scintillation in Noble Liquids

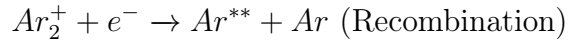
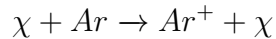
A brief overview of direct dark matter experiments is given in Chapter 1. While many different signal types can be used, noble liquid detectors rely on scintillation light to measure WIMP (or background) events. These detectors make for great dark matter detection, given their inert nature and commercial availability [21]. Currently, liquid xenon and liquid argon are the most common choices for dark matter experiments. In the case of the DEAP-3600 detector, a  $3279 \text{ kg} \pm 96 \text{ kg}$  mass of liquid argon is used as the target material [16].

WIMP particles (denoted by  $\chi$ ) pass through the scintillation material and scatter with argon nuclei, depositing energy. Argon atoms in the volume become excited and ionized during this process. In both cases, scintillation light is created from the energized atom.

In the case of an excited argon atom ( $Ar^*$ ), this can bind with a ground-state argon atom to create an excited argon dimer, also called an excimer ( $Ar_2^*$ ). The excimer releases a scintillation photon ( $h\nu$ ) to return to the ground state, where the dimer is dissociated. [22].



For an ionized argon atom ( $Ar^+$ ), the process is very similar. The ionized atom bonds with a ground state atom and forms a ionized dimer ( $Ar_2^+$ ). At this point the dimer can transition to an excimer through recombination. The dimer recombines with free ionized electrons and creates a highly excited argon atom ( $Ar^{**}$ ), returning the other argon atom to the ground state. Energy is released from the highly excited atom in the form of heat, reaching the lowest excited state. At this point, the process for the excited atom above is repeated again resulting in the emission of a scintillation photon. This photon is released at 128 nm, in the ultraviolet range [23]. The process of an ionized argon atom producing scintillation light is broken down below [22].



Noble liquids provide a great light yield [24], the ratio of scintillation photons to incoming particle energy. Monitoring the number of photons generated in an event allows for the measurement of the energy of the incoming particle. The design of the DEAP-3600 experiment is based around this principle, looking to efficiently measure these photons, and discriminate against scintillation light that comes from non-WIMP interactions. By installing photo multiplier tubes (PMTs) around the argon mass, the scintillation photons can be collected and converted to photoelectrons (PE). PE counts are stored and used to analyze different events.

## 2.2 DEAP-3600 Detector

The DEAP-3600 detector is a single-phase liquid argon detector located in the SNOLAB facility in Sudbury, ON. The aim of the detector is to search for spin independent WIMP dark matter signals. The design sensitivity to the WIMP-nucleon cross-section is  $10^{-46} \text{ cm}^2$  for a  $100 \text{ GeV}/c^2$  WIMP [21]. The experiment is run by the DEAP Collaboration, a team of over 90 researchers across 16 institutions.

### 2.2.1 SNOLAB Facility

The SNOLAB underground research facility was created for the Sudbury Neutrino Observatory (SNO) experiment [25]. An important aspect of astroparticle physics experiments is the limiting of cosmic ray muons, an otherwise large background source. As such, the facility is located in the Creighton Mine, roughly 2 km below ground. This level of rock overburden heavily limits cosmic radiation from above the surface. While this is beneficial to a neutrino experiment, this is also very beneficial to a direct dark matter experiment, where diminished background levels are a necessity. The cosmic ray muon flux in SNOLAB was measured to be  $0.27 \text{ muons/m}^2/\text{d}$  [25]. The DEAP detector is located in the Cube Hall of the facility. A layout of the facility can be seen in Figure 2.1, where the Cube Hall can be found in the top left corner.

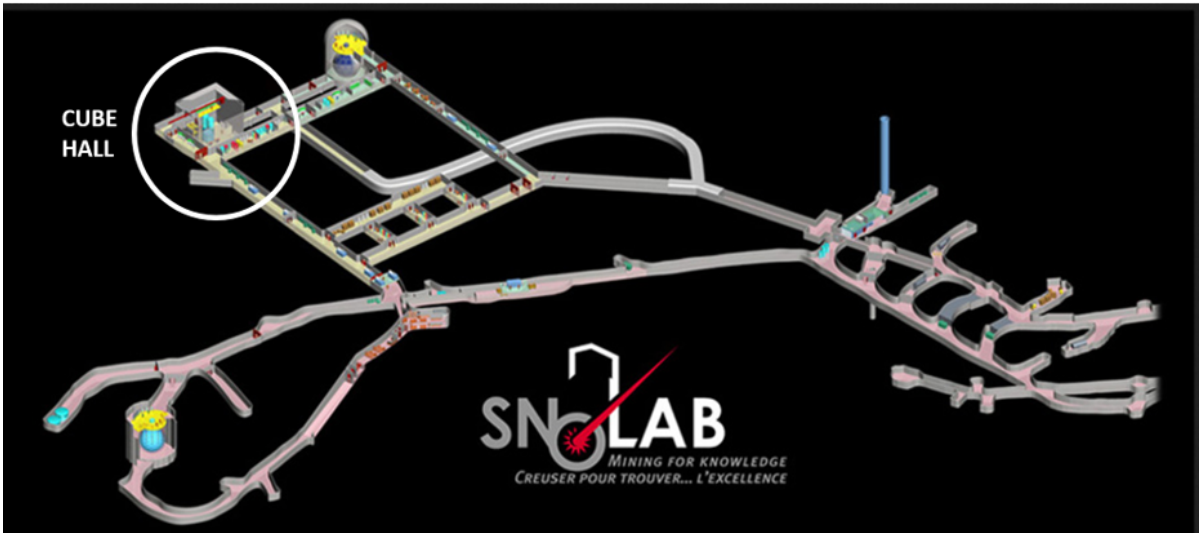


Figure 2.1: Map of the SNOLAB facilities. The Cube Hall, where the DEAP-3600 experiment resides, is indicated at the top left corner. [25]

### 2.2.2 Detector Design

A schematic cross-section of the detector is displayed in Figure 2.2. The primary components of the detector are labelled on this figure. These components will each be described individually in the section, starting from the inside of the detector and

working towards the outside. The data acquisition system (DAQ) will also be explained, alongside the different event reconstruction algorithms and the DEAP-3600 simulation software.

The liquid argon is held in a 851 mm radius spherical acrylic vessel. The vessel is 5 cm thick. This sphere is often referred to as the AV. Acrylic is the choice of material as its optical and thermal properties are ideal for this type of experiment. The large temperature gradient allows for the storage of 87 K liquid argon, while leaving the outer components at operating temperatures. This is crucial as the exterior components of the detector (such as the PMTs) have the optimal efficiency at room temperature. The level of radiopurity in acrylic can also be well controlled, and the acrylic components were manufactured to be as pure as possible [26].

This vessel is surrounded by 255 8-inch R5912 Hamamatsu high quantum efficiency PMTs (maximum QF of 32% at 420 nm) [27]. The acrylic is transparent to visible light but opaque to ultraviolet. The PMT quantum efficiency spectrum peaks in the violet region of light, sharply declining in the ultraviolet portion of the spectrum [28]. The inside surface of the acrylic vessel is coated in an organic wavelength shifter, 1,1,4,4-tetraphenyl-1,3-butadiene (TPB), that redshifts the LAr scintillation light to 420 nm [29]. This TPB layer was evaporated under vacuum onto the surface, with a target thickness of 3  $\mu\text{m}$  [30]. In this way, visible light is passed through the acrylic.

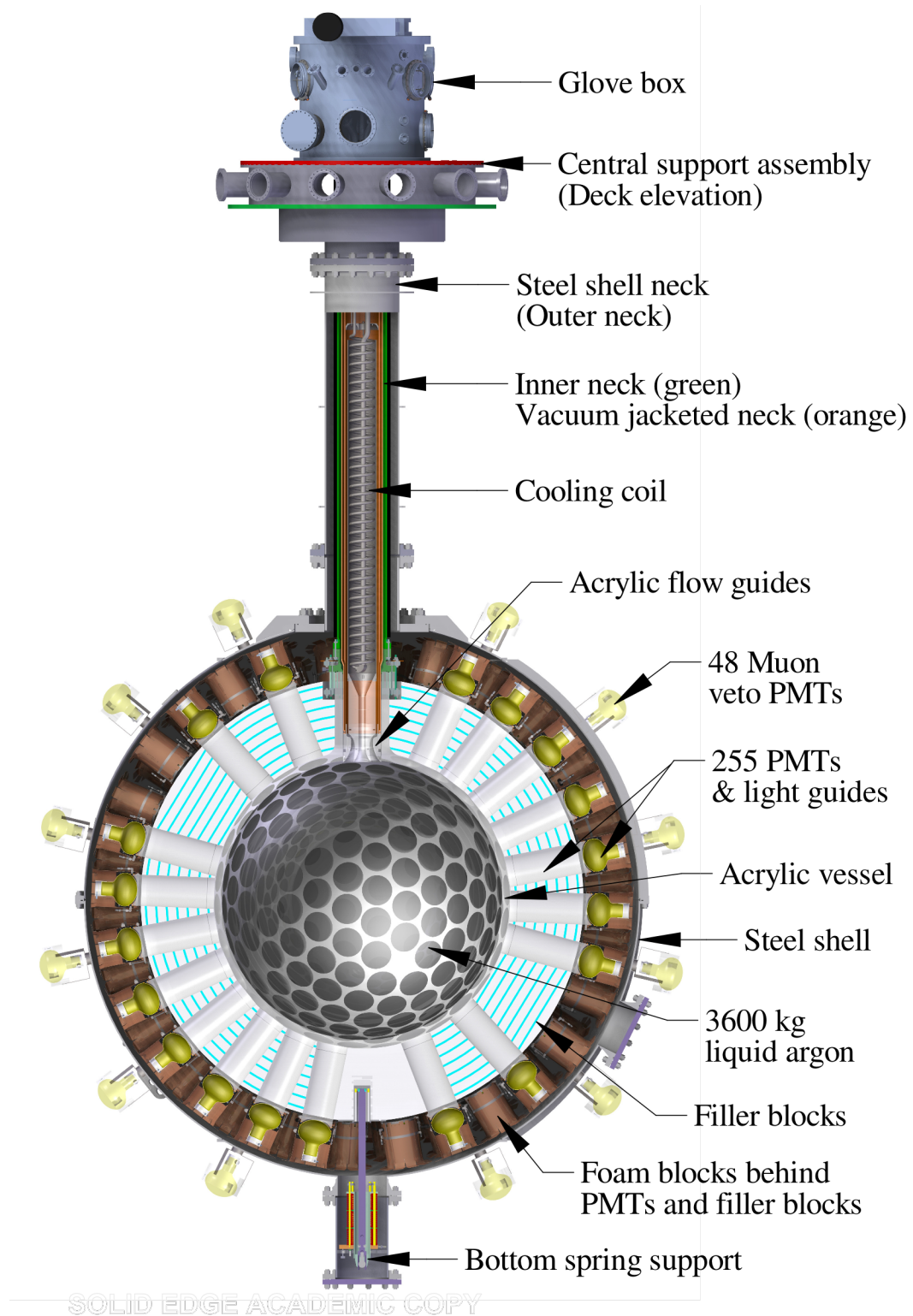


Figure 2.2: Cross-section of the DEAP-3600 detector design. All major components are labelled. Missing from the labels is the TPB layer on the inside of the acrylic vessel, and the water tank the detector is submerged in. [21]

The PMTs are attached to the AV using 45 cm long acrylic light guides bonded to the outer surface of the vessel. These light guides are designed not only for light transmission, but also for thermal insulation of the PMTs. These acrylic structures also provide neutron shielding from the borosilicate PMT glass, a primary source of the neutron background [21]. The light guides cover 76% of the acrylic vessel surface area, each evenly distributing light across the corresponding PMT glass surface.

Between the light guides are filler blocks made of polyethylene and polystyrene [21]. These blocks act as part of the neutron shielding, as well as thermal insulation. This entire set up is encased in a closed steel shell, and submerged in an ultra-pure water tank. While the cosmic muon flux is very low in SNOLAB, it is still non-zero, and must be eliminated in the analysis. To accomplish this, the steel shell is covered in 48 outward facing Hamamatsu R1408 PMTs. These PMTs act as a muon veto, eliminating events that coincide with Cherenkov light in the water tank.

The inner vessel can be accessed through the neck, a vertical tube at the top of the detector with an inner diameter of 255 mm [21]. There are two flowguides, termed inner and outer, with the purpose of guiding the flow of LAr down into the acrylic vessel, and the flow of gaseous argon (GAr) back up into the cooling coils. These cooling coils use liquid nitrogen to cool the LAr. The neck itself is encased in steel, much like the full vessel. The neck assembly also connects the detector to the upper deck [21].

All of these design choices are based around reducing the backgrounds in the WIMP search to zero. Materials are chosen to maximize neutron shielding. Treatment of the materials was done to minimize exposure to any radon contamination that would reduce the radiopurity. The inner vessel was resurfaced in-situ, to eliminate large portions of the radon deposition [31]. These  $^{220}\text{Rn}$  and  $^{222}\text{Rn}$  deposits (and their daughter nuclei) alpha decay. These alphas can mimic WIMP signals depending on their starting location and the amount of energy deposited. These backgrounds,

along with other prevalent backgrounds including neutrons and electromagnetic backgrounds, are described in Chapter 3.

The signals of the PMTs are recorded by the data acquisition system [32]. This system has multiple hardware components. A flowchart is provided in Figure 2.3 showing the path of data through each component. The PMTs generate an analog signal by converting incident photons to a photoelectron count, using the photoelectric effect. These PMTs are connected to signal conditioning boards (SCB), that shapes the analog pulse and prepares it for the digitizers. There are 27 of these SCBs. The charge is measured from these boards using the CAEN V1720 digitizers. These components create a digitized trace of the PMT signal, with a 12-bit precision, corresponding to 4096 ADC (analog to digital) units. A second smaller set of CAEN V1740 digitizers measuring a low gain output are also used. In the case that a large amount of information is sent to a PMT, such that the V1720 digitizer goes past the 12-bit precision, some information is stored in this V1740 digitizer.

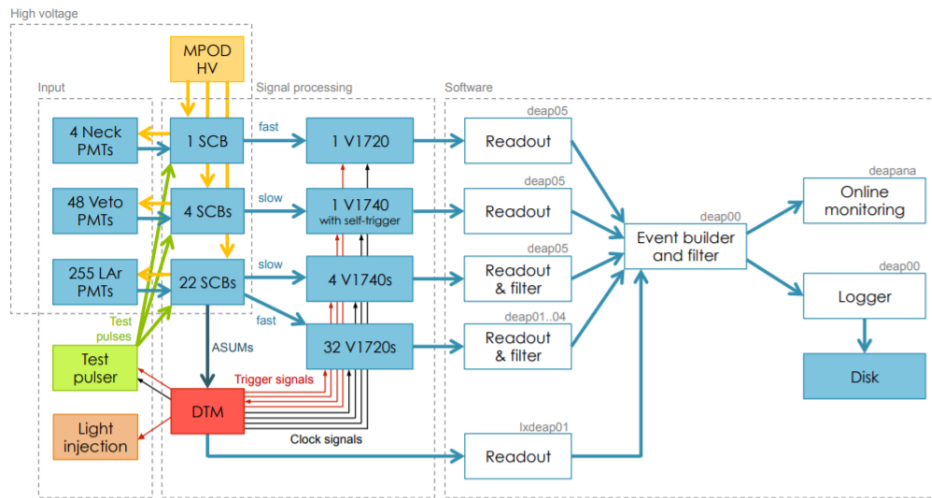


Figure 2.3: Flow chart of the DEAP-3600 data acquisition system. The PMTs run directly to the signal conditioning boards, where the outputs are digitized by the V1720 and V1740 digitizers. Triggers are identified by the DTM, and saved signals are put through the event builder software for saving to disk. [32]

These digitizers save a waveform of  $16 \mu\text{s}$ , but only if a trigger is signaled. The

DTM, or digitizer and trigger module, chooses if an event registers a trigger using the summed signal from the SCB boards and the trigger conditions. At this point, the digitizers and triggering information are transferred to an event object using the Event Builder software and saved to disk.

RAT and DEAP-3600 utilize multiple event reconstruction algorithms to determine different characteristics of an event. The total charge of the event particle is determined by measuring PE counts over a  $10 \mu\text{s}$  window after the trigger occurs, taking the integral of PE over the window as the total event PE. There are two PE estimators used, one based around summing the PE count from all PMTs ("qPE"), and another using Bayesian analysis to calculate the most probable amount of PE generated in the LAr ("nSCBayes"). The latter is the preferred algorithm in this analysis as this estimator removes PMT after-pulsing effects. Any reference to the PE of an event refers to the result of this algorithm unless stated otherwise.

The position of the event is determined using position reconstruction algorithms. There are two main algorithms used. The first, "MBLikelihood", uses the spatial distribution of the charge in the PMTs to determine event position. The second, "TimeFit2", combines this charge distribution with the photon arrival time for a time-based position reconstruction. These algorithms produce positional variables both in the Cartesian coordinates ( $X, Y, Z$ ) and the spherical coordinates ( $R, \theta, \phi$ ) of the detector, where the origin of both frames is at the center of the liquid argon mass. The analysis in this paper uses the variables from the "MBLikelihood" algorithm, and any references to reconstructed position variables in this paper is using this algorithm.

The DEAP detector has been taking data under the current run conditions for 5 years, producing a large amount of tracked events. This work will make reference to multiple datasets, with different livetimes measured in livedays. The full livetime dataset used at the time of this thesis makes up 802 live days of running detector, running from November 2016 - December 2020. References are made to the most

recent DEAP-3600 published results, done using 231 live days [16], running from November 2016 - October 2017.

While 802 livedays are currently available, a large portion of the data is blinded. Instead an open dataset of 376 live days is used for analysis, and to make predictions across the full 802 day livetime. These livetimes also account for an event dead time of  $20 \mu\text{s}$  per event, using the calculation  $livetime_{corrected} = livetime_{database} - n_{events} \cdot 0.00002$ . A muon veto correction is then also applied for any events that trigger the muon veto. The total corrected livetime in seconds used for this analysis is then  $32,452,620 \text{ secs} = 375.621 \text{ days}$ .

Accompanying the event builder and analysis software is a DEAP-3600 detector simulation. This simulation uses a customized version of RAT, a software using Geant4 and ROOT to simulate and analyze liquid scintillator experiments [33]. The simulation software includes the built detector geometry, using optical parameters and geometrical parameters defined through external measurements and studies. The scintillation photons, and the full optical process, are simulated within RAT, and signals are measured in the simulated PMTs to replicate the real life detector process. In this way, the event generation process is recreated within the RAT framework, allowing simulated particles to generate realistic PMT signals. These PMT signals are passed through the same framework as the actual data path, using the same Event Builder software to construct and save the events, allowing the same reconstruction algorithms to be applied to both simulations and data.

These simulations are used for a large amount of analysis efforts, including the background studies detailed in this thesis. If any reference to simulated event samples is made in this paper, they were generated using Monte Carlo simulations with the RAT framework.

## 2.3 Pulseshape Discrimination

For DEAP-3600, argon was chosen as the noble liquid scintillator for a multitude of reasons. The light yield in liquid argon is on par with other noble liquids [24], with a light yield of  $6.1 \pm 0.4$  PE/keV<sub>ee</sub> in the DEAP-3600 detector after accounting for PMT after-pulsing [16]. Argon also is much easier to acquire than xenon, costing a lot less to extract from the atmosphere [21]. Most importantly however, is the high level of pulseshape discrimination that can be achieved with liquid argon. This aspect of the experiment is crucial to the WIMP search. DEAP itself stands for **D**ark **M**atter **E**xperiment using **A**rgon **P**ulseshape **D**iscrimination.

The excited dimers described earlier in the chapter have two different possible spin states: the singlet state and the triplet state. The singlet state has a much shorter lifetime of 8 ns, while the triplet lifetime is in the range of 1.5  $\mu$ s [34]. In the case of xenon, this separation is smaller, on the order of a few nanoseconds. Separation is critical, as the type of particle scattering off the argon atom can influence the ratio of singlet and triplet states.

Electronic recoil (ER) events are events that lose energy to the electrons in the LAr. These reactions favor generating triplet states. Meanwhile, nuclear recoil (NR) events, events losing energy to the argon nuclei, favor singlet states. In this way, the scintillation light from ER events, like  $\beta$ -decays, produce more argon excimers with a long livetime. They de-excite and release scintillation light over a longer range of time. Light from NR events, like WIMP-nuclei scatters, produce more excimers with a short livetime, releasing scintillation light in a short, early window. The parameter  $F_{\text{prompt}}$  can be defined to take advantage of this discrepancy.  $F_{\text{prompt}}$ , defined in Equation 2.1, is the ratio of light appearing in the early or "prompt" window of an event, compared to the total light in the event. The prompt window is defined as the

first 60 ns of the event.

$$F_{\text{prompt}} = \frac{\sum_{t=-28ns}^{60ns} \text{PE}(t)}{\sum_{t=-28ns}^{10\mu s} \text{PE}(t)} \quad (2.1)$$

Since nuclear recoils create mostly singlet state excimers, the  $F_{\text{prompt}}$  value for nuclear recoils are close to 0.7. The opposite logic follows for electronic recoils, resulting in a  $F_{\text{prompt}}$  value closer to 0.3. The distribution of  $F_{\text{prompt}}$  between these two event types are displayed in Figure 2.4. Here the separation between the populations is clear. This allows for the rejection of electronic recoil events, which are exclusively background events to the WIMP search.

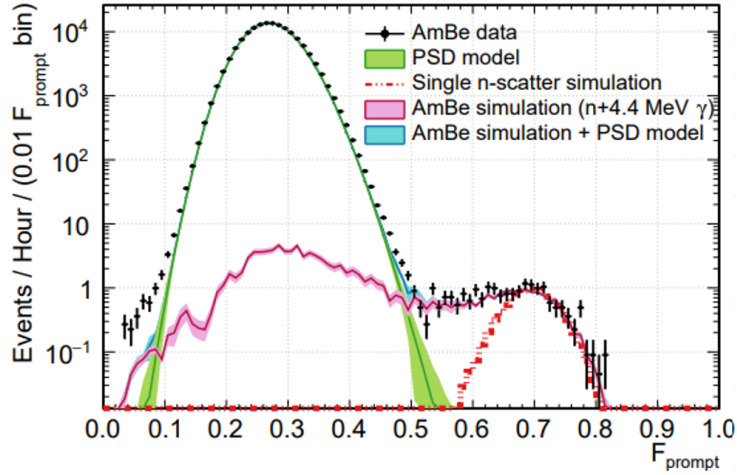


Figure 2.4:  $F_{\text{prompt}}$  distribution of events in the WIMP PE range (120-200 PE) using AmBe source data. Data (black) agrees with the sum (blue) of the ER background model (green) and simulated AmBe source (pink). Electronic recoil background data follows a distribution around a small prompt value of 0.3. Nuclear recoil data is distributed about an  $F_{\text{prompt}}$  of 0.7. [16]

With this we can define a region in  $F_{\text{prompt}}:\text{PE}$  space where WIMP sensitivity is maximized. This region would minimize any background events, while trying to maintain the highest possible signal acceptance. This region is defined as the Region

of Interest (ROI) and becomes the dark matter search area. The ROI shape is shown in Figure 2.5. The location of the region is shown in Figure 2.6. These figures also show the  $F_{\text{prompt}}:\text{PE}$  location of some important background events.

The ROI contour bounds are defined by different background sources. The lower bound in  $F_{\text{prompt}}$  does an effective job of eliminating any electronic recoil backgrounds from the dark matter search. Non-WIMP nuclear recoil events still have the potential to leak into the dark matter search region. Of particular interest are alphas stemming from nuclei undergoing alpha decay that lose some energy before entering the argon. These attenuated alphas, as well as the other backgrounds accounted for in the dark matter search, are discussed in the next chapter.

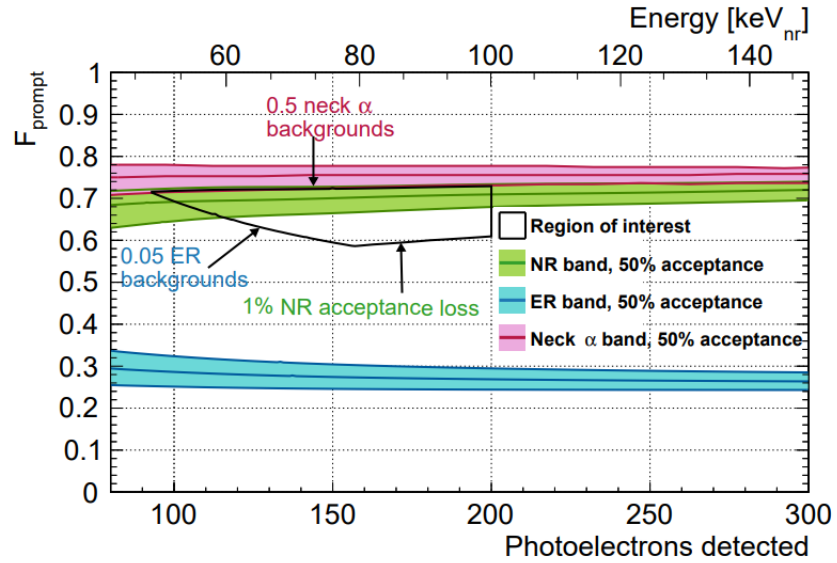


Figure 2.5: Dark matter region of interest from 231 live day paper. The ROI (black) is illustrated with ER (blue), NR (green) and neck alpha (pink, defined in Chapter 3) bands that define the boundaries. Each band is drawn about the median of each event type, with 25% of events shaded above, and 25% shaded below. The lower bound of the ROI designed for ER rejection at low PE. Figure taken from 231 live day paper [16].

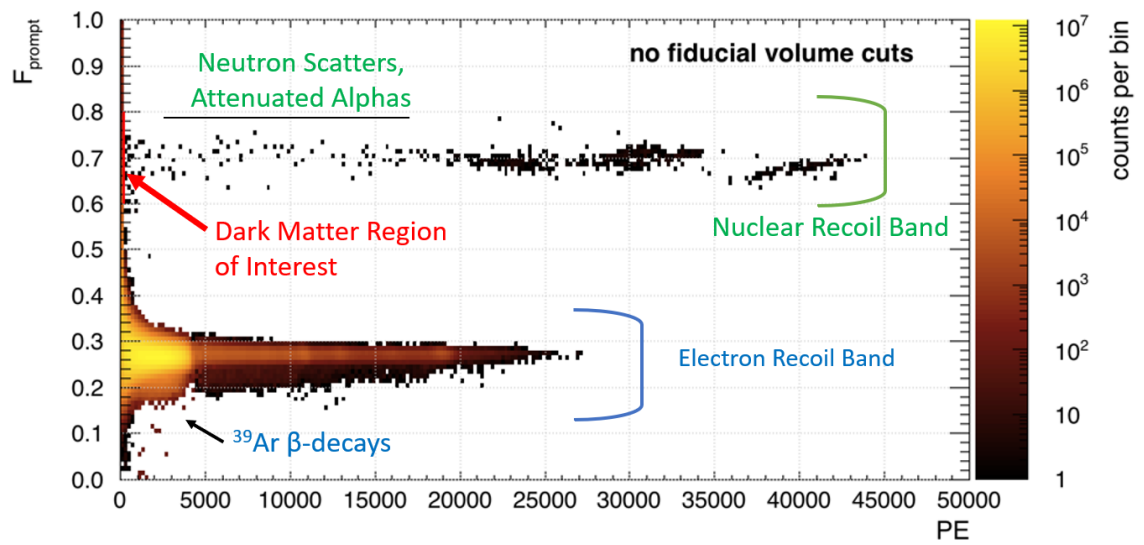


Figure 2.6:  $F_{\text{prompt}}:\text{PE}$  distribution of 4.4 live-day dataset. The electronic recoil band at lower  $F_{\text{prompt}}$  labelled in blue, with the nuclear recoil backgrounds at higher  $F_{\text{prompt}}$  labelled in green. The dark matter region of interest (80-200 PE) is in red. Attenuated alphas and neutron scatters have potential to leak into this region. [35]

# Chapter 3

## Background Sources in the DEAP-3600 Detector

In a direct detection experiment, backgrounds must be extremely low to attain high WIMP sensitivities. The design goal of the DEAP-3600 detector was  $< 0.6$  background events over a 3-tonne-year exposure [21]. This background budget is comprised of equal parts neutrons, alphas, and ER backgrounds. A large amount of work was done in the design and construction of the detector towards meeting this goal. The reduction in muon flux from placing the detector underground, and the benefits of different chosen materials in neutron shielding has already been described. However, background sources can still pass into the scintillation material and create events in the dark matter search. Some of the major background types are described in this chapter. They are  $^{39}\text{Ar}$   $\beta$ -decays, Cherenkov radiation, neutron scatters, and of course,  $\alpha$ -decays.

### 3.1 $^{39}\text{Ar}$ $\beta$ -Decays

The choice of liquid argon as the scintillation material was largely due to the potential for pulshape discrimination. This discrimination allows for the rejec-

tion of electronic recoils in the dark matter search, focusing only on nuclear recoils, like WIMP nuclei scatters. These electronic recoils come from many different decay products, but the largest of these are  $^{39}\text{Ar}$   $\beta$ -decays.

Liquid argon has trace amounts of unstable  $^{39}\text{Ar}$  isotopes. These isotopes can beta decay, emitting electrons into the scintillation material. These electrons scatter off electrons from other argon atoms, creating electronic recoil events in the detector. The activity of these  $^{39}\text{Ar}$  events in atmospheric argon has been measured many times, and is  $0.95 \pm 0.05$  Bq per kg of natural argon [36]. This background ends up being the largest within the detector before any discrimination. It can be seen in Figure 2.6 as the bright spot beneath 5000 PE centered around  $F_{\text{prompt}} = 0.25$ .

At higher energies ( $>1000$  PE), pulshape discrimination makes removing this background from the dark matter search simple. However at lower energies the  $F_{\text{prompt}}$  spectrum from these events widens, as can be seen in Figure 2.6. In this figure, the  $^{39}\text{Ar}$   $\beta$ -decays at low PE leak into higher prompt values. This spread comes from statistical fluctuations in the  $F_{\text{prompt}}$  measurement, as these low PE events have less photons detected. The lower contour of the WIMP ROI (Figure 2.5) counteracts this. It is specifically designed to maximize the nuclear recoil acceptance, while keeping the number of electronic recoil events within the background budget. Pulshape discrimination provides  $10^{-10}$  electronic recoil leakage probability with a 50% nuclear recoil acceptance at 110 PE [34].

There are other sources of electronic recoil events. At higher energies ( $>5000$  PE), gammas and electrons coming from different isotope decays can create ER events. These events can come from a range of isotopes, including the  $^{42}\text{Ar}/^{42}\text{K}$  decay, and radioisotopes both in the PMT glass and from radon gas diffuse in detector components [37]. These sources can produce high energy gammas in their decay chain, creating recoils in the liquid argon mass. In these cases, the energy is high enough to not impact the dark matter search.

## 3.2 Cherenkov Radiation

Cherenkov light is generated by a particle travelling in a medium faster than the group velocity of light in that medium. This light signal can be generated by particles in the acrylic light guides, and be registered as an event in the detector. The light produced by this interaction is quickly sent to PMTs due to its position. In this way, it should theoretically have a  $F_{\text{prompt}}$  value close to 1, as there is no spread to the light production. This is observed for most Cherenkov events. In some cases Cherenkov light may occur in coincidence with an  $^{39}\text{Ar}$  decay, which pulls the  $F_{\text{prompt}}$  value down into the region of interest.

To counter-act this, a cut is applied to data for the dark matter search, using the variable "fmaxpe". This variable is the fraction of light from the brightest PMT, over the full amount of light. In this way, events that deposit the majority of their light in one PMT can be removed. Cherenkov light occurring in the light guide would deposit most of its light in the PMT adjacent to the light guide, making a cut on this variable very effective. As a result, Cherenkov light also becomes a near negligible component of the dark matter search background model. This fmaxpe cut is efficient in the dark matter search, as scintillation light in LAr is fairly isotropic [16].

## 3.3 Radiogenic and Cosmogenic Neutrons

Being heavy neutral particles that can travel at a range of energies, neutrons can closely mimic WIMP signals in a scintillation detector. Neutrons enter the detector from some external source and recoil off Ar nuclei. These neutrons can be separated into two categories based on their source. Radiogenic neutrons are produced from radioisotopes diffuse in components within and around the detector, with both fission and  $(\alpha, n)$  reactions contributing to the background. The dominant locations where neutrons decay include the borosilicate PMT glass, and the filler blocks around the

acrylic vessel [16].

Cosmogenic neutrons are produced from cosmic ray interactions. These are also mitigated by the 2 km of rock overburden SNOLAB provides, which reduces the flux greatly. Any neutrons that can still enter the detector are rejected by the muon veto system, through coincident muon detection. These design choices reduce the neutron background well within the background budget [16].

### 3.4 Alphas

The focus of this thesis is on the impact of attenuated alphas on the DEAP-3600 dark matter search. In the experiment, alphas are produced from different radioactive isotopes present within the detector. The significant radioisotopes for DEAP-3600 are  $^{232}\text{Th}$  and  $^{238}\text{U}$ . These are primordial radioisotopes, radioactive elements from the Earth's creation with extremely long lifetimes [38]. The decay chains for these isotopes are displayed in Figure 3.1. The progeny of these isotopes are diffuse within the detector materials. As such, the high energy alphas in this decay chain can appear throughout the detector, and deposit their energy into the scintillation material through nuclear recoils. In this way, they can mimic a WIMP signal.

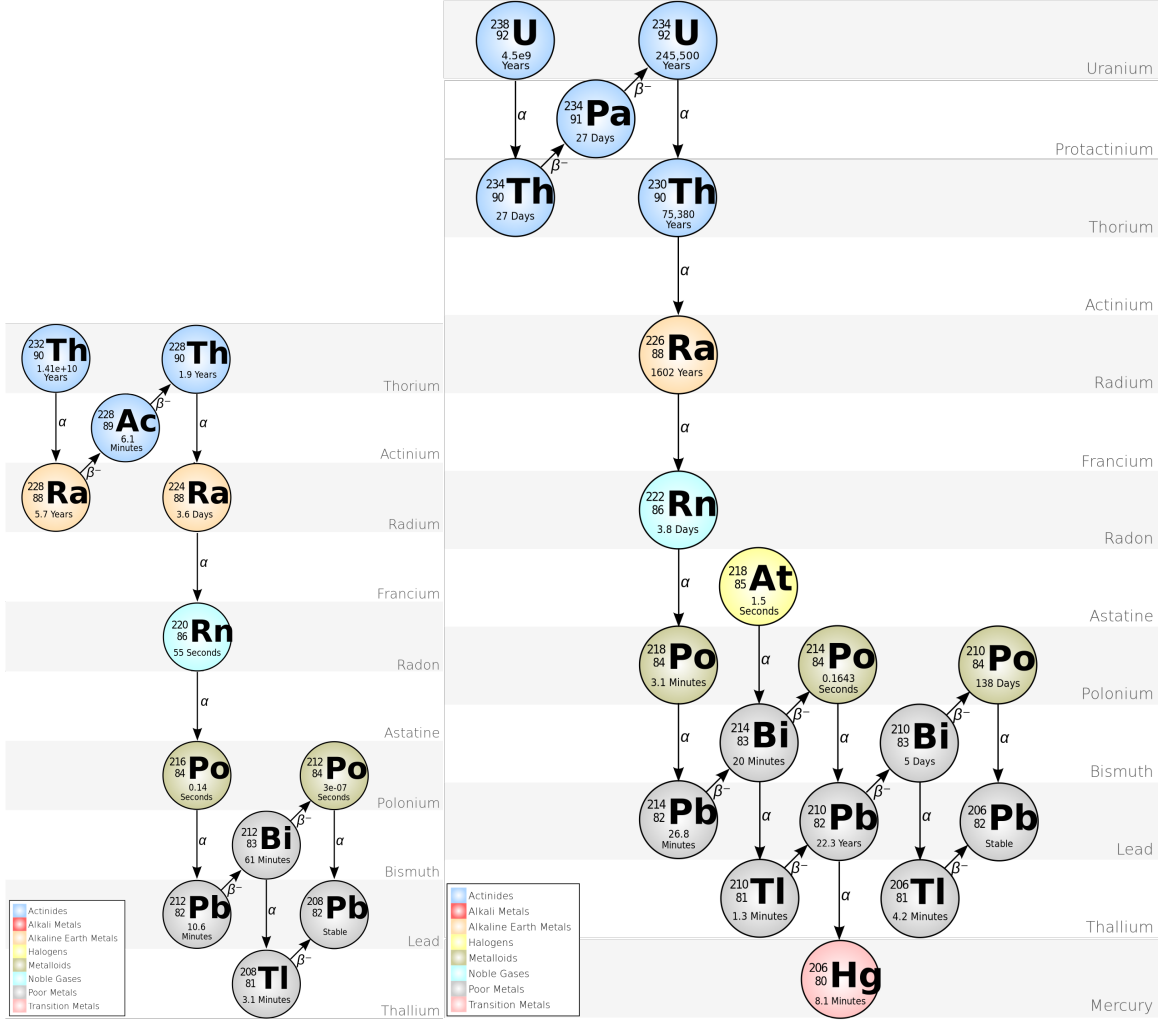


Figure 3.1:  $^{232}\text{Th}$  (left) and  $^{238}\text{U}$  (right) decay chains. [39]

The design of the detector was done with radon contamination in mind. Materials were chosen that are radiopure, and the production of the vessel and TPB was performed with high radiopurity targets. However, the assembly of the different components was done underground at SNOLAB. This involved exposing the acrylic to the air in the underground lab [26]. This air is contaminated with  $^{222}\text{Rn}$  at levels of roughly  $130 \text{ Bq/m}^3$  [21]. Radon gas can emerge through the  $^{232}\text{Th}$  and  $^{238}\text{U}$  decays, producing  $^{220}\text{Rn}$  and  $^{222}\text{Rn}$  nuclei respectively, and these nuclei became diffuse within the detector and its components. This contamination allows for  $^{222}\text{Rn}$   $\alpha$ -decays to occur within the scintillation material. Further, these nuclei can decay into their pol-

lonium daughters, and ultimately some lead daughters. These Po and Pb nuclei can adhere to solid surfaces, like the acrylic, and lessen the radiopurity of these materials [40].

$^{222}\text{Rn}$ , coming from the  $^{238}\text{U}$  decay chain, undergoes  $\alpha$ -decay. This releases a high energy alpha directly within the liquid argon bulk (see Figure 3.1). Its short-lived daughter nuclei  $^{218}\text{Po}$  and  $^{214}\text{Po}$  can also release high energy alphas shortly after this decay.  $^{220}\text{Rn}$ , (from the  $^{232}\text{Th}$  chain) and its progeny also produce high energy alphas, however it is found that  $^{222}\text{Rn}$  and its progeny are the dominant  $\alpha$ -decay in the experiment [16]. These alphas deposit their energy into the liquid argon mass, appearing as high energy nuclear recoil events within the detector. Since alphas in this chain are emitted in the MeV range, and within the liquid argon bulk, they create very large amounts of scintillation light. The resulting events have PE well past the dark matter search area of 80-200 PE. They can be seen in the high energy ( $>20000$  PE) end of the nuclear recoil band in Figure 2.6.

It is possible for an alpha particle to only deposit a portion of its energy into the liquid argon.  $^{210}\text{Po}$  diffuse within detector components can  $\alpha$ -decay, emitting an alpha from within the component material. During this process, the emitted alpha would deposit some energy in the material before entering the liquid argon. In this way, an attenuated alpha would enter the scintillation material, and create a much smaller scintillation response than its full energy counterpart. This energy degradation can create events with PE signals that leak into the WIMP region of interest. These attenuated alphas can be seen in Figure 2.6, in the NR band, leaking from high energy down to the event trigger PE threshold.

There are three major sources for these attenuated alphas. The first is from  $\alpha$ -decays occurring within the acrylic vessel inner surface and TPB layer. The second is  $\alpha$ -decays occurring specifically within the neck flowguide surface, also made of acrylic. The third is from  $\alpha$ -decays occurring within dust particulates that are diffuse

throughout the liquid argon bulk. All three of these sources can create a WIMP-like response in the detector, and each must be treated differently.

### 3.4.1 From Acrylic Vessel Inner Surface and TPB Layer

The simplest of these sources is from the acrylic vessel inner surface and TPB layer.  $^{210}\text{Po}$   $\alpha$ -decays from these regions deposit some of their energy within the originating surface, before passing into the liquid argon. This situation is illustrated in Figure 3.2. Case a) represents an  $\alpha$ -decay occurring within the liquid argon bulk, the ideal case where all energy is deposited in the argon. In case b), the decay occurs in the TPB layer. Here there is potential for either the alpha or the daughter nucleus to enter the liquid argon. The particles in this case deposit some energy in the TPB and create some TPB scintillation before entering the scintillation material. In case c) the decay occurs within the acrylic vessel surface. These alphas lose energy to both the acrylic and TPB layers before entering the liquid argon, resulting in heavily attenuated alphas and low scintillation responses. The latter two cases can result in an event with PE inside the WIMP region of interest.

Work was done to lower this background source by resurfacing the acrylic inner vessel. An in-situ resurfacing was done, where 0.5 mm of the inner surface was removed. This was done to reduce the built up lead and polonium nuclei that adhere onto the vessel [31, 41]. The process was very effective, greatly reducing the contamination presence. However, some alphas still remain in the analysis, and must be reduced using position reconstruction. A measurement of the activity from these sources, as well as mitigating them using radial cuts, is done in Chapter 5.

### 3.4.2 From Acrylic Neck Flowguide Surface

Another source of attenuated alphas that can mimic WIMP nuclear recoils is from  $\alpha$ -decays occurring at the neck flowguide. This acrylic component is located at the

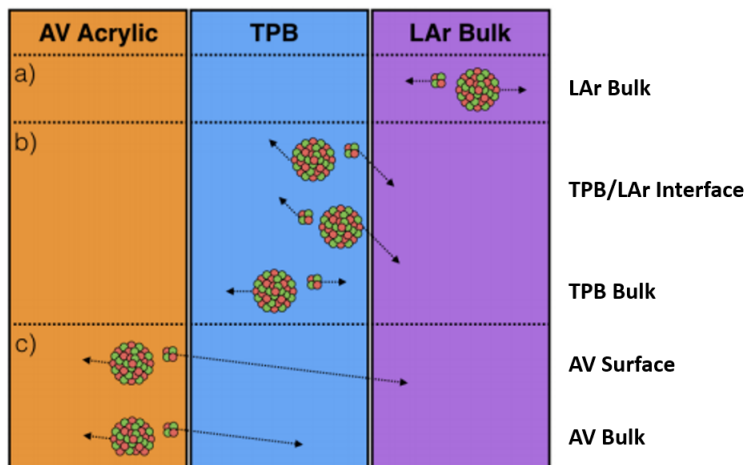


Figure 3.2: Graphic breaking down outcomes of  $^{210}\text{Po}$  surface alphas with different decay points. This includes a)  $\alpha$ -decays occurring within the liquid argon, b) within the TPB layer and c) within the acrylic vessel inner surface. To the right the different decay locations are labelled. [42]

top of the detector in the gaseous argon region.  $^{210}\text{Po}$  nuclei diffuse in this surface can  $\alpha$ -decay, and much like from the acrylic vessel inner surface, deposit some energy into the acrylic before entering the argon region.

The key difference between this source and the standard inner vessel is the nuanced geometry of the acrylic neck and the neck flowguide location. Alphas exiting this source are entering the gaseous argon region, as the neck is above the liquid argon fill level. There is some population of liquid argon at the flowguide that these alphas pass through, likely in the form of a thin liquid argon film. Alphas passing through this film produce scintillation light in the nuclear recoil band. There is no TPB layer on the acrylic flowguides. Because of this, a large portion of the UV scintillation light emitted from the liquid argon layer is absorbed by other parts of the acrylic flowguide. This process is called shadowing. The shadowing of these events distorts and reduces the number of scintillation photons reaching the PMTs. This causes events with PE levels within the WIMP region of interest. This alpha source is quantified in Chapter 5, culminating in a measured event rate.

In the most recent DEAP-3600 results, alphas from this source made up the largest

portion of the background model in the WIMP ROI [16]. Some methods to mitigate this alpha background have been developed [43, 44], including some machine learning algorithms. These algorithms are designed to reduce this background efficiently. Preliminary results of these algorithms, and how they impact the dark matter search, are found in Chapter 6.

### 3.4.3 From Dust Particulate Diffuse in LAr

An excess of events has been observed in the intermediate PE range, between 5000 - 20000 PE. These events are in the nuclear recoil band, and behave like attenuated alphas, but are unexplained by the alpha model published in [16]. It has been proposed that these unaccounted for alpha events originate from dust particulates. These particulates would be diffuse within the liquid argon bulk, and have some  $^{222}\text{Rn}$  contamination, such that  $\alpha$ -decay within the dust particle could occur.

There is the potential for metallic dust to be present within the liquid argon bulk. Metallic surface erosion could create dust in the cryogenic liquid storage tanks [21]. At the time of resurfacing, a 10 tonne nitrogen purge inside the vessel was used to reduce radon activities. During this process, the nitrogen was passed through a filter of 50  $\mu\text{m}$ . This would allow for dust particulates beneath this filter size. Dust samples have been collected around the DEAP-3600 deck and detector floor, as well as within the liquid nitrogen tanks. Residue of copper and zinc dust were found in the liquid nitrogen using filter paper. As such, there is real potential for the presence of sub-50  $\mu\text{m}$  copper dust particulates within the liquid argon bulk.

The process for a potential  $\alpha$ -decay in a dust particulate is shown in Figure 3.3. The emitted alpha would deposit some fraction of its energy within the dust material before exiting into the liquid argon. The rest of the alpha energy is then deposited into the argon. This would produce some scintillation light. Some of this light is then shadowed by the dust particulate behind it, further reducing the scintillation photons

reaching PMTs.

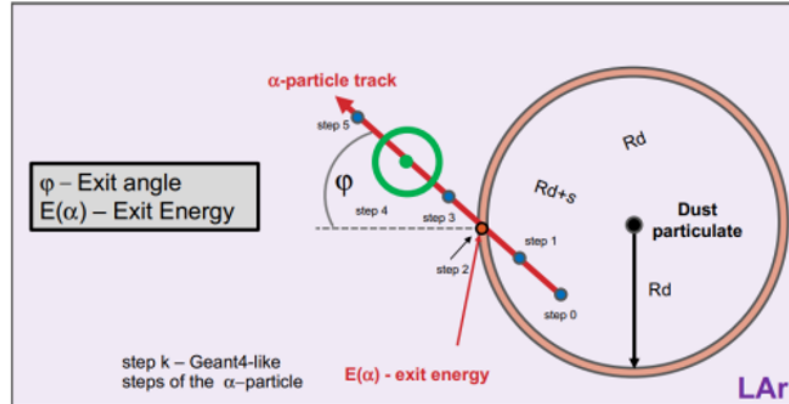


Figure 3.3: Graphic of  $\alpha$ -decay occurring within a dust particulate in the liquid argon bulk. The alpha is emitted in the dust, losing some energy to the dust material at steps 0-2. At this point, it exits into the liquid argon and begins creating scintillation light, with a degraded exit energy. The level of shadowing is dependent on the exit angle. Courtesy of Robert Stainforth.

In this way, dust alphas can span a wide range of energies. Further, the particulates are assumed to be uniformly distributed across the liquid argon, removing the potential for any positional cuts. The dust hypothesis becomes the dominant background in the dark matter search. The measured event rates, and yield in the dark matter search region of interest, are found in Chapter 6, along with the other alphas.

# Chapter 4

## $\alpha$ -Decays from the Inner Acrylic Vessel Surface and TPB Layer

### 4.1 Activity Measurement

The first source of attenuated alphas to be examined is alphas originating from the inner acrylic vessel surface and TPB layer. Alphas from  $^{210}\text{Po}$  nuclei decays in these materials lose some energy into the acrylic and TPB. Upon entering the liquid argon, only a fraction of their energy is left, and converted to scintillation light. The alphas produced in these decays, and their resulting events in the detector, will be referred to as "surface alphas" within this paper.

The amount of energy these alphas deposit into the scintillation material is dependent on their starting position.  $^{210}\text{Po}$  decays occurring deeper in the acrylic vessel are more likely to deposit less of their energy, whereas a decay occurring in the TPB layer will still deposit the majority of its energy into the liquid argon provided the alpha particle is travelling inwards. Using Figure 3.2 as a guideline, surface alphas are separated into four components, based on their decay location, shown in Table 4.1. These values are only used in RAT to generate simulated samples of the surface

alphas.

Table 4.1: Simulated positions of  $^{210}\text{Po}$  surface alpha components, based off Figure 3.2. The spherical acrylic vessel begins at 851.000 mm from the center of the liquid argon bulk

Component	Decay Location (mm from center of LAr Bulk)
LAr/TPB Surface	$R = 850.997$
TPB Bulk	$850.997 < R < 851.000$
AV Acrylic Surface	$R = 851.000$
AV Acrylic Bulk	$851.000 < R < 851.050$

Decays labelled as type b) in Figure 3.2 are designated as LAr/TPB Surface (upper two) or TPB Bulk (lower). When the alpha is oriented towards the liquid argon, they have little attenuation, and deposit the majority of their energy into the scintillation material. In the case where the alpha takes a longer path in the TPB layer, or is oriented away from the LAr Bulk, TPB scintillation light is created.

Decays labelled as type c) in Figure 3.2 are designated as AV Acrylic Surface (upper) and AV Acrylic Bulk (lower). In these cases, the alphas experience a large amount of attenuation in the acrylic, and deposit a small fraction of energy into the LAr Bulk.

These depths are chosen based on the geometry of the detector and the TPB layer. In the simulation, the acrylic vessel is defined as 851 mm from the center of the LAr. The applied TPB coating has a thickness of  $3 \mu\text{m}$ , applied on the inside of the vessel wall [30]. The upper bound of  $50 \mu\text{m}$  into the acrylic was chosen from simulations that predicted no triggers from  $^{210}\text{Po}$  alpha decays beyond this depth [16]. As such, any reference to the "AV Bulk" component only considers acrylic up to this  $50 \mu\text{m}$  depth, not the entire depth of the acrylic vessel.

#### 4.1.1 Defining the Surface Alpha Control Region

Monte Carlo simulations of the decays are generated at each location listed in Table 4.1. The resulting PE spectra can be seen in Figure 4.4, where the impact

of attenuation from the acrylic can be seen. The AV Surface and TPB components of the decays deposit a very large fraction of their energy into LAr. The AV Bulk component, which undergoes the most energy degradation, is spread in PE. All four components have the potential to leak into the dark matter PE region of interest, with their impact on the dark matter search explored in Chapter 6.

The 376 live day dataset can also be looked at in this region, defining a surface alpha preselection (Table 4.2). This selection, along with a PE range, will act as our surface alpha control region, and be used to fit the simulated samples to data.

Table 4.2: Definition of the surface alpha control region.

<b>Event Selection</b>	<b>Purpose</b>
Fraction of PE in one PMT < 75%	Remove events that deposit majority of light in one PMT (mostly Cherenkov events)
Fprompt > 0.55	Require high prompt light fraction to remove electronic recoils, select only neutron recoils (See Figure 2.6)
Single-scatter event	Pileup cut removing coincidence events
Reconstructed Z < 550 mm	Ensure events are reconstructed below LAr fill level, while maintaining consistency with true position (see Figure 4.1)
PE detected > 9000	PE cut to remove any neck alphas, while also low enough to capture the full $^{210}\text{Po}$ surface alpha tail.
PE detected < 25000	PE cut to remove full-energy alpha decays in LAr (see Figure 4.3)

The choice of reconstructed  $Z < 550$  mm is made for multiple reasons. Most importantly, the current liquid argon fill level stands at 558 mm [45], and only alphas scintillating within the liquid argon should be considered. In previous studies, including the 231 live day study [16], a cut of reconstructed  $Z < 500$  mm was used for these alpha studies. Position reconstruction bias shows that considering a wider cut improves the uncertainty on this study. Comparing a CDF of the reconstructed Z positions of both data and a simulated AV Surface sample with the simulation location in Figure 4.1 displays this bias. The preselection defined above is applied to these

samples, but without the reconstructed Z cut. Both data and the AV surface sample show a bias at 500 mm, with a roughly 5% disagreement between the reconstructed positions and the true position. A cut here would be subject to a larger uncertainty because of this. Instead, cutting at 550 mm (indicated by the yellow line) removes this bias, as the position reconstruction algorithm converges to unity with the true position of the events.

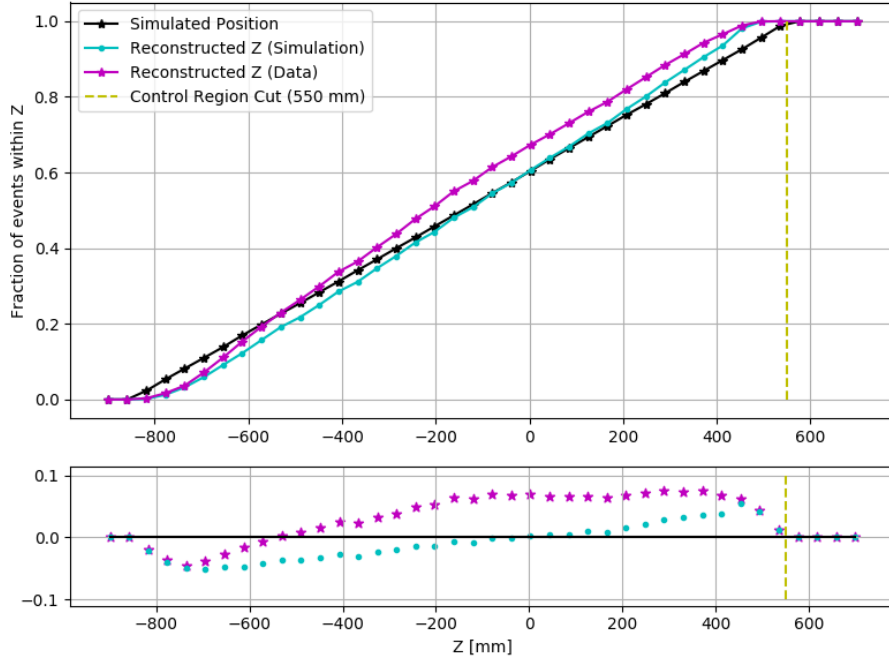


Figure 4.1: Z position reconstruction consistency in the surface alpha control region (see Table 4.2). Cumulative distribution functions (top) are plotted for the reconstructed Z position of both a simulated AV Surface sample (cyan) and data (magenta) in the control region. These can be compared directly to the true position of the AV Surface sample (black) to see the bias in the position reconstruction algorithm. An initial cut of 500 mm on reconstructed Z was used, but to reduce uncertainty from bias, a cut on 550 mm (yellow) is used instead. The difference between the reconstructed and true positions is also displayed in the bottom row.

Plotting the full PE spectrum (10000 - 50000 PE) of the dataset with this preselection displays not only the  $^{210}\text{Po}$  alpha population, but also the higher energy LAr Bulk alpha populations. These decays occur in the LAr Bulk, and the alpha deposits its full energy. Plotting against the reconstructed radius allows for easy separation between

the alphas, and is seen in Figure 4.2.

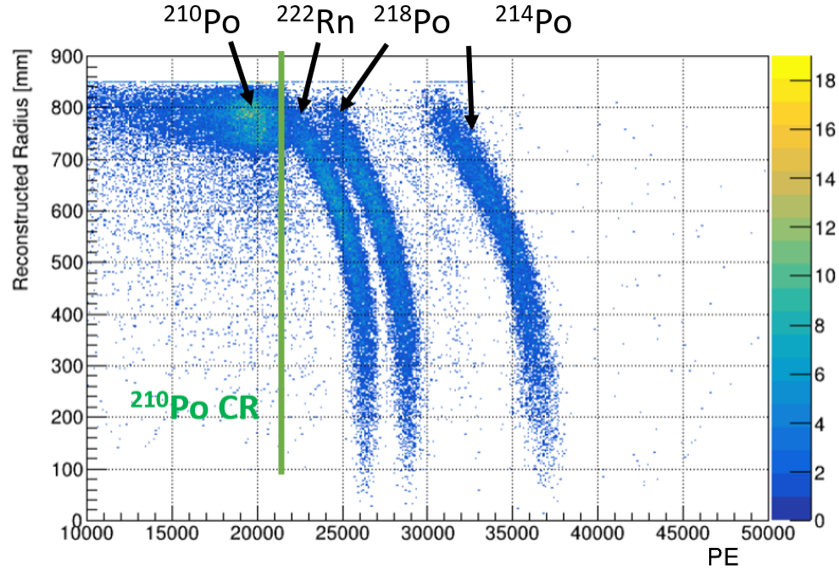


Figure 4.2: Three year dataset after the surface alpha preselection in the a PE range, before the saturation and clipping corrections. The green line defines the upper limit of the  $^{210}\text{Po}$  control region. High energy alpha decays, occurring throughout the LAr Bulk, can be seen to the right of the green line. Attenuated surface alphas leaking into lower energies are seen left of the green line.

These higher energy LAr Bulk decays, displayed in Figure 3.2 as a), have a much higher and narrower PE band, as they are not affected by materials other than liquid argon. While a  $^{210}\text{Po}$  alpha control region can be defined by the green line in Figure 4.2, the control region is impure, as some  $^{222}\text{Rn}$  decay events leak in at higher reconstructed radius. This contamination is a consequence of saturation and clipping effects in the PMTs at these high energies. In the previous version of this process, this was accounted for by including a  $^{222}\text{Rn}$  alpha decay component in the fit [16]. The recent development of a pulse level saturation correction processor [42] allows for the separation of these populations.

Saturation occurs when a PMT is bombarded by a large amount of incidence light, creating a non-linear response in the PMT. Clipping is a result of the PMT digitizer reaching its gain limit, and cutting the pulse. In both cases, the full information of

the pulse is not recorded, and a lower PE than actual is registered. These effects become more pronounced at higher radius. The large amount of scintillation light produced in these high energy alpha interactions is directed at a small selection of PMTs.

Applying the processor corrections gives clear definition between the  $^{210}\text{Po}$  and  $^{222}\text{Rn}$  populations, seen in Figure 4.3. This allows for a wider and purer  $^{210}\text{Po}$  alpha control region. As such, the upper bound of the surface alpha control region will be set at 25000 PE, and the  $^{222}\text{Rn}$  component can be excluded.

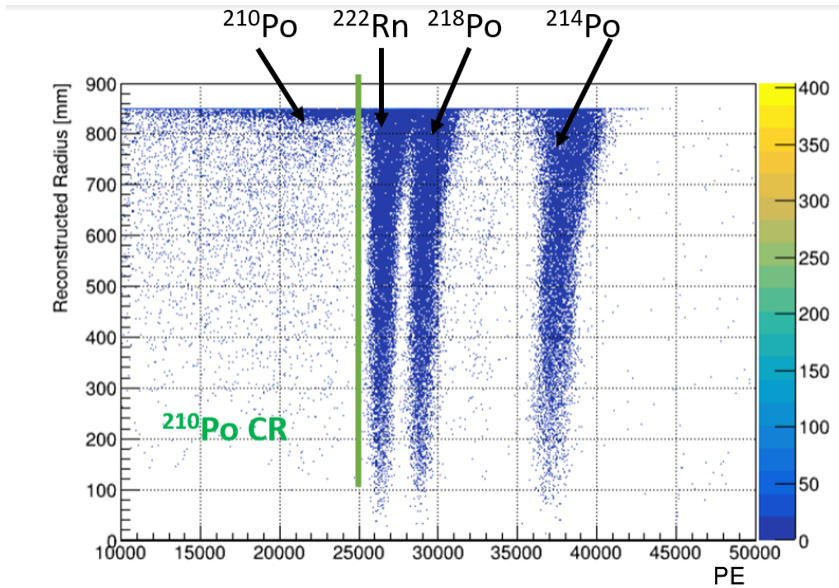


Figure 4.3: Three year dataset after the surface alpha preselection in a wide PE range, after the clipping and saturation corrections. High energy alpha decays, seen above the green line, are well defined and do not leak into  $^{210}\text{Po}$  region beneath the green line.

#### 4.1.2 Activity Calculation

With this, an activity can be calculated for each of the four surface alpha components. For AV/TPB surface and TPB Bulk components, this is done through the

equation:

$$A^u \cdot S_{area}^u = \frac{N_{CR}^u}{t_{live} \epsilon^u}, \quad (4.1)$$

For the AV Bulk component, a similar equation is used:

$$A^u \cdot S_{vol}^u \cdot \rho_{AV} = \frac{N_{CR}^u}{t_{live} \epsilon^u}, \quad (4.2)$$

In this equation:

- $A^u$  - activity of a surface alpha component, in dimensions of Bq/m<sup>2</sup> for AV/TPB surface and TPB Bulk components, and in dimensions of Bq/kg for AV Bulk components
- $S_{area/vol}^u$  - area/volume where decay occurs, units of m<sup>2</sup> for AV/TPB Surface and TPB Bulk, units of m<sup>3</sup> for AV Bulk
- $\rho_{AV}$  - Density of the acrylic vessel, used to convert AV Bulk volume to a mass, in units of kg/m<sup>3</sup>
- $t_{live}$  - total livetime of the dataset [s]
- $\epsilon^u$  - percent of events in sample passing control region cuts [%]
- $N_{CR}^u$  - total number of events observed in the control region from this component

The latter ( $N_{CR}^u$ ) can be expressed in terms of the total number of data events in the control region. This is done by applying a fit of the four simulation samples to data in that region, and attaining a component weight, that can be applied to the number of events. The equation looks like:

$$N_{CR}^u = N_{CR} \omega^u f_{pileup}, \quad (4.3)$$

where:

- $N_{CR}$  - overall number of events that trigger the detector in the control region
- $\omega^u$  - component's weight from the fit [dimensionless]
- $f_{pileup}$  - pileup correction to account for events lost after pileup cuts [dimensionless]

These different variables will be defined, beginning with the number of events in the control region, and the different component weights from the  $^{210}\text{Po}$  surface alpha fit.

### Events in Control Region

After applying the control region preselection listed in Section 4.2, along with data cleaning cuts, to the 376 live day dataset, we are left with 30906 events in the surface alpha control region.

This result is scaled with the component weights and the pileup correction to get the total number of events in the control region for each individual component.

### $^{210}\text{Po}$ Alpha Fit Results

The four surface alpha samples are fit to the data in the control region, using a one dimensional fit in the PE spectrum. The fit is composed of six parameters: the four weights of the normalized alpha samples, and a pair of Gaussian smearing parameters (mean, width). As mentioned earlier, there is a  $3\ \mu\text{m}$  layer of TPB added to the inside of the acrylic vessel. While  $3\ \mu\text{m}$  is the average thickness, in reality there are peaks and valleys across the layer that create roughness. This is not present in simulations, where the TPB layer is perfectly smooth. It is possible that, because of these variations, the actual average thickness of the TPB could be more or less than  $3\ \mu\text{m}$ . This difference in mean thickness would result in a shift in the PE distribution. This shift in mean is accounted for in the mean parameter of the

Gaussian smear. This untracked roughness would also widen the PE distributions, as some alphas would be subject to more/less TPB, and lose more/less of their energy before entering the liquid argon. This broadening is accounted for in the width parameter of the Gaussian smear. These smear terms are constant throughout the four simulated samples, so that all the samples are broadened and shifted equally. These parameters are constrained to 0.9-1.1 for the mean, and 0-0.1 for the width. The initial values are set to 1 and 0 respectively. The fit scans through these values of smearing parameters to find the combination that yields the best  $\chi^2$  value, while altering the  $^{210}\text{Po}$  simulated samples.

The best fit results when considering all 4 components can be seen on Figure 4.4, with the resulting parameters also displayed in Table 4.3.

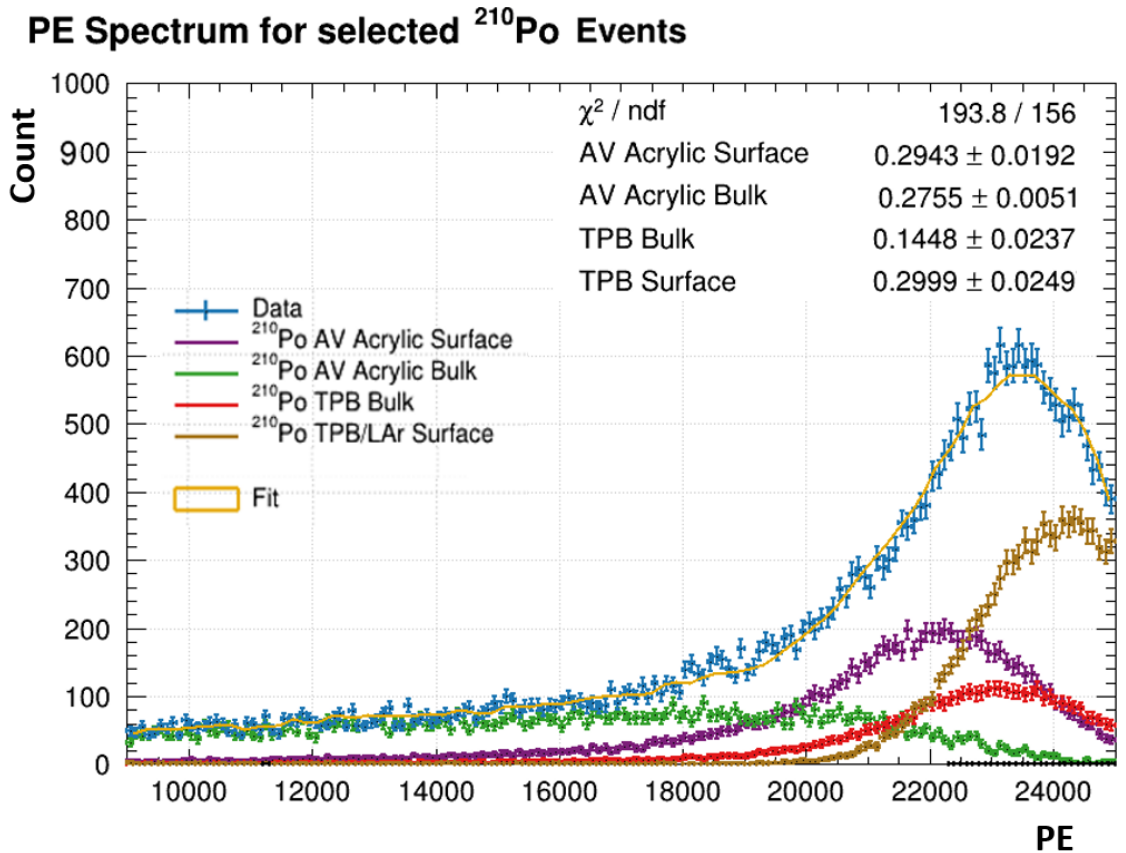


Figure 4.4: Results of  $^{210}\text{Po}$  surface alpha fit. Component weights and smearing parameters for this fit are displayed in Table 4.3.

Table 4.3: Results of component weight fit from Figure 4.4. The smearing mean and width are determined by performing the fit over many different combinations of the two variables, and finding the combination with the best  $\chi^2$ . The step size is 0.001 for the mean and 0.00025 for the width. The component weights are the results of the fit at this optimized combination of smearing parameters. Here the uncertainties on the component weights are statistical only. These parameters are used in activity calculations.

$^{210}\text{Po}$ fit values		
Parameter	Description	Value
$\mu_{TPB}$	Smearing mean for $^{210}\text{Po}$ PDFs	1.065
$\sigma_{TPB}$	Smearing width for $^{210}\text{Po}$ PDFs	0.060
$\omega^0$	Component weight of $^{210}\text{Po}$ AV acrylic surface PDF	$29.43 \pm 1.92$ %
$\omega^1$	Component weight of $^{210}\text{Po}$ AV acrylic bulk PDF	$27.55 \pm 0.51$ %
$\omega^2$	Component weight of $^{210}\text{Po}$ TPB bulk PDF	$14.48 \pm 2.37$ %
$\omega^3$	Component weight of $^{210}\text{Po}$ TPB/LAr interface PDF	$29.99 \pm 2.49$ %

The fit performs very well in this expanded PE control region, returning a  $\chi^2/\text{ndf}$  of 1.2. Fit uncertainties in the component weights are propagated through the activity calculation. The fit demands a 6.5% increase in the mean of the distribution, pushing the full energy TPB/LAr surface component to the high end of the control region spectrum. Added alpha systematic uncertainties may factor into this fit, most notably the treatment of alpha quenching in liquid argon. Alpha quenching in our simulations is explored in Appendix A.

### Pileup Correction

The single-scatter event cut is designed to remove any potential events that are signs of a coincidence event. In the present study it eliminates 3.5% of events. While this removes any pileup events that dilute the PE distribution, these are still  $^{210}\text{Po}$  triggers. This loss should be taken into account when the activity is calculated.

$$f_{pileup} = \frac{1}{0.965} = 1.036 \quad (4.4)$$

## Control Region Efficiency

The control region efficiency ( $\epsilon^u$ ) is calculated using the simulated samples by finding the efficiency of the surface alpha control region preselection cuts (from Table 4.2). Applying this to the number of events in the preselection gives an estimate of the total number of triggers that occur in the full detector.

This is done for each sample so an efficiency is generated for each component. The final results are:

- AV Surface:  $43.47 \pm 0.27$  %
- AV Bulk:  $10.80 \pm 0.12$  %
- TPB Bulk:  $46.03 \pm 0.29$  %
- TPB Surface:  $47.94 \pm 0.27$  %

## Geometrical Factors

Surface areas and mass values are calculated using equations designed by Robert Stainforth in a previous study. This process is repeated here, with updated parameters. The values of these parameters used are defined as [21, 30, 45]:

$$R_{AV} = 846 \pm 2 \text{ mm}$$

$$R_{TPB} = 3_{-1.5}^{+3} \text{ } \mu\text{m}$$

$$h_{lvl.} = 846 \pm 2 \text{ mm} + 550 \pm 2 \text{ mm} = 1346 \pm 3 \text{ mm}$$

$$d_{AV,bulk} = 0.050 \text{ mm}$$

$$\rho_{AV} = 1140 \text{ kg/m}^3$$

Where  $h_{lvl.}$  is the sum of the acrylic vessel radius, and the reconstructed Z cut location of 550 mm. An uncertainty of .04% is applied to the 550 mm height, coming

from the relative difference between the simulated and reconstructed position of the events at  $Z = 550$  mm in Figure 4.1.

The role of these parameters, and the equations needed for each component, are:

- $^{210}\text{Po}$  AV Surface [Surface Area]: Surface area of the AV acrylic at the TPB interface up to the fill level, calculated as:

$$S_{area}^u = S_{area}^{trun.}(R_{AV}, h_{lvl.}) = 2\pi R_{AV} h_{lvl.} \quad (4.5)$$

where  $R_{AV}$  is the acrylic vessel radius, and  $h_{lvl.}$  is the fill level considered in the surface alpha control region (550 mm).

- $^{210}\text{Po}$  AV Bulk [Volume]: Volume of the AV acrylic up to the simulation point of  $50 \mu\text{m}$ . That is, only considering a  $50 \mu\text{m}$  depth of acrylic, as that is the only amount that causes scintillation response. This is calculated as:

$$S_{vol}^u = S_{vol}^{trun.}(R_{AV} + d_{AV,bulk}) - S_{vol}^{trun.}(R_{AV}) \quad (4.6)$$

$$S_{vol}^u = \frac{\pi h_{lvl.}^2}{3}(3(R_{AV} + d_{AV,bulk}) - h_{lvl.}) - \frac{\pi h_{lvl.}^2}{3}(3R_{AV} - h_{lvl.}) \quad (4.7)$$

$$S_{vol}^u = \pi d_{AV,bulk} h_{lvl.}^2 \quad (4.8)$$

where the two components of the equation are the volume of the acrylic shell with the simulated depth and the volume without, and the form is simplified. The calculated AV Bulk volume is converted to a mass for the final activity calculation by multiplying the AV density  $\rho_{AV}$ .

- $^{210}\text{Po}$  TPB Bulk [Volume/Surface]: Due to the TPB layer's high roughness and low thickness, the bulk component is approximated as the surface area of the TPB layer, and calculated as:

$$S_{area}^{trun.}(R_{AV}, h_{lvl.}) = 2\pi R_{AV} h_{lvl.} \quad (4.9)$$

where  $R_{AV}$  is the acrylic vessel radius. The actual radius is  $3 \mu\text{m}$  less than this value (by subtracting  $R_{TPB}$ ), but this difference is negligible compared to the uncertainty in the measurements, and can be ignored.

- $^{210}\text{Po}$  TPB/LAr Interface [Surface]: Surface area of the TPB layer, equal to the calculation for  $^{210}\text{Po}$  TPB Bulk.

And the results of these calculations are given in Table 4.4.

Table 4.4: Geometrical parameters of acrylic vessel and TPB layer necessary for activity calculation. Listed are the truncated version of values, only considering up to the 550 mm height considered in the control region.

Geometrical Parameter	Value
Surface Area of AV [TPB/Acrylic] [Fill Level]	$7.42 \pm 0.02 \text{ m}^2$
Volume of AV Bulk Up to $50 \mu\text{m}$ Depth [Fill Level]	$(3.06 \pm 0.01) \times 10^{-4} \text{ m}^3$
Mass of AV Bulk Up to $50 \mu\text{m}$ Depth [Fill Level]	$(3.49 \pm 0.01) \times 10^{-1} \text{ kg}$

## Result

All of these calculated parameters are combined together using Equation 4.1 to get a final activity estimate for the different surface alpha components. Each value and the final result are displayed in Table 4.5.

Table 4.5: Values determined in previous sections, and the resulting Activity for each component using Equation 4.1. Note that a livetime of 376 days is used.

Surface Alpha Activity Calculation Table				
Sample	$N_{CR}^u$	Area/Volume $S^u$	CR Efficiency, $\epsilon^u$	Activity, $A^u$
AV Surface	9,423	$7.42 \pm 0.02 \text{ m}^2$	$43.47 \pm 0.27\%$	$0.090 \pm 0.006 \text{ mBq/m}^2$
AV Bulk	8,821	$(3.49 \pm 0.01) \cdot 10^{-1} \text{ kg}$	$10.80 \pm 0.12\%$	$7.211 \pm 0.162 \text{ mBq/kg}$ , Full: $3.678 \pm 0.056 \text{ mBq}$
TPB Bulk	4,636	$7.42 \pm 0.02 \text{ m}^2$	$46.03 \pm 0.29\%$	$0.042 \pm 0.007 \text{ mBq/m}^2$
TPB Surface	9,602	$7.42 \pm 0.02 \text{ m}^2$	$47.94 \pm 0.27\%$	$0.083 \pm 0.008 \text{ mBq/m}^2$

These activities can also be translated to a total surface alpha trigger rate. By taking the ratio of triggers in the detector to total alpha decays (Hz/Bq) and applying

it to the activity, an estimate of the trigger rate of each component can be made. This ratio is extracted from the simulated samples, and the results are presented in Table 4.6.

Sample	Trigger Prob. (Hz/Bq)	Trigger Rate ( $\mu\text{Hz}$ )
AV Bulk	$0.178 \pm 0.001$	$448 \pm 10$
AV Surface	$0.519 \pm 0.003$	$347 \pm 23$
TPB Bulk	$0.769 \pm 0.004$	$240 \pm 40$
TPB Surface	$0.999^{+0.001}_{-0.004}$	$615 \pm 59$
Total	$1650 \pm 76 \mu\text{Hz}$	

Table 4.6: Surface alpha component trigger rate calculations. For each component, simulated samples were used to find the trigger probability (with statistical uncertainty). These values are applied to the total activity ( $A^u S^u$ ) for each component.

These activity estimates can be directly compared to the previous estimate from the 231 live day dataset [16]. In that paper, the surface alpha activity is quoted as a surface component, adding TPB Bulk, TPB Surface and AV Surface, and a bulk component, considering just the AV Bulk. In this thesis' work, the surface activity estimate comes to  $0.22 \pm 0.02 \text{ mBq/m}^2$ , compared to the previous 231 live day estimate of  $0.26 \pm 0.02 \text{ mBq/m}^2$ . The two are within each other's uncertainty. As for the  $50 \mu\text{m}$  of acrylic bulk activity, this thesis' estimate of  $3.68 \pm 0.06 \text{ mBq}$  is compared to the previous estimate of  $2.82 \pm 0.05 \text{ mBq}$ . This is a sizeable difference. In the previous estimates, a  $^{222}\text{Rn}$  component was part of the fit to account for the leakage in uncorrected data, seen in Figure 4.2. It is possible some high energy  $^{210}\text{Po}$  alphas in the previous study were being mislabelled as  $^{222}\text{Rn}$  alphas due to some very strong clipping effects. Regardless, the control region defined in this study is the purest yet, and gives confidence to this result. There are also added systematic uncertainties not taken into account for this study that could influence the agreement between the two estimates, including the treatment of alpha quenching, documented in Appendix A. Uncertainties in the acrylic vessel geometry taken into account in this study were not considered in the previous, causing the increase in activity uncertainty.

The activity calculation can be validated by directly comparing with data in event selections where we expect there to only be surface alpha events. By normalizing the simulated surface alpha samples, and scaling them by the livetime of the dataset and the calculated trigger rate, an estimate of the events in the detector can be made. Plotting this estimate in these surface alpha validation regions shows great agreement between simulation and data. An example of one of these regions is shown in Figure 4.5. This region is defined by an intermediate PE range (10-15k PE) and reconstructed radius higher than 700 mm. Great agreement gives confidence to the trigger rate and activity estimates.

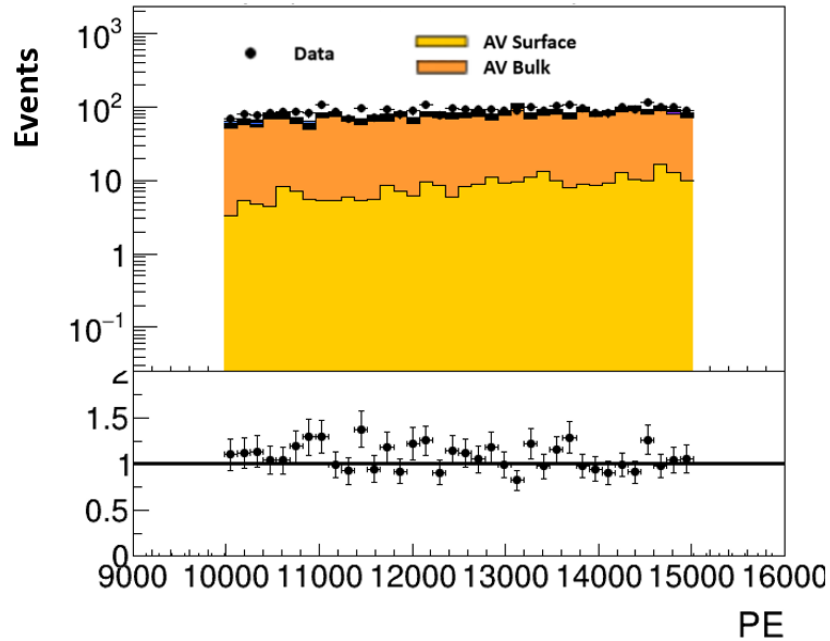


Figure 4.5: Validation of the surface alpha trigger rate estimate in a surface alpha dominant region. The region is defined by an intermediate PE range (10-15k PE) and higher reconstructed radius ( $R > 700$  mm). Surface alpha simulations (yellow/orange) are scaled by the trigger rates in Table 4.6 to match the dataset (black).

## 4.2 Surface Alpha Positional Leakage

The calculated activity results in a significant surface alpha background that can leak into the dark matter search region and affect the sensitivity of the detector. A handle against these events is necessary. By definition, these alphas originate at the edge of the liquid argon bulk, and can not travel far into the scintillation material before depositing their energy. Removing any events that occur at or near the acrylic surface will eliminate this background.

The PE-based position reconstruction algorithm introduced in Section 2.2 ("MB-Likelihood") is used to determine the location of events within the detector based on the distribution of PE in the PMTs. The surface alpha simulated samples are plotted against this reconstructed radius in Figure 4.6. As expected, the vast majority of these events reconstruct appropriately, close to the edge of the detector.

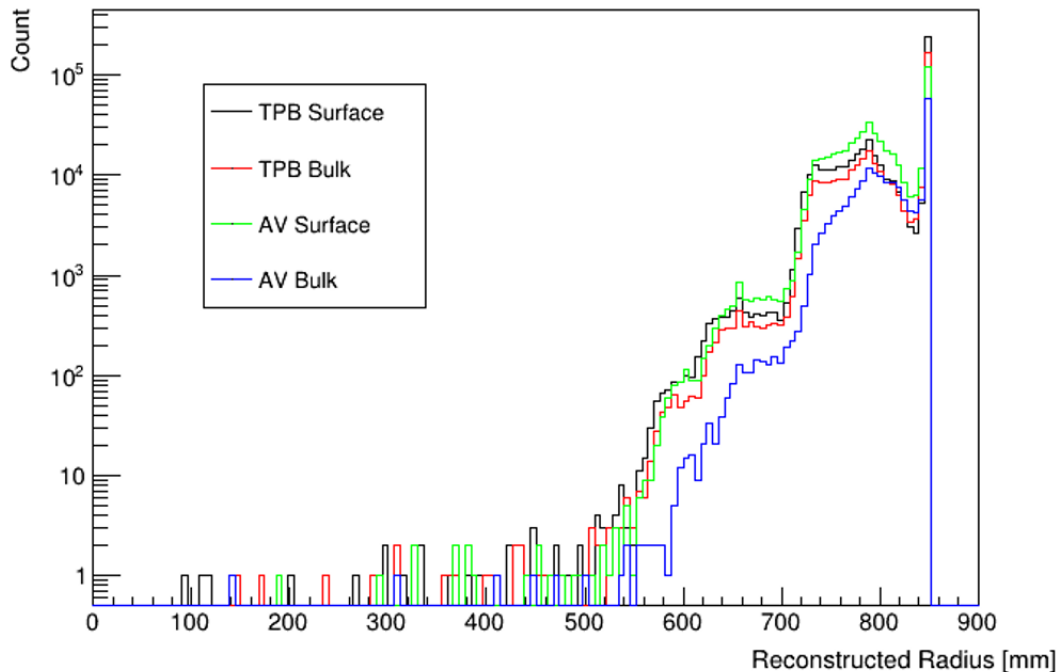


Figure 4.6: Reconstructed radius [mm] of  $^{210}\text{Po}$  surface alpha simulations, with a log scale on y-axis.

Restricting the dark matter search to events within a certain radial cut would

remove a large amount of these events. However, there is still a population of events reconstructing deeper into the detector volume.

### 4.2.1 Pentagonal Alphas

To further reduce this surface alpha background leakage, a deeper understanding of these low radius alpha events is necessary. Specifically, an understanding of why the position reconstruction algorithm is failing for a small portion of surface alpha events. To do this, we can look at the angular distribution of the origin of these events, in  $\cos \theta$  and  $\phi$ . In this plane, we can flatten and view the layout of the spherical detector. The PMT distribution is clear, displayed in Figure 4.7 with black labels. Each PMT is labelled 0-254. Due to the spherical shape of the detector and the circular shape of the PMTs, it is impossible to get complete PMT coverage of the vessel. Eleven pentagonal shaped gaps in PMT coverage, labelled in red in Figure 4.7, exist along the detector. Five are located at  $\cos \theta = 0.4$ , five at  $\cos \theta = -0.4$ , and one at the bottom of the detector.

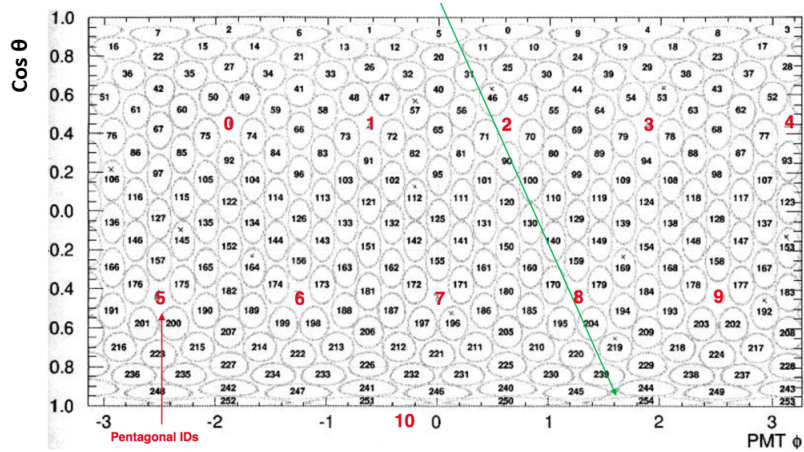


Figure 4.7: PMT map in  $\cos \theta$  and  $\phi$ . PMTs are labelled in black. Eleven pentagonal gaps in PMT coverage are labelled in red. Figure courtesy of Robert Stainforth, DEAP Collaboration.

Using simulated samples, the simulated X, Y, and Z position of the event can be

compared with the reconstructed position. The angular distribution can be calculated and plotted with:

$$\phi = \arctan\left(\frac{Y}{X}\right) \quad (4.10)$$

$$\cos \theta = \frac{Z}{\sqrt{X^2 + Y^2 + Z^2}} \quad (4.11)$$

The TPB/LAr interface sample is used, with a preselection similar to Table 4.2. Since we are using a simulated surface alpha sample, we do not need to worry about eliminating other types of events. Instead, we can use an event selection closer to our dark matter search. The PE range is changed to  $80 < \text{PE} < 500$ . Two cuts are added, the "charge fraction" cuts. These cuts are defined as:

- PE in top two rings of PMTs less than 4% of total event PE
- PE in bottom three rings of PMTs less than 10% of total event PE

These cuts remove events that deposit a large fraction of their energy at the top or bottom of the detector. The top ring cut removes events in the gaseous argon region, while the bottom ring cut removes an excess of events seen in the low Z portion of the detector.

Applying these cuts to the sample, and plotting their angular distribution using the true position of the events, we can see the uniform distribution of the sample in Figure 4.8. The pentagonal gaps are indicated by squares. Also visible is the effect of the charge fraction rings, removing the gap at the bottom pole from the study.

This is repeated, looking only at events in the sample that reconstruct with a radius less than 800 mm. This distribution is shown in Figure 4.9. All events in the simulated samples that reconstruct within 720 mm originate from these pentagonal gaps. Within 800 mm, the leakage from pentagonal gaps is an order of magnitude larger than alphas originating from the rest of the acrylic surface.

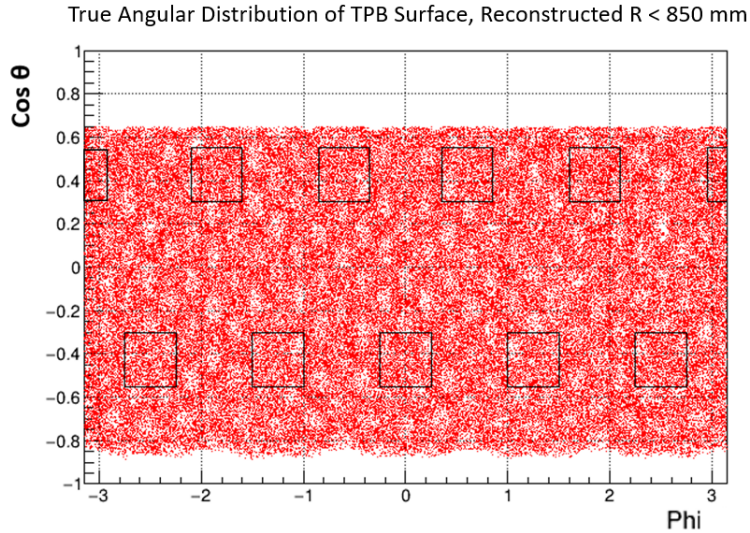


Figure 4.8: Angular distribution of simulated TPB/LAr interface events with very loose radial cut of reconstructed  $R < 850$  mm. Pentagonal gaps are marked by squares. High and low events are removed by reconstructed  $Z$  cut and charge fraction cuts.

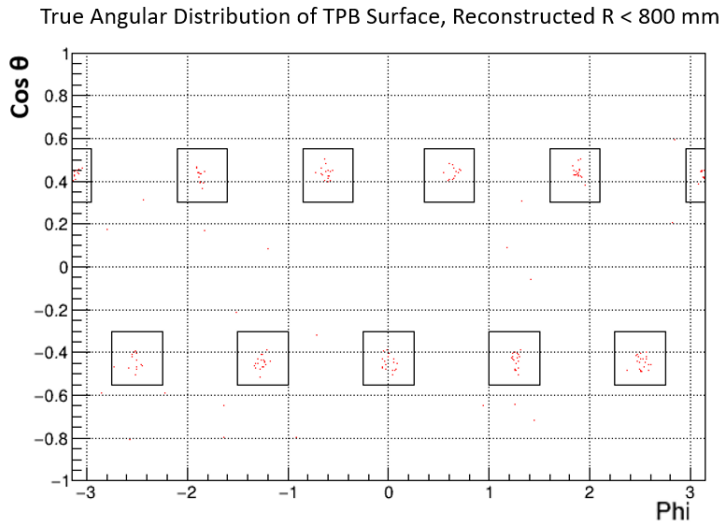


Figure 4.9: Angular distribution of simulated TPB/LAr interface events that reconstruct beneath 800 mm in radius. Pentagonal gaps are marked by squares.

Events originating from these pentagonal gaps are subject to poor position reconstruction. The lack of PMT coverage in these spots is causing lapses in the position reconstruction algorithm. It could be possible to define a conical event selection to remove these gaps. A cut defined as removing these regions could reduce the sur-

face alpha leakage to potentially zero. However, these events are plotted in the true position, a variable that can be tracked with simulated samples. In the case of real data, only the reconstructed positions are available. This means the effectiveness of a potential conical cut is dependent on these alphas reconstructing appropriately in  $\cos \theta$  and  $\phi$ . The reconstructed and true position of TPB/LAr interface events beneath 720 mm reconstructed radius are displayed in Figure 4.10.

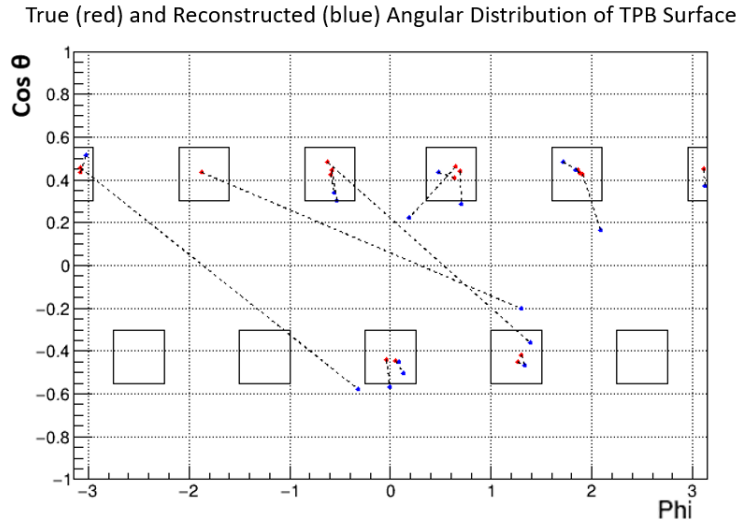


Figure 4.10: True and reconstructed angular distribution of simulated TPB/LAr interface events that reconstruct beneath 720 mm in radius. Pentagonal gaps are marked by squares. The true position is marked in red, with the reconstructed position of the event marked in blue, and connected by a dotted line.

While reconstruction is somewhat consistent, the position reconstruction algorithm moves the event further away from the pentagonal gap. In some cases, the event reconstructs wildly, moving the events to a completely different part of the vessel. The square gaps in these figures are already designed very conservatively. The effects of a cut on these gaps would be very costly to signal acceptance, removing large chunks of the effective volume in the dark matter search. A lack of consistency in the angular distribution reconstruction all but removes the potential for this cut.

This study was also done in a previous version of the simulation software. The position reconstruction algorithm did not undergo large changes between the two ver-

sions. Instead, the previous version operated with a different set of run conditions. In these conditions, some PMTs are disabled. These disabled PMTs create hexagonal gaps in coverage, and the resulting leakage past 800 mm is displayed in Figure 4.11. These PMT gaps create a very large amount of radial leakage. Their angular reconstruction (seen in Figure 4.12) is very poor as well, making the conical cut very ineffective.

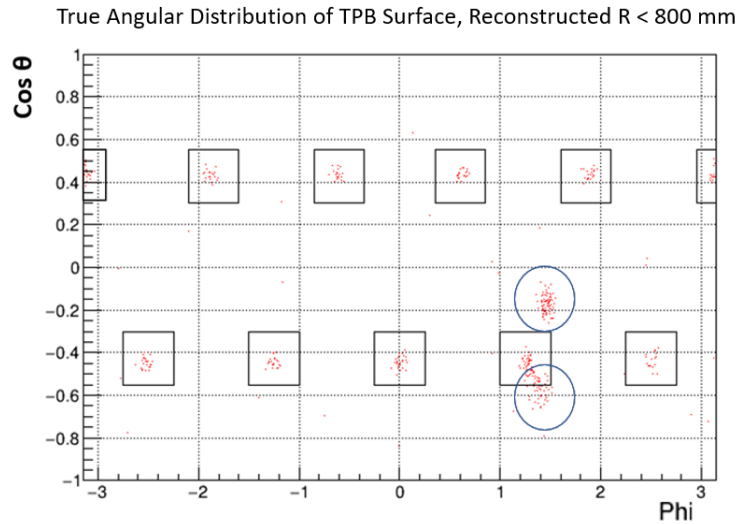


Figure 4.11: True angular distribution of surface alphas that reconstruct beneath 800 mm in radius, using simulated run conditions where some PMTs are disabled. Locations of disabled PMTs are indicated with blue circles.

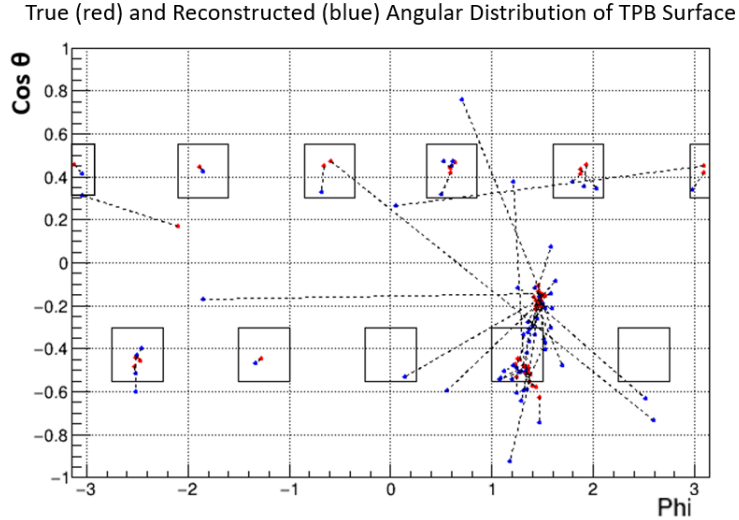


Figure 4.12: True and reconstructed angular distribution of simulated TPB/LAr interface events that reconstruct beneath 720 mm in radius. Pentagonal gaps are marked by squares. The true position is marked in red, with the reconstructed position of the event marked in blue, and connected by a dotted line.

## 4.2.2 Surface Leakage Measurement

An estimate of the surface leakage fraction for events in the dark matter PE region of 93-200 PE is performed. TPB/LAr interface samples are used to be conservative, as they have the largest leakage into lower radius (see Figure 4.6), and a low-level event selection is applied along with the dark matter PE region cut.

Nominal samples are generated for the TPB/LAr interface. Along with these, more samples are generated using the systematic variations for key simulation parameters. These different variations can impact the position of the alphas in  $F_{\text{prompt:PE}}$  space, and worsen position reconstruction. The same systematics are considered in all background studies based on simulated samples.

## Systematic Uncertainties

The RAT software uses a number of input parameters to generate event simulations. These input parameters include optical and geometric properties of the detector

that come from external measurements. Naturally, there is a level of uncertainty in these measurements that can impact the outcome of these event simulations. These parameter variations, or systematic uncertainties, must be accounted for in studies involving simulations. These systematics include:

- PMT After-pulsing:

After-pulsing is a source of noise in PMTs. This comes from the generation of pulses from the charge carriers of an initial pulse. The after-pulsing probability has been measured, with a  $\pm 15\%$  uncertainty on the value [46].

- Intermediate Liquid Argon Pulseshape:

The liquid argon pulseshape is determined by two exponentials, one for the singlet state and one for the triplet state. There is also a potential intermediate term attributed to electrons ejected during the initial interaction needing to random-walk back before being recombined [34]. The inclusion of this term is treated as a systematic variation.

- PMT Efficiency:

The PMTs have a quoted quantum efficiency, with an uncertainty of  $\pm 10\%$  on the value [28].

- PMT Efficiency Smear:

The PMTs have varying efficiencies from PMT to PMT. As such the actual PMTs have a spread in nominal efficiency, measured with a RMS of  $\pm 4.5\%$ . To account for this, a systematic is used where the  $\pm 4.5\%$  spread is applied randomly across the PMTs.

- Disabled PMT 204:

For a portion of the dataset, PMT 204 was disabled. To account for this, a systematic variation includes disabling this PMT in the simulation.

- TPB Scattering Length:

The intended thickness of the TPB layer is  $3 \mu\text{m}$  [30]. There is some indication that the actual layer is very uneven. An asymmetric uncertainty on the layer was estimated to be  $3_{-1.5}^{+3} \mu\text{m}$ . These variations are another systematic uncertainty.

- TPB Light Yield:

The light yield of TPB is quoted as 882 photons/MeV, with a  $\pm 10\%$  uncertainty on the value [47].

- LAr Refractive Index (and optical parameters):

The refractive index of liquid argon has been measured in different experiments [48, 49], with a small range of values taken as the systematic uncertainty. This variation also uses the relationship between the refractive index and other optical parameters of LAr (scattering length, group velocity of light) to account for the variation in these other parameters.

To combine these variations into one systematic uncertainty on a value, they must be combined properly.

Systematic uncertainties can be designated as either a single variation (i.e. Disabled PMT, Intermediate Pulseshape) or a paired variation (i.e. After-pulsing up and down, PMT efficiency up and down). How these uncertainties are combined is dependant on this categorization, and results in an asymmetric final systematic uncertainty.

In the case of a single variation ( $\sigma_i$ ), the absolute uncertainty is added in quadrature depending on its sign:

$$\sigma_{\text{total}}^+ = \sqrt{\sum_{i=1}^n (\max(\sigma_i - \sigma_0, 0))^2} \quad (4.12)$$

$$\sigma_{\text{total}}^- = \sqrt{\sum_{i=1}^n (\max(\sigma_0 - \sigma_i, 0))^2} \quad (4.13)$$

Where  $\sigma_{\text{total}}^{+/-}$  is the total uncertainty. In the case of a paired variation ( $\sigma_i^{+/-}$ ), the following method is used to determine the impact of the uncertainty:

$$\sigma_{\text{total}}^+ = \sqrt{\sum_{i=1}^n (\max(\sigma_i^+ - \sigma_0, \sigma_i^- - \sigma_0, 0))^2} \quad (4.14)$$

$$\sigma_{\text{total}}^- = \sqrt{\sum_{i=1}^n (\max(\sigma_0 - \sigma_i^+, \sigma_0 - \sigma_i^-, 0))^2} \quad (4.15)$$

Where the greater impact between the two variations is added to the total uncertainty in quadrature, unless the two variations point in different directions.

These two total uncertainties are combined to get a complete asymmetric systematic uncertainty.

## Results

The resulting surface leakage fraction is plotted as a function of contained mass in Figure 4.13. The nominal leakage is defined by the red curve, with the combined asymmetrical systematic uncertainty indicated by the grey band.

At our current fiducial radius of 630 mm (corresponding to 1248 kg contained mass), a surface leakage of:

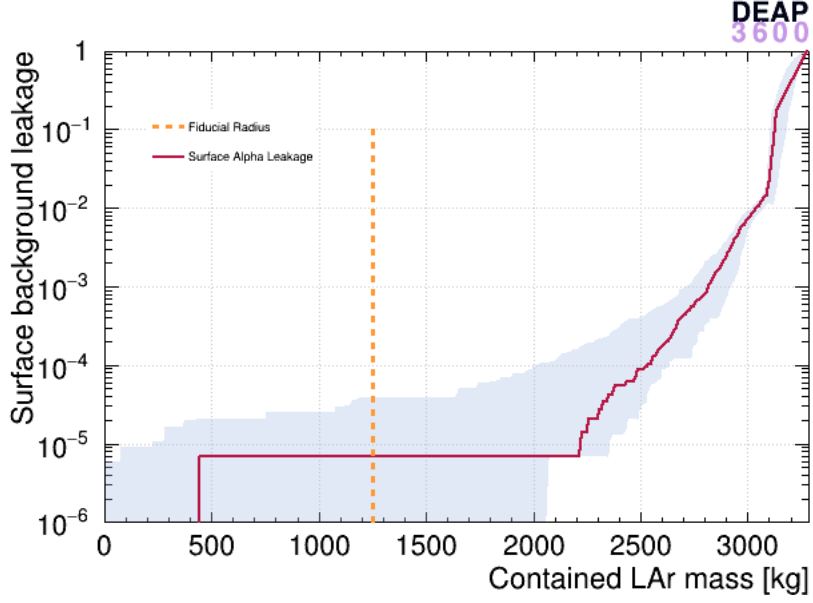


Figure 4.13: TPB/LAr interface alpha leakage as a function of contained LAr mass. Nominal curve is in red, with systematic uncertainty band in grey. Current radial cut of 630 mm (corresponding to 1248 kg contained mass) indicated with yellow line.

$$LF_{rad,630mm} = (0.689^{+2.53}_{-0.689}) \times 10^{-5} \quad (4.16)$$

is found. Expanding to a 90% confidence limit gives:

$$LF_{630mm,90\%} = 3.97 \times 10^{-5} \quad (4.17)$$

This reduction to a leakage fraction of 0.004% makes the surface alpha background nearly negligible in the dark matter search. A radius of 630 mm was chosen to reduce both surface alpha and neutron backgrounds, while still remaining sensitive to dark matter. The leakage curve remains flat up to 2000 kg, corresponding to a radius of roughly 720 mm, with a factor of 3 increase in the systematic band. This radial cut is revisited in Chapter 6, considering values between 630 mm and 720 mm, the region

where surface alphas remain negligible. For reference, the 90% confidence limit of surface leakage at 720 mm comes out to:

$$LF_{rad,720mm} = (0.689^{+6.45}_{-0.689}) \times 10^{-5} \quad (4.18)$$

$$LF_{720mm,90\%} = 8.94 \times 10^{-5} \quad (4.19)$$

The potential conical cut based around eliminating events originating from the pentagonal gaps is not yet required. The reduction in surface alpha events from a radial cut constrains the background effectively. Losses in signal acceptance from the cut would greatly outweigh the effect on the background.

In future studies, if the surface alpha background requires reduction, the conical cut can be revisited. More work will have to be done in position reconstruction such that angular reconstruction is consistent. As it stands, the position fitter MBLikelihood is strong enough to mitigate this background.

# Chapter 5

## $\alpha$ -Decays from the Neck Flowguide

Introduced in Chapter 3, another major source of attenuated alphas are the long-lived  $^{210}\text{Po}$   $\alpha$ -decays occurring at the acrylic neck flowguide surface. Alphas originating from this specific source will be referred to as "neck alphas" within this paper. Neck alphas are a challenging background due to the intricacy of the neck geometry. The acrylic neck flowguide has two parts, the inner flowguide and the outer flowguide. On these flowguides are three surfaces that we consider for our alpha sources: the inner flowguide inner surface (IFIS), the inner flowguide outer surface (IFOS) and the outer flowguide inner surface (OFIS). This composition can be seen in Figure 5.1, where these three surfaces are highlighted.

Alpha decays occurring at these surfaces are subject to shadowing from the other acrylic surfaces. Scintillation light produced by the decay can be absorbed by acrylic flowguide components (Figure 5.1), which are not coated in TPB. This causes a reduced number of photoelectrons from reaching actual PMTs, and consequentially, a much lower reconstructed energy than the alpha began with. This degraded energy can cause these alpha events to leak into the dark matter search region of interest. As opposed to the previously discussed surface alphas, which originate from the inner surface of the AV and reconstruct there, these neck alphas tend to reconstruct in the

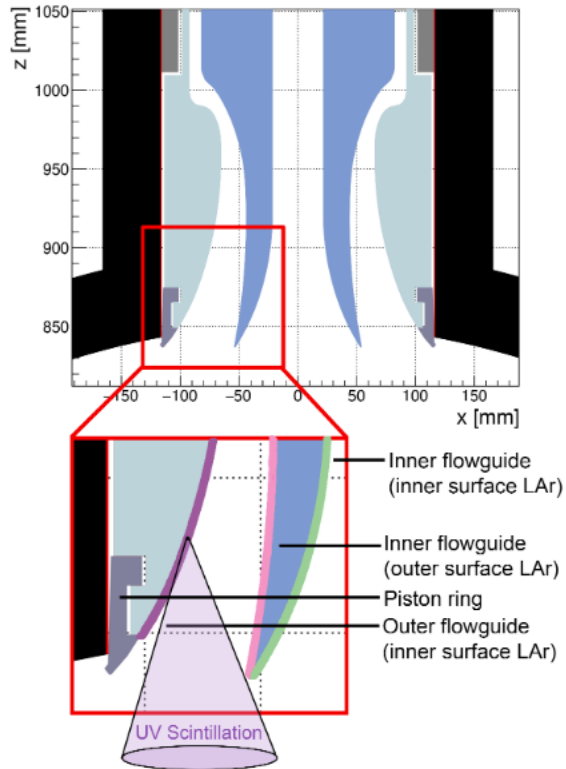


Figure 5.1: Cross-sectional illustration of the flowguide components in the AV neck. Shown are the three FG surfaces: inner flowguide inner surface (IFIS) in green, inner flowguide outer surface (IFOS) in pink, outer flowguide inner surface (OFIS) in purple and the piston ring in grey [16].

centre of the detector, and therefore cannot be eliminated by fiducial positional cuts. As such, these events become a very large portion of the background model in the dark matter search.

## 5.1 Control Regions and Fit

Scintillation light originating from the neck is observed, with  $F_{\text{prompt}}$  consistent with 5.3 MeV  $\alpha$  predictions, suggesting  $^{210}\text{Po}$  decays [16]. Monte Carlo simulations of these alpha decays are generated for all three surfaces. In these simulations, a liquid argon film of  $50 \mu\text{m}$  is layered on the flowguide surfaces such that scintillation light can be produced by the alpha. The acrylic neck is located in the gaseous argon top of the

detector (above 550 mm height), so a LAr volume is necessary to produce the proper scintillation light. A thickness of 50  $\mu\text{m}$  is chosen so that the alpha could come to a stop within the LAr. Analysis of these samples shows distinct reconstructed position distributions separating the three components, seen in Figure 5.2, after a neck alpha preselection defined in Table 5.1. These features are seen in PE:Reconstructed Z space, caused by the shadowing of scintillation light creating very location dependent distributions.

Table 5.1: Definition of neck alpha preselection.

<b>Event Selection</b>	<b>Purpose</b>
PE detected > 75	Low PE cut to stay above trigger threshold
Fprompt>0.55	High prompt window timing cut to remove electronic recoils, select only neutron recoils (See Figure 2.6)
Cut in Fprompt:PE space mirroring lower bound of ROI	Removes $^{39}\text{Ar}$ beta decays
Single-scatter event	Pileup cut removing coincidence events
Fraction of PE in one PMT < 3.5%	Removing events with more than 3.5% of light in one PMT, arm distributions present in this region
Reconstructed Z < 700 mm	Ensure events are reconstructed below neck flowguides
Reconstructed R < 700 mm	Remove surface events with high reconstructed radius

These distributions are also present in the 376 liveday dataset, and can be used to generate control regions to constrain alpha decays from the three different components individually. This work was done to calculate the contribution of these alphas to the dark matter search in the 231 day livetime paper [16]. The work of this thesis involves the implementation of the dust alpha background into this model, and the optimization of the flowguide surface alpha control regions.

The initial control regions used to distinguish the different component contributions were defined in PE and reconstructed Z position. Improvements are made by expanding into reconstructed R, to distinguish the OFIS and IFIS distributions. Ten regions are defined to isolate the neck alpha components, and displayed in Table 5.2.

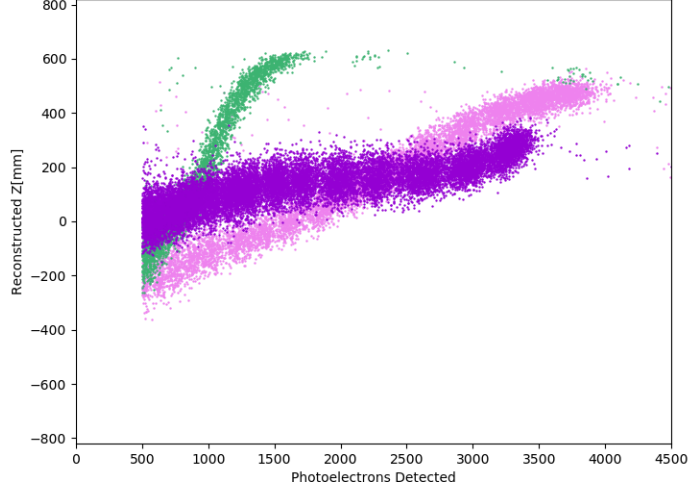


Figure 5.2: Positional neck features in Monte-Carlo samples after event selection in Table 5.1. IFOS is in green, OFIS is in purple, and IFIS is in pink.

Table 5.2: Definition of neck alpha control regions. This selection is applied on top of the preselection in Table 5.1. These regions are displayed graphically in Figures 5.3, 5.4.

Control Region	PE	Reconstructed Z [mm]	Reconstructed R [mm]
NCRA_IFOS	$300 < PE < 600$	$-500 < Z < -75$	$75 < R < 550$
NCRB_IFIS	$600 < PE < 1600$	$-275 < Z < -150$	$275 < R < 450$
NCRC_IFOS	$600 < PE < 1100$	$-75 < Z < 250$	$325 < R < 550$
NCRC_OFIS	$600 < PE < 1100$	$-150 < Z < 250$	$50 < R < 325$
NCRD_OFIS	$1100 < PE < 2400$	$-75 < Z < 250$	$75 < R < 300$
NCRD_IFIS	$1100 < PE < 2400$	$-75 < Z < 250$	$300 < R < 450$
NCRE_IFIS	$2400 < PE < 3450$	$50 < Z < 350$	$400 < R < 500$
NCRE_OFIS	$2400 < PE < 3450$	$50 < Z < 350$	$175 < R < 400$
NCRG_IFOS	$850 < PE < 1700$	$250 < Z < 650$	$425 < R < 700$
NCRH_IFIS	$3000 < PE < 3900$	$350 < Z < 550$	$425 < R < 580$

This redefinition of control regions results in a 8% decrease in the  $\chi^2/ndf$ . Attempts were made to expand the control regions into lower PE ranges, but poor separation between components in reconstructed Z made it too costly. These control regions are displayed in three dimensions in Figure 5.3 and two-dimensional projections in Figure 5.4.

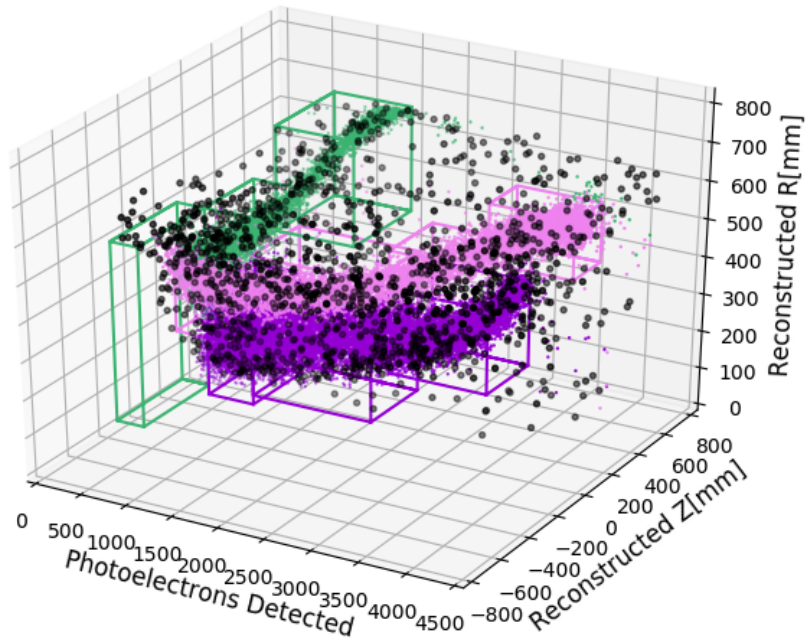


Figure 5.3: Three dimensional neck control regions displayed on top of simulation and data distributions. Data plotted in black, IFIS simulation in pink, IFOS in green, and OFIS in purple.

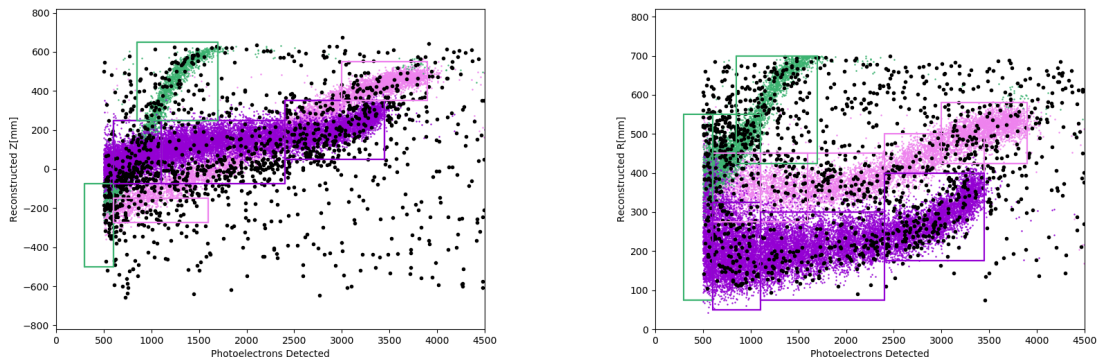


Figure 5.4: Left: PE vs Reconstructed Z [mm] for simulations (IFIS-Pink, IFOS-Green, OFIS-Purple) and data (black). Control regions are also plotted on top of distributions. Right: PE vs Reconstructed R [mm].

Along with these features present from neck decays, there is also a distinct background present throughout this neck alpha region. This is more distinct in Figure 5.4. Initially this background was treated as a flat contribution [16]. This flat background rate is constrained with nine square control regions between 5000 and 8000 PE. Following the development of the dust alpha background hypothesis, this was understood as the origin of the additional background in neck alpha control regions.

As mentioned in Chapter 3, a third source of attenuated alphas in the DEAP-3600 detector comes from  $^{210}\text{Po}$  alpha decays within dust particulates diffuse in the liquid argon bulk. These alphas deposit a fraction of their energy within the dust particle before entering the scintillation material, resulting in events with a wide range of PE counts. Because of this, the dust alpha background is present within the neck control regions, and for a more accurate fit to data, should be used as our background template in the fit.

Alpha decays within copper dust particulates are simulated for various diameter of dust particulate:  $1\mu\text{m}$ ,  $5\mu\text{m}$ ,  $10\mu\text{m}$ ,  $17\mu\text{m}$ , and  $25\mu\text{m}$ . This is done by uniformly distributing degraded alphas throughout the LAr bulk with energies and trajectories matching an alpha released within a dust particulate. Work done by Pushpa Adhikari involved fitting these to data in a wide PE range of 6000 - 23000 PE, resulting in a calculated trigger rate for the dust alpha background across the detector. This rate is listed in Table 6.1, with its impacts to the dark matter search further explored in Section 6.2.

These dust alpha decay simulations, scaled with the calculated rates, are plotted along with the neck simulations and 376 liveday dataset in Figure 5.5, where the dust model fits well with data.

A one dimensional template fit is employed, fitting the three simulated neck alpha samples and the dust background template to the three year dataset within the 18 control regions, 10 neck alpha regions and 8 dust alpha regions. For the dust alpha

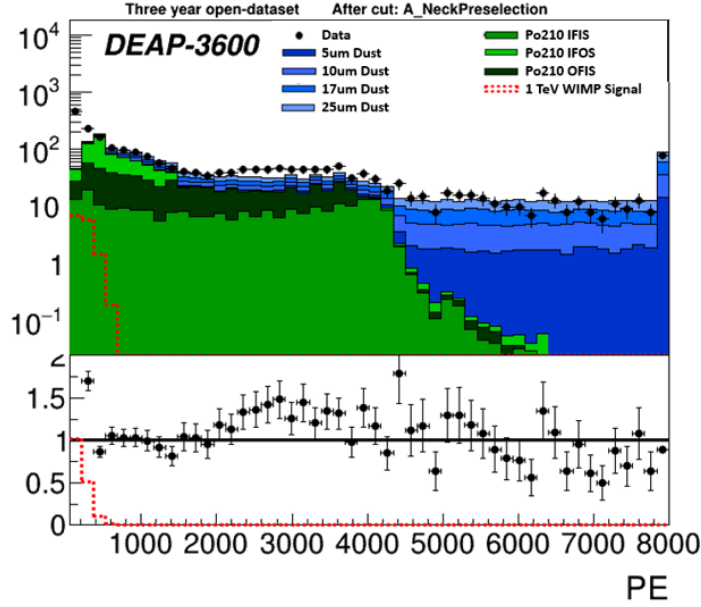


Figure 5.5: One dimensional stacked histogram of preselection defined in Table 5.1 over PE. Simulated neck alpha events are green, simulated dust alpha events are blue, and data is shown with black points. After 4500 PE, the region is dominated by dust alpha events, with some leakage into lower PE.

background, all five sizes of dust samples are used as one parameter, with the relative weights between them kept constant. This background template is scaled to fit the background control regions defined in the higher PE boxes. The piston ring contribution, previously included in the fit, is ignored, as the contribution is extremely small compared to the other neck components [16]. The different regions and the sample distributions within them are mapped along a PE axis, and a one dimensional fit is performed simultaneously across all the control regions. This fit optimizes the normalization of each sample to best fit the data across the mapped axis.

The results of this fit can be seen in Figure 5.6, where the PE-mapped control regions are displayed, along with the fit samples and data.

The scale factors of the neck flowguide components listed in Figure 5.6 are also the trigger rate for that alpha source. The trigger rate is defined as the number of events this component is responsible for per second, and has units of Hz. It is found by taking the number of triggers in the simulated sample, normalizing it to the run time

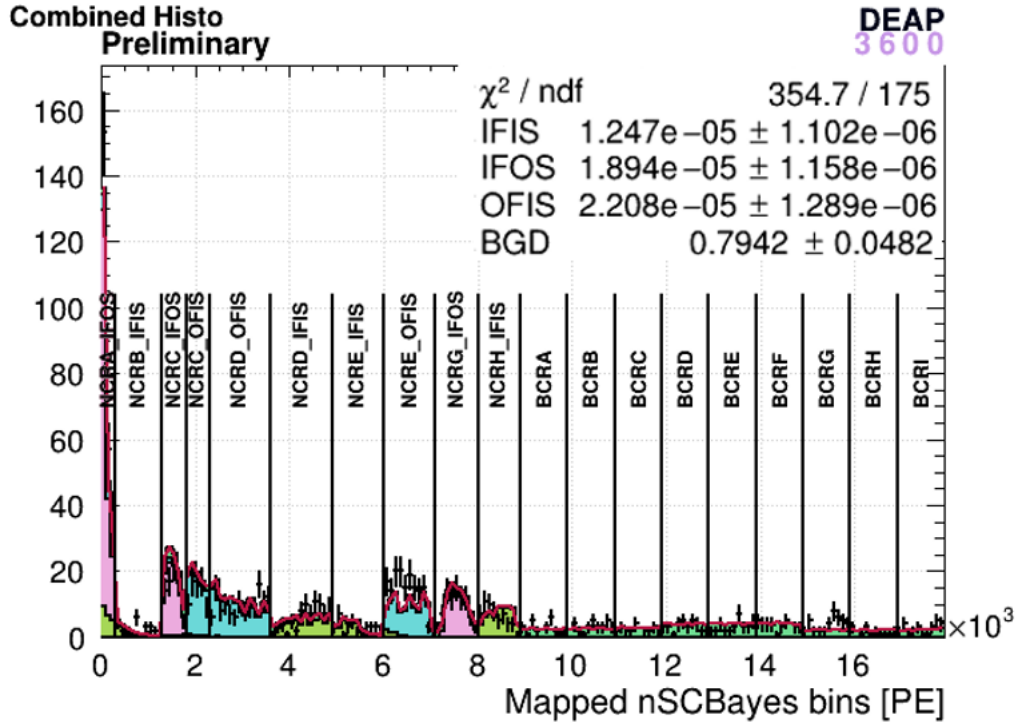


Figure 5.6: Results of neck alpha template fit, using the control regions outlined in Table 5.2 along with the background control regions (BCRX). Every CR, and the events within it, is projected onto and chained along the PE x-axis. Note, the distances on the mapped axis are preserved, but the absolute values do not have physical meaning. IFOS is in pink, IFIS is in green, and OFIS is in blue. Also included is the resulting scale factors for each sample and the fit statistic. Dust is labelled by "BGD". In the case of this scale factor, this value is applied to the dust alpha fit result, and is unitless.

of the dataset, and dividing by the run time in seconds. This rate can be multiplied by any livetime to get the number of triggers measured by the detector over that time. The dust scaling factor (BGD) is scaled with respect to the dust alpha fit result. The best fit is achieved when reducing the dust alpha trigger rate to 79% of its current value.

These control regions can be unmapped, and the different samples can be stacked for better comparison to data. This stacked histogram version of the fit can be seen in Figure 5.7. The inclusion of this background template allows for better agreement in the low PE regions of our neck preselection, where the dust template is larger than

the previous flat background.

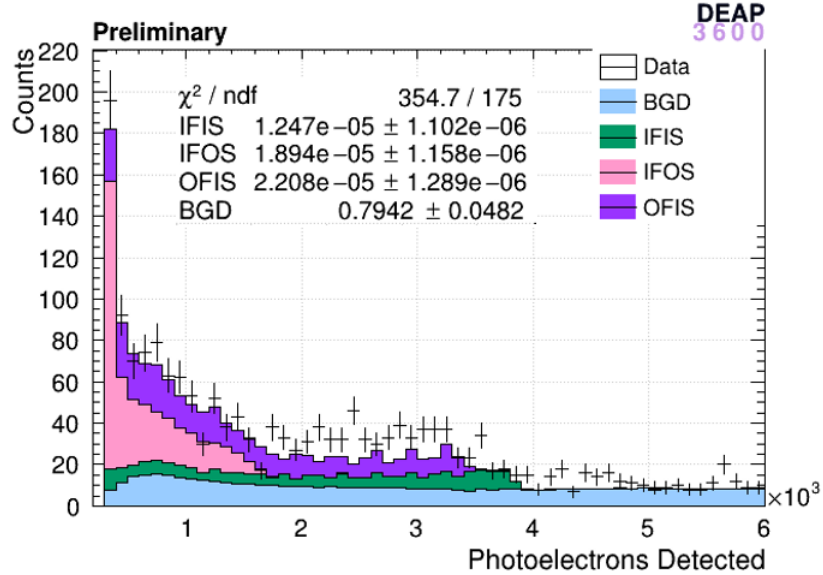


Figure 5.7: Results of the neck template fit. Data plotted here against stacked and scaled neck and dust simulations. Also included is the fit statistic, scaling factors for each neck component, and the scale applied to the dust template for the fit, with fit uncertainties.

These final rates are left as trigger rates, and not converted to an activity. This is due to uncertainty in the geometry of the liquid argon at the flowguide components. This includes the surface area of the film, its thickness, and the potential for the film to actually be a liquid argon mist. The mist hypothesis is actively being worked on, and will be compared to data when complete. Instead, the rate is kept as a trigger rate, which can be used to calculate estimates for the dark matter search.

## 5.2 Systematics on the Neck Alpha Trigger Rate

Systematic uncertainties in different optical and physical parameters are considered, namely those in Section 4.2.2. To account for the uncertainty in our liquid argon layer, the reduced thickness of the layer at  $25 \mu\text{m}$  is considered as a systematic uncertainty as well.

New sets of Monte Carlo simulations for each systematic variation are generated individually, for both dust and neck alphas. With these, the fitting process is repeated to observe the impact of this uncertainty. These variations to the trigger rates are combined to calculate a final systematic uncertainty on the nominal rate. It is important to note that this process does not account for potential shape changes caused by the systematic variation. These changes may impact the extrapolation into the dark matter search region of interest. Because of this, we plot  $F_{\text{prompt}}$  and PE into the dark matter PE range to check for agreement between nominal and systematic samples. Comparisons for the PE variable up to 5000 PE and the  $F_{\text{prompt}}$  variable are displayed in Figure 5.9 and Figure 5.10. The 25  $\mu\text{m}$  LAr layer systematic dominates in the calculation, and is focused on in these figures. This systematic doubles the trigger rate of the neck alpha components in the fit.

This doubling is due to gaseous argon scintillation. The 50  $\mu\text{m}$  nominal LAr layer thickness was chosen so that an alpha generated at the neck flowguide surface would deposit all of its energy into the liquid argon. By reducing the layer thickness, there is the potential for an alpha to escape the liquid argon layer, and enter the gaseous argon region. The scintillation light created in gaseous argon alters the  $F_{\text{prompt}}$  distribution of the event. This can be seen in Figure 5.8, where the 25  $\mu\text{m}$  layer systematic has a large population of events with  $F_{\text{prompt}} = 0.3$ . Only the alphas with the longest tracks in liquid argon deposit all of their energy, and end up with a  $F_{\text{prompt}}$  in the nuclear recoil band. As a result, a higher number of alphas is required to match data in the NR band control regions. While this does increase the trigger rate, this does not necessarily increase the yield in the dark matter search region of interest, as the number of alphas with a  $F_{\text{prompt}}$  in the dark matter search region will still be similar to nominal. The yield is explored further in Section 6.2.

The rates can be compared directly with the results from the 231 liveday dataset [16], which used two dimensional control regions and a flat background. This

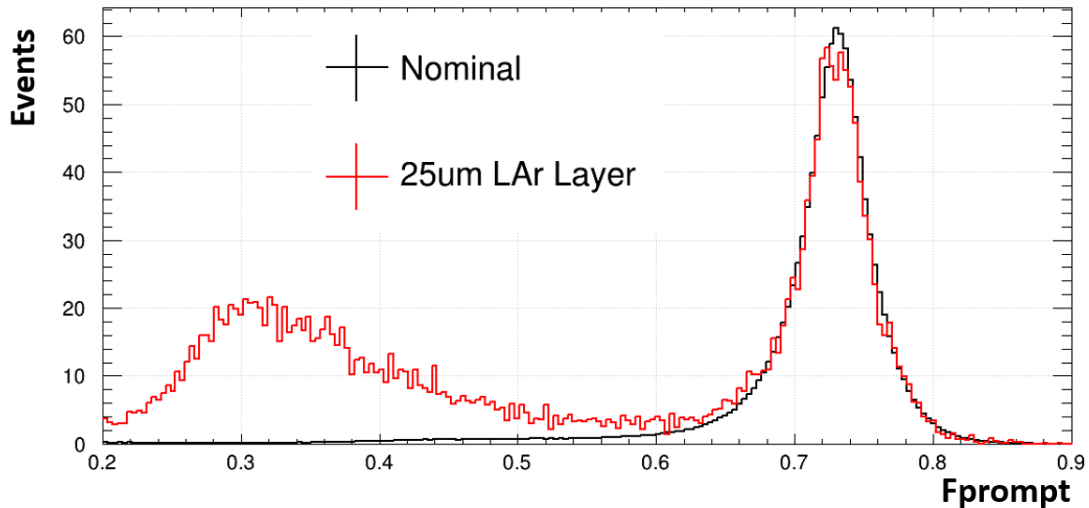


Figure 5.8: Fprompt distributions of 25  $\mu\text{m}$  LAr layer and nominal samples. For the 25  $\mu\text{m}$  LAr layer (red), a large population of events at low FPrompt is visible, coming from GAR scintillation due to the reduced layer thickness. This discrepancy is what causes the two fold increase in trigger rate. A loosened version of the neck alpha preselection in Table 5.1 applied, with the Fprompt cuts removed, for comparison.

study also did not include the 25  $\mu\text{m}$  LAr layer systematic, which is the dominant contribution to the current estimate uncertainty. This is shown in Table 5.3.

Table 5.3: Neck alpha trigger rate from fit, compared to 231 live day result. The previous estimate used two dimensional control regions, and a flat background component, instead of the 3D control regions and dust background template used in this work. The previous estimate also did not include the 25  $\mu\text{m}$  LAr Layer as a systematic. IFIS and IFOS components are redistributed, but summed rates are consistent.

Component	Previous Estimate ( $\mu\text{Hz}$ )	This Estimate ( $\mu\text{Hz}$ )
IFIS	$18.6 \pm 1.8$	$12.5^{+15.0}_{-0.3}$
IFOS	$15.0 \pm 1.2$	$18.9^{+16.8}_{-2.2}$
OFIS	$20.8 \pm 1.5$	$22.1^{+19.9}_{-4.0}$
Total	$54.4 \pm 2.6$	$53.5^{+30.0}_{-4.6}$

The updated version of the fit is similar, and within the previous study uncertainty for the OFIS component. The new fit adds more weight to the IFOS component, removing some weight from the IFIS component. The IFIS component and the dust

alpha template are both larger at lower PE, so the inclusion of the dust component causes a reduction in the IFIS weight. Likewise, the IFOS component is stronger at intermediate energies, where the dust template is lower than a potential flat template, and as such the IFOS sample needs to be scaled up in these new regions. The total sum of the three rates is in agreement with each other.

These trigger rates are combined with the 376 live day dataset in Chapter 6 to create an estimate of the neck alpha yield in the dark matter search. They are also used to optimize the dark matter event selection in this chapter.

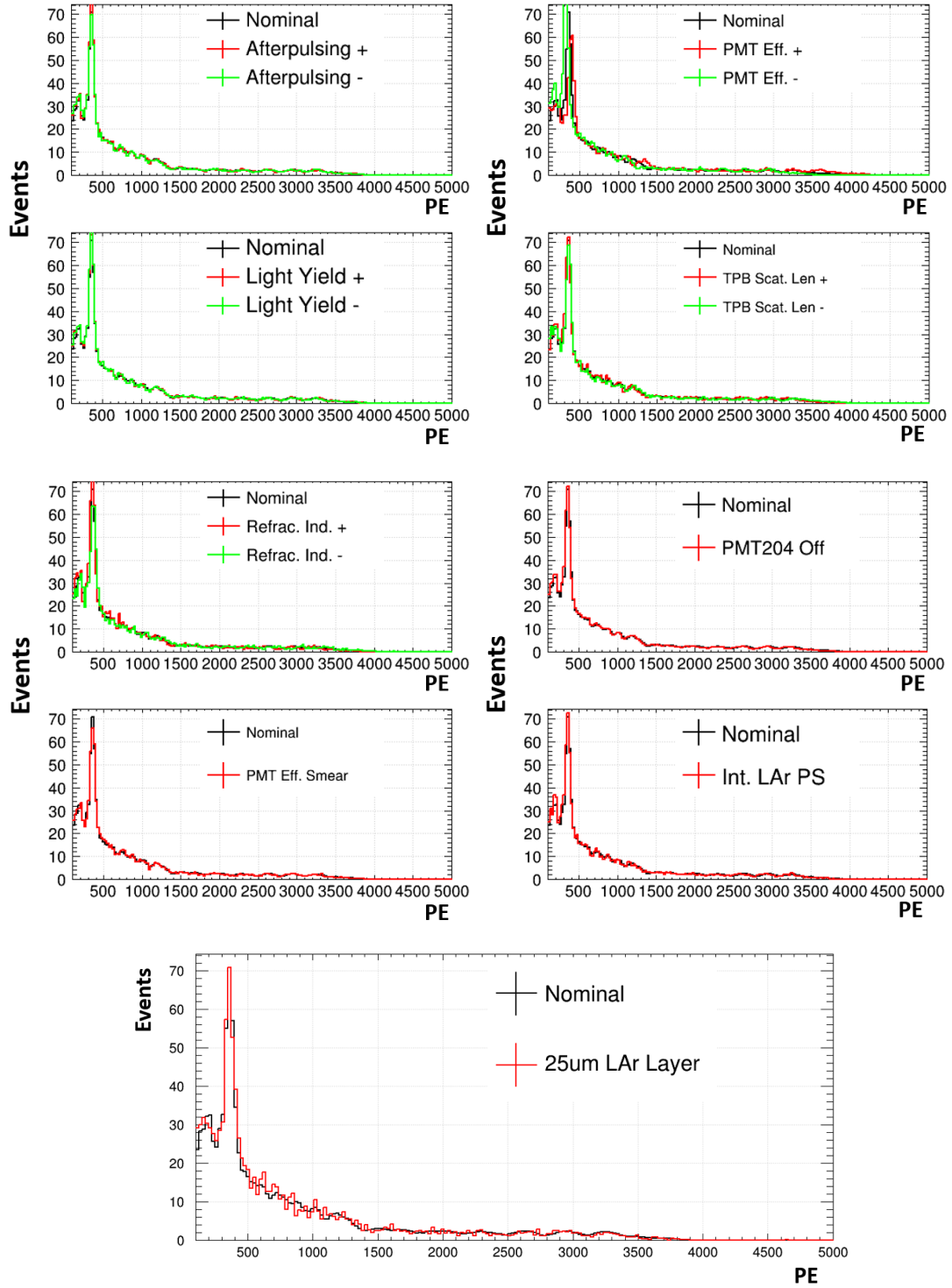


Figure 5.9: Comparison of nominal (black) to systematic variations (red/green) for PE, scaled to the expected number of triggers over the 376 live days for each systematic variation sample, with the dominant  $25 \mu\text{m}$  LAr Layer in the bottom row. A loosened version of neck alpha preselection in Table 5.1 applied for comparisons.

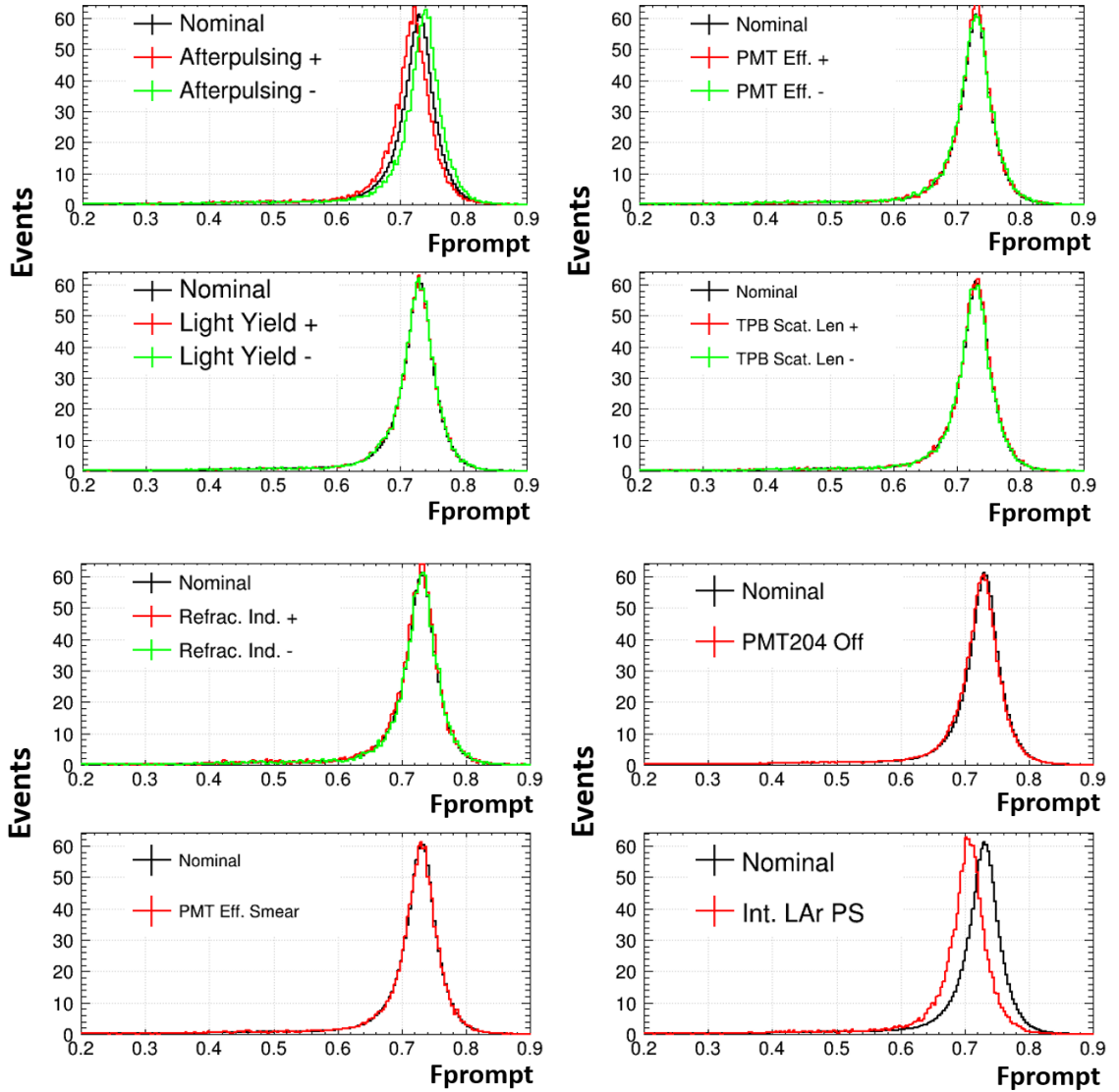


Figure 5.10: Comparison of nominal (black) to systematic variations (red/green) for  $F_{\text{prompt}}$ , scaled to the expected number of triggers over the 376 live days for each systematic variation sample, except for  $25 \mu\text{m}$  LAr layer systematic variation (see Figure 5.8). There is a noticeable difference in shape in the intermediate LAr pulse shape (bottom right plot), but that is expected, and accounted for in ROI estimate (Section 6.2).

# Chapter 6

## Impact on the Dark Matter Search

### 6.1 Event Selection Optimization

#### 6.1.1 Event Selection Definition

At this point two of the three major alpha backgrounds have been addressed, surface and neck alphas. Both  $^{210}\text{Po}$   $\alpha$ -decay sources were broken down into components for analysis. Simulated samples were generated for each of these components, and a fit was performed between the samples and data in designated control regions. Trigger rates were determined from these fits for each component, listed in Table 6.1. Also included are the dust alpha trigger rates found by Pushpa Adhikari, introduced in Chapter 5.

The rates in this table are the number of triggers registered by the detector from each source, per million seconds. They can be combined with a livetime to determine the number of events from these sources in a given dataset. The simulated samples can then be used to determine the efficiency of an event selection, and that efficiency can be applied to the number of events. In this way, the yield for any event selection and any amount of live days can be determined from these rates, provided enough statistics from the simulated samples exist. The alpha background yield for the dark

Table 6.1: Summary of trigger rates for all alpha sources, split between surface, neck and dust alphas. Uncertainties for the dust trigger rate is preliminary, as more systematics are still being considered.

$^{210}\text{Po}$ Alpha Decay Source	Trigger Rate ( $\mu\text{Hz}$ )
Surface, Acrylic Vessel Bulk	$448 \pm 10$
Surface, Acrylic Vessel Surface	$347 \pm 23$
Surface, TPB Bulk	$240 \pm 40$
Surface, TPB/LAr Interface	$615 \pm 59$
Neck, Inner Flowguide Inner Surface	$12.5^{+15.0}_{-0.3}$
Neck, Inner Flowguide Outer Surface	$18.9^{+16.8}_{-2.2}$
Neck, Outer Flowguide Inner Surface	$22.1^{+19.9}_{-4.0}$
Dust, 1 $\mu\text{m}$	$126^{+25}_{-32}$
Dust, 5 $\mu\text{m}$	$51^{+10}_{-13}$
Dust, 10 $\mu\text{m}$	$54^{+11}_{-13}$
Dust, 17 $\mu\text{m}$	$57^{+11}_{-14}$
Dust, 25 $\mu\text{m}$	$55^{+11}_{-14}$

matter search event selection, designed to maximize signal acceptance and minimize background, is calculated in Section 6.2 of this thesis. The previous event selection, used in [16], is described in Table 6.2.

The selection in Table 6.2 was chosen for the 231 live day dataset and must be reoptimized. For this previous analysis, neck alphas represented the dominant background in the WIMP search ROI. Some dedicated event selection cuts were defined with the intention of mitigating this background for the study.

Table 6.2: Dark matter event selection for 231 liveday study, separated into low-level cuts, positional cuts, and contour cuts, including the region of interest. The radial cut and contour cuts will be redefined during the reoptimization for the 376 liveday study.

<b>Low-Level Event Quality Cuts</b>	
Trigger condition and DAQ Calibration cuts	Data cleaning cuts that use the DTM to only select physics triggers
Single-scatter event and timing cuts	Cuts aimed at removing coincidence events and pileup using the relative timing of the event and shape of the waveform
Fraction of PE in one PMT < 40%	Cut on events with more than 40% of light in one PMT, removes Cherenkov
Neck Veto Activated	Remove any events that trigger the neck veto
Only first two pulses allowed in gaseous argon	One of the first 3 PMTs seeing light must be in LAr region, eliminates neck and GAr events
<b>Positional Cuts</b>	
Fraction of charge in top rings less < 4%	Remove events with high fraction of charge in top two rings
Fraction of charge in bottom rings < 10%	Remove events with high fraction of charge in bottom three rings
Reconstructed Z < 500 mm	Remove events above 550 mm, in gaseous argon
Reconstructed R < 630 mm	Remove events past 630 mm, mainly surface alphas and neutrons
<b>Dark Matter Study Contour Cuts</b>	
90% acceptance DeltaZ Contour	Z position reconstruction consistency cut, further explained in Figure 6.1, aimed at rejecting neck events
85% acceptance 3D dist. Contour	3D position reconstruction consistency cut, similar to DeltaZ, aimed at rejecting neck events
30% NR Acceptance Loss ROI	Region of interest contour in PE:Fprompt space, shown in Figure 2.5

One set of such cuts is the position reconstruction consistency cuts, listed in the Dark Matter Study Contour Cuts section of Table 6.2. There are two position reconstruction algorithms run on events: a charge based algorithm (MBLikelihood), and a time based algorithm (TimeFit2). Shadowing in the neck flowguide components causes a large amount of disagreement between these algorithms on the Z location and 3D vertices of events. Removing any events that have a large difference between the two algorithms can remove a large portion of neck events. The difference between the reconstructed Z position in MBLikelihood and TimeFit2 is shown in Figure 6.1, taken from the 231 live day paper [16]. The difference between the two ( $\Delta z$  in the x-axis) is much stronger for neck alpha simulations than for signal. The contour cuts based on this disagreement are in PE:Difference in Reconstructed Position space.

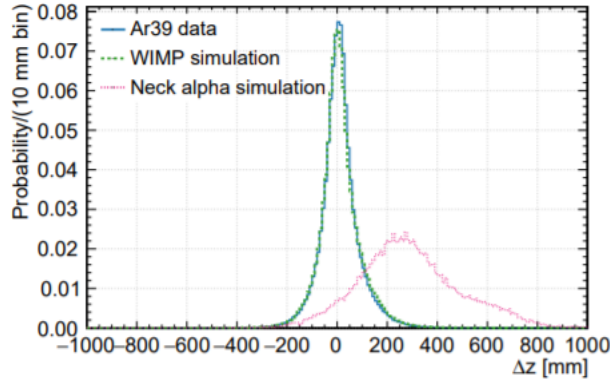


Figure 6.1: Difference in MBLikelihood and TimeFit2 position reconstruction algorithms for Z position, used to mitigate neck alpha events. Neck alpha simulations in pink are much higher in difference, and based around 250 mm. Signal events are based around 0 mm. Figure taken from 231 live day paper [16].

The other contour cut is the dark matter search region of interest, defined in PE:Fprompt space. This contour is defined to reject electronic recoil events with lower Fprompt (see Figure 2.6), and focus on the nuclear recoil Fprompt band. It is also defined in a very low PE range (93 - 200 PE), where the detector is most sensitive to dark matter events. The ROI definition from the 231 live day paper is displayed in Chapter 2 with Figure 2.5 [16]. The previous ROI definition causes a loss of 30%

in the nuclear recoil acceptance. The upper boundary of the ROI is defined to reject neck alpha events, which are defined by their higher  $F_{\text{prompt}}$  values.

The effects of these three cuts can be seen in Figures 6.2, 6.3, and 6.4, showing the Z and 3D position reconstruction consistency cuts, and the effect of the upper  $F_{\text{prompt}}$  bound of the ROI. In these plots, the distributions of the background and signal samples across the variables of interest are displayed, before and after the cuts are applied. In all three cuts, neck event rejection is very strong, however a sizeable amount of signal is removed.

These cuts were designed for the 231 live day analysis, and must be reoptimized for this new study. This is done by incorporating new machine learning techniques aimed at rejecting neck events. Adding these cuts to the event selection allows for the loosening of previous cuts defined to mitigate the neck alpha background. If the neck background is mitigated by machine learning estimators, the ROI can be expanded to higher prompt values of the nuclear recoil band, and the acceptance loss can be reduced. The position reconstruction consistency contours could also be loosened, removing less signal from the dark matter search. The event selection optimization analysis will look into loosening these cuts, along with the radial cut of 630 mm, by introducing a cut on one of the multivariate analysis (MVA) variables.

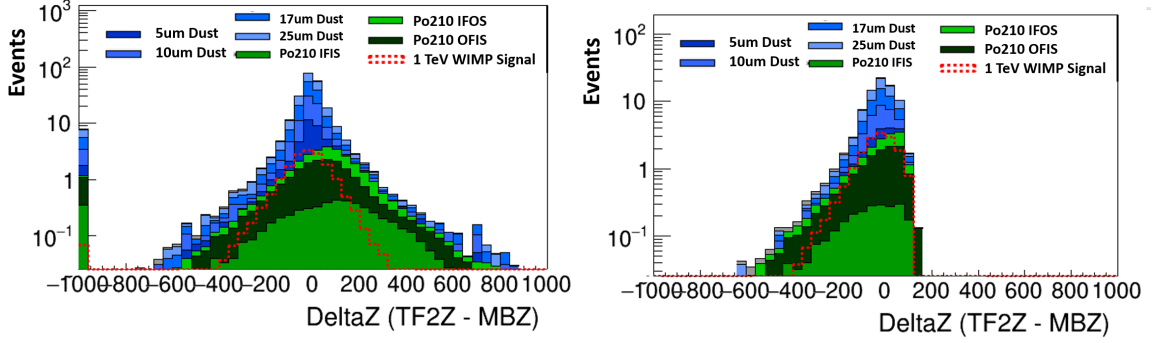


Figure 6.2: Impact of Z Position Consistency Cut. Dust alpha (blue) and neck alpha (green) simulations displayed in stacked histogram and plotted against  $1 \text{ TeV}/c^2$  WIMP at  $10^{-45} \text{ cm}^2$  cross-section signal (red). Plots shown for before (left) and after (right) the Z position consistency cut is applied in the event selection from Table 6.2. This cut is targeted at removing neck events, but also removes some signal and dust.

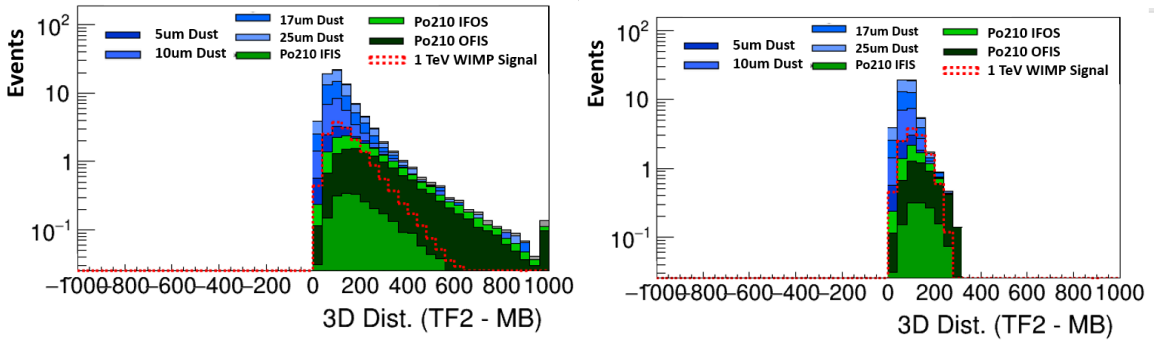


Figure 6.3: Impact of 3D Position Consistency Cut. Dust alpha (blue) and neck alpha (green) simulations displayed in stacked histogram and plotted against  $1 \text{ TeV}/c^2$  WIMP at  $10^{-45} \text{ cm}^2$  cross-section signal (red). Plots shown for before (left) and after (right) the 3D position consistency cut is applied in the event selection from Table 6.2. This cut is targeted at removing neck events, but also removes some signal and dust.

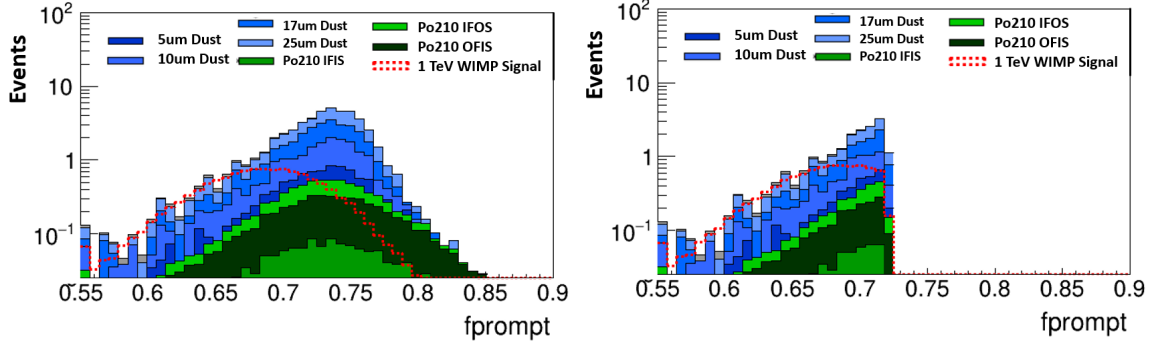


Figure 6.4: Impact of upper  $F_{\text{prompt}}$  contour of ROI (see Figure 2.5). Dust alpha (blue) and neck alpha (green) simulations displayed in stacked histogram and plotted against  $1 \text{ TeV}/c^2$  WIMP at  $10^{-45} \text{ cm}^2$  cross-section signal (red). Plots shown for before (left) and after (right) the upper  $F_{\text{prompt}}$  cut is applied, after the 3D position consistency cut in the event selection from Table 6.2. This cut is targeted at removing neck events, but also removes some signal and dust.

### 6.1.2 Introducing Multivariate Analysis

The surface alpha background is well mitigated with the radial cut (Figure 4.13), to the point where it is near negligible in the dark matter search. The dust alpha and neck alpha backgrounds are not as well constrained, and represent the dominant backgrounds in the dark matter search. Some handles were developed to limit neck alphas (discussed above), but are costly to signal acceptance, and limit the dark matter sensitivity of the experiment.

A great amount of work has been done by the DEAP Collaboration in creating machine learning techniques to discriminate against neck alphas efficiently in the dark matter search region [44]. Three different multivariate analysis (MVA) techniques were developed independently by different groups in the DEAP collaboration for this purpose:

- RF - Random Forest
- XGB - Gradient Boosted Decision Tree

- NN - Neural Network

Each estimator works on a preselection of events representing a superset of the dark matter search event selection defined in Table 6.2. The algorithms are trained on a set of simulated samples, with specific variables designated as potential features used to classify. These variables were validated, and chosen from a physics perspective. These include results from position reconstruction algorithms, and variables indicating events coming from the gaseous region of the detector. A brief overview of the different machine learning techniques is useful for comparisons.

A random forest classification algorithm uses the decision tree structure, but on a large, ensemble scale. Many individual uncorrelated trees, sampling randomly from the training set, and choosing from subsets of the feature list, work to classify events as either neck alphas or WIMP events. For each event to classify, each tree gives a classification vote, and the RF score is the proportion of all votes that is given to the signal hypothesis [50].

The XGBoost library is used to develop a gradient boosting algorithm. These algorithms use decision trees as well, but keeps them constrained (unlike Random Forest which allows for full tree growth). The target is to optimize accuracy through adding selectively chosen decision trees that minimize the loss function. The final classification comes as the weighted sum of these tree outputs [51].

The final algorithm used is a feed forward neural network. These algorithms employ layers of "neurons" or nodes. These nodes take in weighted inputs and apply an activation function to them, non-linearizing the output. Inputs are passed through the input layer, then through a varying amount of hidden layers where the activation functions are applied, before reaching the output layer. These multi-layer networks can learn the relationship between the input features and the target classification, and tune the weights during supervised learning on the training set for optimal sorting. The information will pass through these functions, and result in a set of classification

probabilities. The signal hypothesis probability is the neural network estimator [52].

For all scores, a value between 0 and 1 is attributed to each event. 0 is a neck-like event, and 1 is a signal-like event. These estimators are applied to different simulated samples, namely, the neck and dust alpha simulations mentioned in this thesis, and a sample of simulated neutron events. Surface alpha simulations are not used, as the MVA analysis preselection includes a cut on the reconstructed radius of 720 mm. This cut combined with a tight PE and Fprompt selection leaves no events in the surface alpha samples for analysis. The neck alpha, dust alpha and signal distributions are plotted for RF, XGB and NN in Figures 6.5, 6.6, and 6.7 respectively. These distributions include the low-level event quality cuts, and positional cuts from Table 6.2.

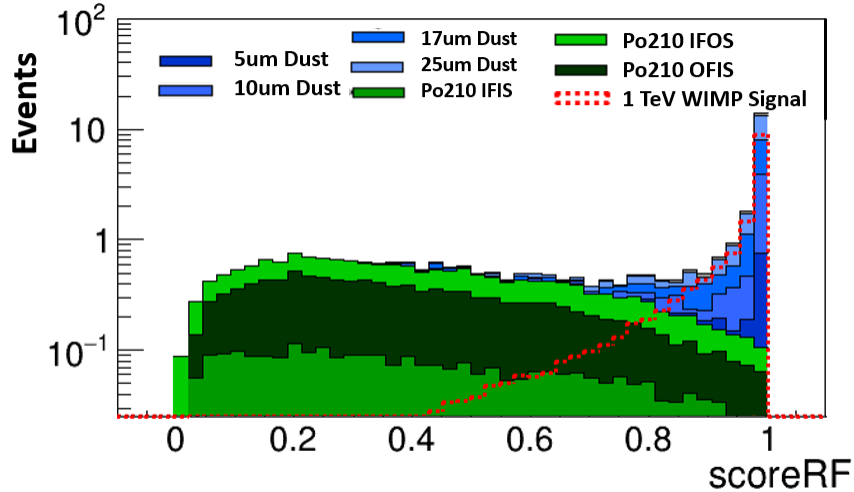


Figure 6.5: Random Forest Estimator distribution for simulated background and signal samples after low-level event quality cuts, and positional cuts from Table 6.2. Background simulations are stacked, with dust alpha events plotted in blue, and neck alpha events in green. Dashed line shows simulated 1 TeV/ $c^2$  WIMP at  $10^{-45}$  cm<sup>2</sup> cross-section signal distribution.

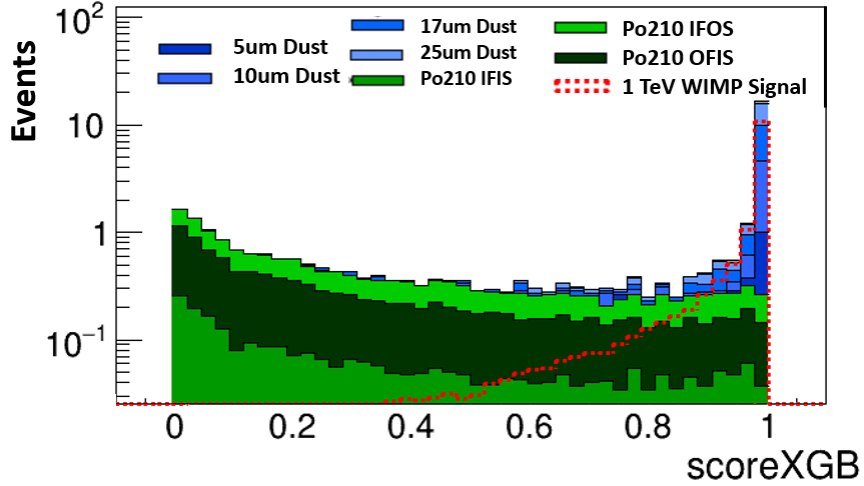


Figure 6.6: Boosted Decision Tree Estimator distribution for simulated background and signal samples after low-level event quality cuts, and positional cuts from Table 6.2. Background simulations are stacked, with dust alpha events plotted in blue, and neck alpha events in green. Dashed line shows simulated 1 TeV/ $c^2$  WIMP at  $10^{-45}$   $\text{cm}^2$  cross-section signal distribution.

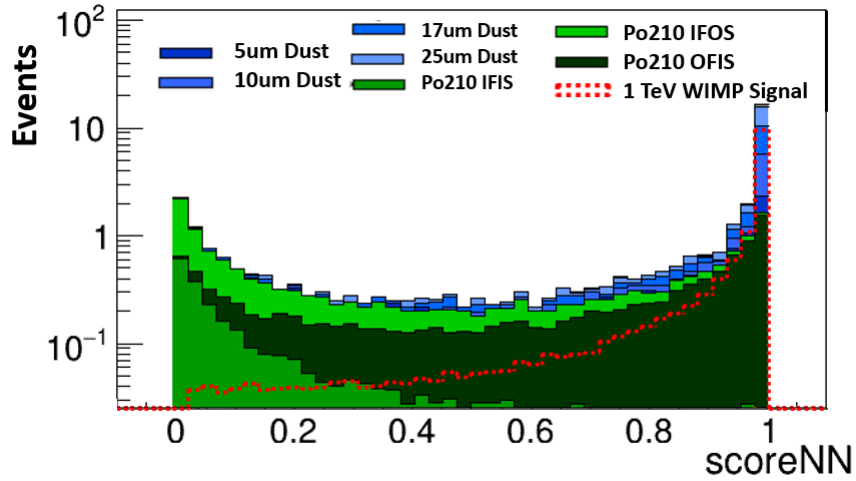


Figure 6.7: Neural Network estimator distribution for simulated background and signal samples after low-level event-quality cuts, and positional cuts from Table 6.2. Background simulations are stacked, with dust alpha events plotted in blue, and neck alpha events in green. Dashed line shows simulated 1 TeV/ $c^2$  WIMP at  $10^{-45}$   $\text{cm}^2$  cross-section signal distribution.

All three estimators efficiently complete their task of rejecting neck alpha events. The vast majority of neck events (represented by green bars) are closer to 0, while signal (red dashed line) events are very close to 1. These variables present a new

way of mitigating neck events in the dark matter search. A new event selection can be developed that includes one (or some combination of) these estimators, while loosening the costly neck rejection cuts, along with the radial cut of 630 mm.

### 6.1.3 Grid Scan

To find the optimal event selection, a grid scan is performed. A candidate range is defined for each potentially loosened cut, displayed in Table 6.3.

Table 6.3: Range of candidate values for event selection optimization. Potential values are iterated through, replacing previous cut in Table 6.2, and optimizing for Asimov significance. MVA estimators are considered both individually and in combinations of two.

Variable	Previous Cut	Candidate Range
Reconstructed Radius [mm]	630 mm	[630 - 720] mm
Z Position Consistency Contour	90% accep.	[75, 100]%
3D Position Consistency Contour	85% accep.	[75, 100]%
PE:Fprompt Region of Interest	30% NR accep. loss	[1%, 55%] NR accep. loss
MVA estimator	None	[0, 0.99]

The scan will iterate over all combinations of these cuts, applying the complete event selection to the simulated background samples, as well as a simulated signal sample. A program was written in PyROOT to take as input the trigger rates defined in Table 6.1, getting a prediction of the number of background and signal events in 376 live days. For each potential event selection, the scan looks for the optimal Asimov significance approximation, a close estimator to signal sensitivity. The significance is defined as [53]:

$$Z_A = \sqrt{(2 * (s + b) * \ln(1 + \frac{s}{b}) - 2s)} \quad (6.1)$$

Where  $Z_A$  is the significance,  $s$  is the amount of signal, and  $b$  is the amount of background.

At first a wide scan is performed for each MVA estimator. Upon reaching an

optimized area in the grid scan, the scan is repeated in greater detail in the area of the maximum. In this fine scan, the sensitivity for a  $1 \text{ TeV}/c^2$  WIMP at  $10^{-45} \text{ cm}^2$  cross-section is optimized. This is done by calculating the signal acceptance and number of background events for a given livetime. These numbers are then used to generate a number of excluded WIMP events for the mass hypothesis. With this value, and the livetime, an excluded cross-section at this mass can be hypothesized.

As mentioned before, the process is done completely with simulated samples, using dust alpha, neck alpha and neutron backgrounds. For the simulated signal sample, a simulation of  $^{40}\text{Ar}$  nuclear recoils is generated. This sample is then reweighted to match the WIMP PE spectrum for a  $1 \text{ TeV}/c^2$  WIMP nuclear recoil at  $10^{-45} \text{ cm}^2$  cross-section.

In the previous study a zero background study was targeted, where the expected number of background events in the dark matter search area was reduced to less than 1 event [16]. To repeat this, the grid scan was run with the condition that the expected number of background events was less than 1 in the full livetime of 802 live days. Initial returns on the grid scan showed a serious problem with this condition, the dust alpha background is not efficiently eliminated by any existing cuts. This is evident in Figure 6.5 (and the other estimator distributions) where dust alphas, plotted in blue, are treated as signal like. Figures displaying the distribution of simulated dust alpha events across the neck rejection cuts (Figure 6.2, 6.3, and 6.4) also show a behaviour mimicking WIMP signal events. A reduction to less than 1 background event would force an event selection with an extremely low signal acceptance, and consequentially, a poor dark matter sensitivity. Because of this, this initial condition of less than 1 event is removed. Instead the event selection is optimized for a background subtraction model, where a given number of background events is predicted and removed from the final analysis. This gives much more room to find the ideal event selection optimization.

The grid scan code outputs a table of candidate event selections, sorted by the Asimov significance or sensitivity. It also produces a heat map in ROI:estimator space for each combination of radius and position reconstruction cut. This optimization process was done for each estimator individually, as well as for combinations. Heat maps for all three estimators can be seen in Appendix B. For example, the heat map for RF and NN estimator mixing is shown in Figure 6.8 on the next page. In these plots the Asimov significance or sensitivity is on the z-axis, with a better sensitivity to dark matter being in yellow. Table 6.4 shows the optimized event selection for each score, as well as all combinations of two scores. For each event selection, the 90% confidence limit sensitivity to 1 TeV/c<sup>2</sup> WIMPs is displayed. The table is sorted by sensitivity. In all cases, the optimized event selection came with a removed 3D position consistency cut, and expanding the radial cut to 720 mm.

Table 6.4: Optimized event selection for each estimator, and combinations of two, with sensitivity to 1 TeV/c<sup>2</sup> WIMPs. For all combinations, the best sensitivity came with a removed 3D position consistency cut, expanded radial cut to 720 mm, and unchanged Z position consistency cut. Choices of event selection are sorted by sensitivity. These sensitivities are 90% confidence level (CL) limits calculated using the QWimp software. They do not account for uncertainties in the background model.

Estimator Cuts	ROI Choice	1 TeV/c <sup>2</sup> WIMP Sens. (cm <sup>2</sup> )
RF>0.848 + NN>0.342	1% Accep. Loss	6.17×10 <sup>-45</sup>
RF>0.848	5% Accep. Loss	6.30×10 <sup>-45</sup>
RF>0.848 + XGB>0.100	5% Accep. Loss	6.30×10 <sup>-45</sup>
XGB>0.956 + NN>0.340	1% Accep. Loss	6.54×10 <sup>-45</sup>
XGB>0.964	5% Accep. Loss	6.59×10 <sup>-45</sup>
NN>0.940	5% Accep. Loss	7.39×10 <sup>-45</sup>

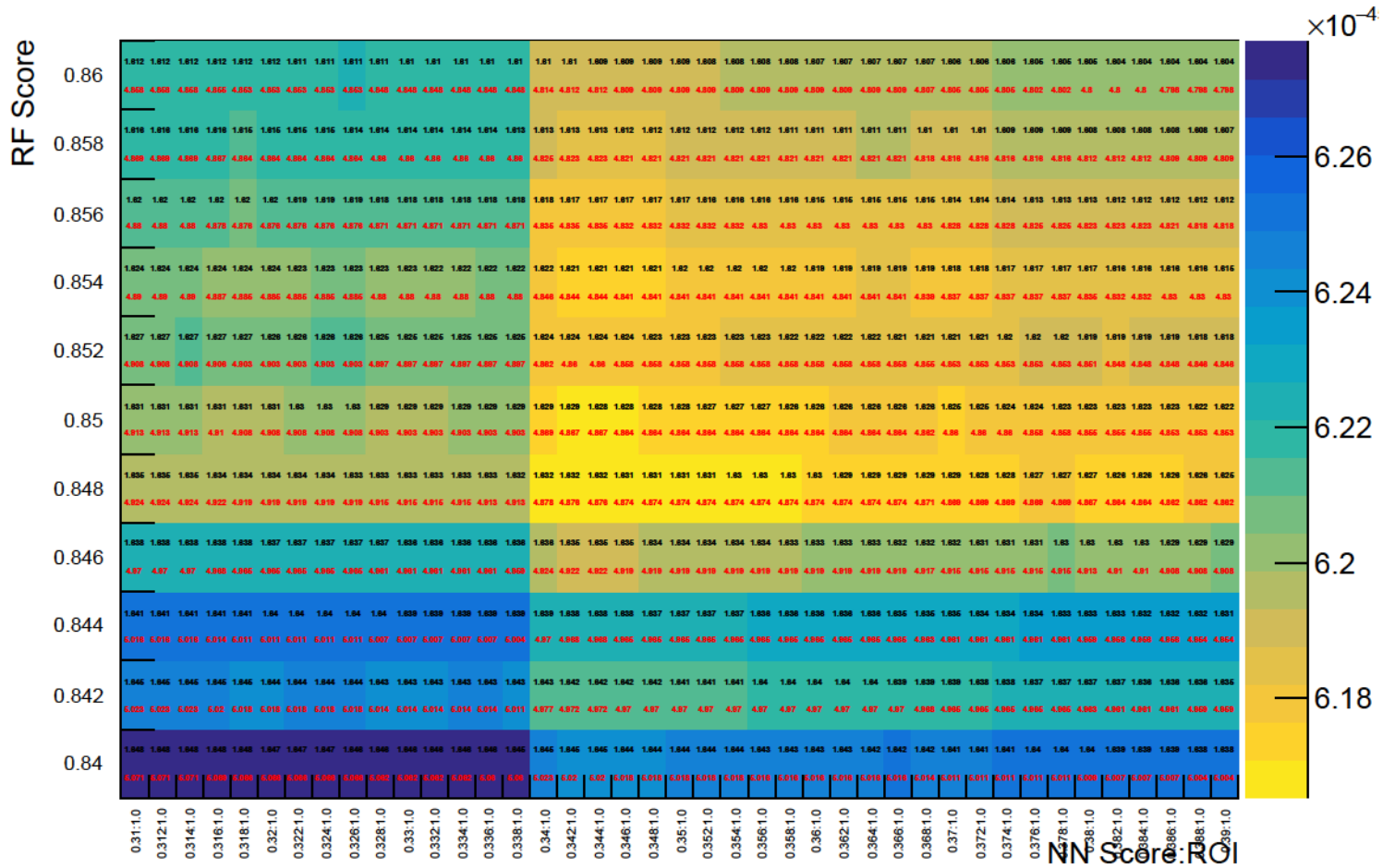
The best optimization came when using the Random Forest estimator of RF>0.848, along with a very loose Neural Network cut of NN>0.342. This event selection includes an expansion to the 1% nuclear recoil acceptance loss ROI, the widest ROI definition available. As noted earlier, this ROI expansion is into the neck alpha band in Figure 2.5, along with a small expansion in PE range. Alternatively, the best single estimator event selection was achieved with just the RF>0.848 cut, along with

a slightly tighter 5% ROI to counteract the missing Neural Network cut. The difference in sensitivity is very small, and for the sake of simplicity, the single estimator RF event selection is recommended for use as the optimized event selection.

To summarize, the new optimized event selection is the same as Table 6.2, with four changes:

- Expanding the fiducial radius to 720 mm
- Removing the 3D Position Consistency contour cut
- Expanding the ROI to the 5% nuclear recoil acceptance loss ROI
- Adding a cut on the Random Forest Estimator of  $RF > 0.848$

Sensitivity For Varying Cutflows (MBR = 720.0, PIFGAR = 2.0, RCUT = 100.0, MVA Type = MIX)



06

Figure 6.8: Event selection optimization grid scan results for RF estimator, optimizing for  $1 \text{ TeV}/c^2$  WIMP sensitivity. Y-axis is RF estimator. X-axis is repeated NN estimator over different ROI cut values.  $1 \text{ TeV}/c^2$  WIMP sensitivity is in Z-axis. Text within the boxes shows signal events (black) and background events (red) for the given event selection. This selection is for a 720 mm radial cut, and removed Position Consistency 3D cut. The optimal event selection can be seen at a cut on RF estimator  $> 0.848$ .

### 6.1.4 New Event Selection Signal Acceptance

With this new event selection, the signal acceptance must be formally calculated. This is done using the reweighted simulated  $^{40}\text{Ar}$  samples described earlier. There are two ways to quote the signal acceptance, within the fiducial volume after the position cuts, or a complete acceptance over the whole detector. Both versions will be calculated for better comparison with previous estimates, which used the acceptance within the fiducial volume. Before this can be done, the changes to the radial cut require a new calculation of the contained mass. These values can be found by applying the positional cut acceptance on the full detector mass:

$$M = \epsilon_{\text{pos.}} * (3729 \pm 96 \text{ [kg]}) \quad (6.2)$$

Where  $\epsilon_{\text{pos.}}$  is the cut efficiency of the positional cuts, taken as the number of events after both the positional and low-level cuts are applied, divided by the number of events after just the low-level cuts are applied (see Table 6.2). Applying this to the mass of liquid argon in the detector gives the contained mass  $M$ . This calculation is done for both the previous event selection in Table 6.2, and the optimized version with the change to the radial cut. The positional cuts are made up of the reconstructed R and Z cuts, as well as the charge fraction top two rings and charge fraction bottom three rings cuts. The contained mass must consider all of these cuts, which impact the volume of liquid argon being used for the dark matter search. These calculations are in Table 6.5.

The expanded radius cut increases the final contained mass by 66%, largely impacting the signal acceptance of the experiment. This change would not be evident when quoting the signal acceptance within the contained mass. The values for the previous event selection are consistent with those found in the 231 live day paper [16].

Table 6.5: Contained mass calculations based on cumulative position acceptance. Calculations are done for 231 live day event selection (Table 6.2) and current optimization. The only change is the loosened reconstructed R cut. Calculations are performed using Equation 6.2. Statistical uncertainties for the acceptance are listed.

Position Acceptance Simulated Signal Samples		
231 Live Day Event Selection		
Cut	Acceptance	Contained Mass (kg)
Reconstructed R>630 mm & Z>550 mm	38.1% $\pm$ 0.1%	1249 $\pm$ 37
Removing Events from Top 2 Rings	28.1% $\pm$ 0.1%	921 $\pm$ 27
Removing Events from Bottom 3 Rings	25.1% $\pm$ 0.1%	824 $\pm$ 24
New Optimization		
Cut	Acceptance	Contained Mass (kg)
Reconstructed R>720 mm & Z>550 mm	58.5% $\pm$ 0.1%	1918 $\pm$ 56
Remove Events from Top 2 Rings	47.6% $\pm$ 0.1%	1528 $\pm$ 45
Remove Events from Bottom 3 Rings	42.8% $\pm$ 0.1%	1371 $\pm$ 40

Now the signal acceptance calculations can be performed. The signal acceptance within the fiducial volume will be referenced as  $A_{\text{fid}}$ , while the full acceptance will be referenced as  $A_{\text{full}}$ . The equations for both are:

$$A_{\text{fid}} = \frac{N_{\text{all}}}{N_{\text{low-level, pos., ROI PE}}} \quad (6.3)$$

$$A_{\text{full}} = \frac{N_{\text{all}}}{N_{\text{low-level}}} \quad (6.4)$$

Again these equations deal with cut efficiencies, with the difference between the two acceptance equations being the denominator. For  $A_{\text{full}}$  (the full signal acceptance), the efficiency is calculated as the number of simulated signal events after all cuts,  $N_{\text{all}}$ , divided by the number of events after just the low-level event quality cuts  $N_{\text{low-level}}$ . For the fiducial acceptance  $A_{\text{fid}}$ , the denominator is instead the number of events after the low-level, positional, and the WIMP ROI PE cut,  $N_{\text{low-level, pos., ROI PE}}$ . This PE region is [93, 200] PE in the 30% ROI, and [80, 200] PE in the 5% ROI. The resulting calculations for both can be found in Table 6.6.

To better observe the improvements gained by expanding the radial cut, the full

signal acceptance should be quoted. The previous event selection results in an acceptance of  $0.98 \pm 0.01\%$ , while the optimized event selection increases this to  $2.68 \pm 0.03\%$ . This is a nearly 3 times increase in WIMP acceptance.

Table 6.6: Signal acceptance for previous and optimized event selection, quoted both within the fiducial volume (Equation 6.3), and over the entire detector volume (Equation 6.4). Calculated using simulated  $^{40}\text{Ar}$  signal samples weighted to match WIMPs. Statistical uncertainties are listed as well.

Event Selection	Fiducial Signal Acceptance	Full Signal Acceptance
Previous (Tab. 6.2)	$17.1^* \pm 0.2 \%$	$0.98 \pm 0.01 \%$
Optimized	$26.0 \pm 0.4 \%$	$2.68 \pm 0.03 \%$

\*R position reconstruction consistency cut does not affect simulated samples the same way as data. Because of this, the value here does not match the previously quoted acceptance value of 25%. This does not affect the optimized study, where this cut is omitted.

The final acceptance has an asterisk with it for the original cut. In the previous study, a signal acceptance of 25% was quoted, disagreeing with this 17.09% calculation. This is due to a disagreement in cut efficiency between data and simulations for the 3D position reconstruction cut. The 231 live day study used select  $^{39}\text{Ar}$   $\beta$ -decay data events to calculate the acceptance. This disagreement was recreated for this study for consistency, and the same results were found. The disagreement does not affect the optimized event selection, as the 3D position reconstruction cut is removed from the event selection. A better comparison between data and simulation would be between 25% for the original event selection and 26.04% for the new event selection. While this is a small difference, it does not take into account the changes to the contained mass.

## 6.2 Expected Alpha Background Yield in the DM Search ROI

The final step in a full study on alpha backgrounds in the DEAP-3600 dark matter search is to quantify the alpha background yield in the dark matter search region of interest. This was already done to some degree in the previous section, where estimates of the yield were used to educate an event selection optimization. That analysis did not include the impact of systematic uncertainties on the study. In this section, a full analysis of the yield is done for the three alpha backgrounds: neck, dust and surface. This analysis includes predictions and systematic variations for both the previous event selection in Table 6.2, and the optimized version. The process mainly revolves around converting the determined trigger rates (in Table 6.1) into estimates using the study livetime and the event selection efficiency. In the case of livetime, 376 live days are used to match the open dataset. In future studies, the values can be scaled to larger livetimes, including the full second-fill dataset livetime of 802 days.

First the neck alpha and dust alpha estimates will be addressed. Due to their large presence in the WIMP dark matter search ROI, the simulated samples can be used to find a reliable event selection efficiency. Many events within these simulated samples survive the two event selections, and the event selection efficiency calculation will not be affected by poor stats. This is not true for the surface alphas, and their estimate calculation must be treated differently.

### 6.2.1 Neck Alpha Yield

For each component, an estimate of the total number of events after a given event selection is calculated. Similarly to the grid scan, neck alpha trigger rates are combined with the open dataset livetime and simulated samples to find these values.

The results for all three flowguide components, for both the previous and optimized

event selection, are displayed in Table 6.7. This estimate process is also repeated for the upper and lower bounds of the trigger rate uncertainty (Table 5.3), giving an asymmetric uncertainty to these yield estimates. These trigger rates were developed using the neck alpha control regions, and did not account for potential shape changes from the systematic variation. Comparisons made in Figures 5.9 and 5.10 displaying systematic variation variable shapes showed consistency between the samples in all cases except the intermediate LAr pulseshape systematic. As expected, altering the pulseshape influences the FPrompt distribution, pulling the neck alphas into the dark matter FPrompt region. This systematic was treated with more attention, using the full simulated sample to determine the dark matter event selection efficiency.

This more thorough treatment was also applied to the 25  $\mu\text{m}$  LAr layer systematic variation. In this case, a sizeable portion of the alphas (roughly half) emitted into the liquid argon exit, and enter the gaseous argon. This creates GAr scintillation that lowers the Fprompt distribution out of the dark matter search ROI. This variation also necessitated a much larger trigger rate to match the data in the nuclear recoil control region. To properly account for these changes to the FPrompt distribution, the simulated sample is used to generate a new set of trigger efficiencies, reducing the yield in the ROI. As such, the dominant systematic variation within the ROI becomes the intermediate LAr pulseshape.

The final results of combining the systematic uncertainties is displayed with the nominal value in Table 6.7.

Component	Previous Selection	Optimized Selection
IFIS	$0.113^{+0.172}_{-0.003}$	$0.072^{+0.049}_{-0.007}$
OFIS	$0.198^{+0.072}_{-0.038}$	$0.128^{+0.108}_{-0.012}$
IFOS	$0.217^{+0.346}_{-0.025}$	$0.102^{+0.029}_{-0.025}$
Total	$0.528^{+0.393}_{-0.046}$	$0.302^{+0.122}_{-0.028}$

Table 6.7: Neck alpha estimates in the dark matter search region of interest, for both the previous and optimized event selection, for 376 live days.

### 6.2.2 Dust Alpha Yield

Moving on to dust alphas, the same method is used. The trigger rates defined in Table 6.1 for the five dust sizes are used, along with the simulated samples, and the 376 day livetime.

For the systematic variations, all systematic variations listed in Section 4.2.2 are considered. For each variation, a set of dust alpha samples are simulated (all sizes). These samples are then normalized to the expected number of dust events, and an estimate of events within the dark matter search region is calculated. This can be compared directly to the central value.

Shape comparisons between the nominal sample and the systematic variations are displayed in Appendix C. Variables plotted are PE (Figure C.1),  $F_{\text{prompt}}$  (Figure C.2) and the reconstructed radius (Figure C.3). Distributions are consistent with the nominal, with no unexpected deviations.

Following the formula set out in Section 4.2.2, an asymmetric uncertainty is developed from these variations due to systematic uncertainties.

$$\text{Dust Alpha Total original} = 0.88^{+0.16}_{-0.23}$$

$$\text{Dust Alpha Total optimized} = 2.02^{+0.40}_{-0.41}$$

There are additional systematic uncertainties being explored for the dust alpha model. A large portion of these uncertainties pertain to the qualities of the dust. The range of dust particulate sizes comes from the acrylic vessel resurfacing. The resurfacing process, aimed at lowering the radon activity, was done with 10 tons of nitrogen inside the vessel. The filter used in this process had a  $50 \mu\text{m}$  pore size [31]. Different intervals of sizes and higher upper limits can be a potential systematic. There is also the potential for different metallic dusts, as well as acrylic dust from the resurfacing, or norite dust from SNOLAB rocks to be present. Finally different shapes of dust can be considered, as the nominal simulation only creates spherical dust. Oblate spheroid dust can be generated as well.

Additionally, there are some systematic uncertainties that can be applied in the fitting process. An excess of events in low reconstructed  $Z$  in the alpha region indicates dust may be  $Z$  dependent. Including a  $Z$  dependence in the fit could account for this.

Finally, the current alpha quenching model is not well defined, and is explored further in Appendix A. Changes to this model would impact the dust spectrum at low PE and the yield in dark matter search.

### 6.2.3 Surface Alpha Yield

An estimate of the surface alpha background in the dark matter search region must be approached differently. Because the radial cut is so effective (see Figure 4.13) there is a lack of statistics within the optimized fiducial volume of 720 mm. This lack of statistics is only increased with the previous cut of 630 mm. In both cases, simulated samples do not have enough events within this range to generate a useful event selection efficiency for the full dark matter search selection.

Further, it is not possible to extrapolate into the ROI using simulated events due to disagreement between simulated surface alpha events and data. Comparing the  $F_{\text{prompt}}$  distribution of simulated events to data shows that data is more prompt than

simulation. This plot is shown in Figure 6.9. If the  $F_{\text{prompt}}$  distribution in simulated samples is lower than the true distribution in data, the surface alpha background yield would be underestimated. Due to this, simulated samples can not be used to make meaningful dark matter search ROI predictions, and instead a data-driven approach is taken.

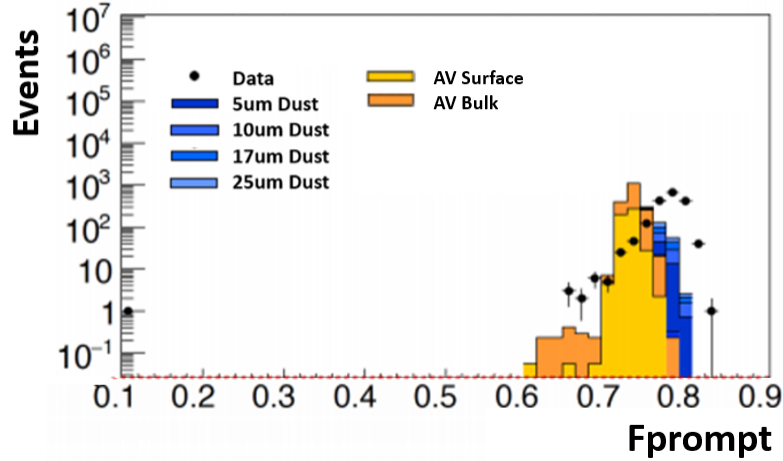


Figure 6.9:  $F_{\text{prompt}}$  distribution of simulated surface alphas (yellow/orange) vs data (black) in surface alpha validation region. Dust background (blue) is also plotted. Data is more prompt than simulations, leading to a potential underestimate of surface alpha yield in the dark matter ROI.

A low PE data control region for surface alphas can not be attained. At the dark matter PE level of 80-200 PE, the vast majority of surface alpha events are removed, and it is difficult to separate surface alphas from other events occurring at the surface (i.e.  $^{39}\text{Ar}$  decays, dust alpha events, Cherenkov). Instead, for a conservative upper limit, it is easier to select any events that construct near the surface in this PE window. This can be done using the  $n_{\text{Hit}}/\text{PE}$  distribution, where  $n_{\text{Hit}}$  is defined as the number of PMTs registering a signal in the event.

This distribution, shown for the  $^{210}\text{Po}$  LAr/TPB interface sample after some low-level cuts in Figure 6.10, is sensitive to the topology of events. By selecting events in the dataset that mimic the distributions seen in the LAr/TPB interface figure, one

can create a surface event control region without relying on position reconstruction. The contours defined in Figure 6.10 are designed to do this.

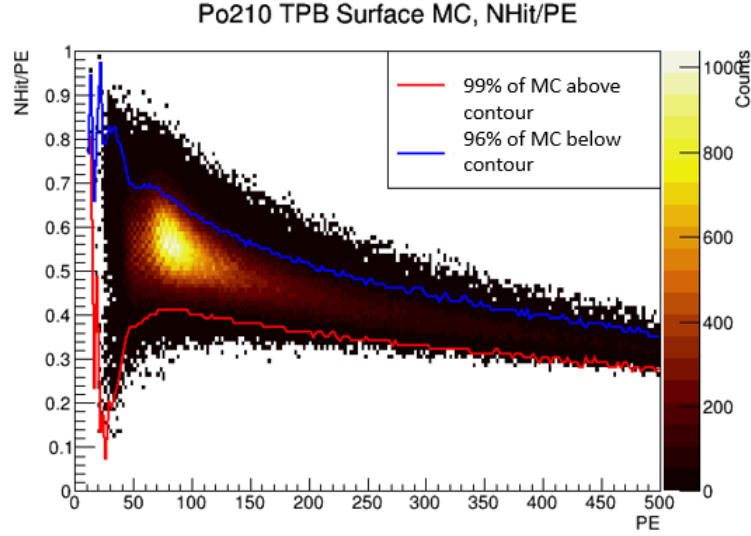


Figure 6.10: nHit/PE distribution as a function of PE for simulated  $^{210}\text{Po}$  TPB/LAr interface samples. Acceptance contours selecting 1% (red) and 96% (blue) of events are drawn over distribution. These contours are used to create a 2D contour cut for data.

If some added preselection cuts are applied to the dataset along with these contours, a population of surface alpha candidate events within the dark matter search ROI can be selected.

This preselection is a superset of the original event selection, listed in Table 6.2. The low-level cuts are included to remove any unwanted data. The positional cuts are not included in this preselection, as they would remove surface alpha candidates. The position reconstruction consistency contours are not included. Included is the 30% NR acceptance loss ROI. A large portion of surface events at this low PE range are  $^{39}\text{Ar}$  beta decays occurring at the edge of the liquid argon mass. These events have a lower  $F_{\text{prompt}}$  in the electronic recoil band, and can be removed from the preselection with the lower bound of the ROI.

After applying this preselection to data, the nHit/PE distribution is displayed in

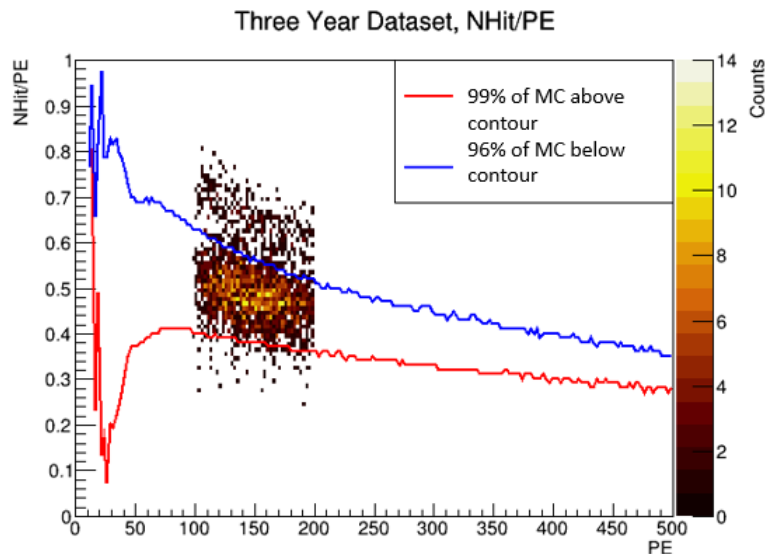


Figure 6.11:  $n\text{Hit}/\text{PE}$  distribution of 376 live days of data after low-level preselection in dark matter search ROI. Acceptance contours from simulated surface alpha sample in Figure 6.10 are drawn. Events between the contours (1,305 events) are surface events that exist within the dark matter ROI, and are considered as surface alpha candidates.

Figure 6.11, with events outside of the contour removed. Events within the contours are deemed ROI surface alpha candidate events. These events pass the low-level preselection, exist within the dark matter search ROI, and are selected as surface events from the  $n\text{Hit}/\text{PE}$  contours. There are 1,305 events in 376 live days of data within these contours. To make sure the  $n\text{Hit}/\text{PE}$  contour cut is working as intended, these events are plotted in reconstructed radius, along with the events above the contours, in Figure 6.12. These events are exclusively high in radius, as intended, and the events outside the contour are lower in radius. None of the 1,305 candidate events survive the reconstructed radius cuts of 630 mm and 720 mm.

The optimized event selection includes an expansion of the WIMP region of interest to the 5% nuclear recoil acceptance loss contour. This change does not affect the part of the region of interest rejecting  $^{39}\text{Ar}$  decays. Instead the expansion is only into the neck alpha band from Figure 2.5, and into lower PE regions (from 93 to 80 PE). This increase in ROI increases the number of surface candidate events from

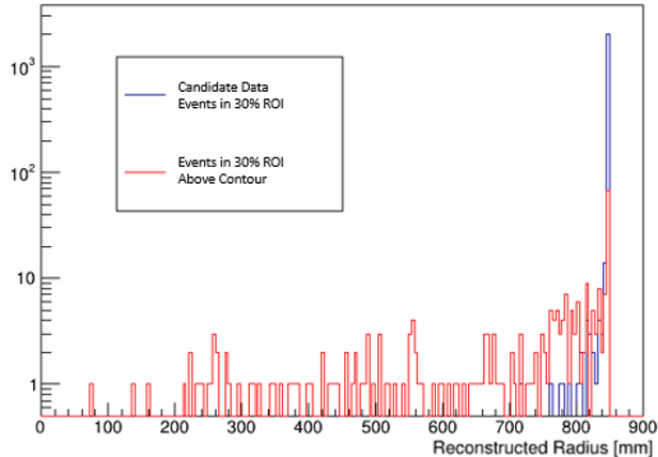


Figure 6.12: Reconstructed radius of the 1,305 candidate events within nHit/PE contours (blue) and above the nHit/PE contours (red). Events within the contours reconstruct exclusively at high radius.

1,305 to 1,880.

This selection of candidate surface events represents a selection of events in the 376 live day dataset, near the surface of the detector, that pass low-level cuts and are within the ROI. None of these 1,880 events survive the either the previous or optimized event selection. Regardless, there is still the potential for surface events to reconstruct within the fiducial volume, as can be seen in Figure 4.13. The 90% confidence limit of the leakage fraction from these leakage distributions can be applied to this estimate. This gives a conservative upper limit on the number of surface alpha events within the dark matter search event selection.

First, for the previous event selection, with a radial cut of 630 mm. The 90% CL leakage fraction is given in Equation 4.17 as  $3.97 \times 10^{-5}$ . Applying this to 1,305 events gives:

$$N_{SA}^{ROI} < 0.05 \text{ (90\% CL, previous)} \quad (6.5)$$

For the optimized event selection, with a radial cut of 720 mm, the 90% CL leakage fraction from Equation 4.19 is  $8.94 \times 10^{-5}$ . This is applied to the number of surface

alpha candidate events in the 5% ROI, 1880. This gives a final upper limit of:

$$N_{SA}^{ROI} < 0.17 \text{ (90\% CL, optimized)} \quad (6.6)$$

In both cases a 90% CL is used to give an upper bound accounting for systematics, as the surface alphas are still a very small portion of the full background model.

## 6.2.4 Summary and Exclusion Curves

In summary, the alpha yields in the dark matter search, for both the previous and optimized event selection, are presented below in Table 6.8, for 376 live days. All are presented with systematic uncertainties, with events from alpha decays occurring at the acrylic vessel inner surface quoted as an upper limit at 90% CL.

Table 6.8: Summary of alpha yields in dark matter search region of interest for original and optimized event selections. The results are for 376 live days. Signal acceptance for a 1 TeV/c<sup>2</sup> WIMP at 10<sup>-45</sup> cm<sup>2</sup> cross-section is included for reference.

Alpha Source	Yield, Original Selection	Yield, Optimized Selection
Neck Flowguide	0.53 <sup>+0.30</sup> <sub>-0.05</sub>	0.30 <sup>+0.17</sup> <sub>-0.03</sub>
Dust	0.88 <sup>+0.16</sup> <sub>-0.23</sub>	2.02 <sup>+0.40</sup> <sub>-0.41</sub>
Inner AV and TPB Surface	<0.05	<0.17
Signal Acceptance	0.98 ± 0.01 %	2.68 ± 0.03 %

This analysis gives a predicted number of alpha background events for the open dataset livetime. Along with the rest of the background model, these yields can be combined with the signal acceptance calculated earlier in the section to find the number of excluded WIMP events. Combining this number with the livetime and contained mass allows the generation of some preliminary sensitivity curves for the new event selection, displayed in Figure 6.13. These curves are generated using a program called QWimp, created by Mark Boulay to plot exclusion curves. These

curves can be compared to the result from the 231 live day analysis.

The previous result was created using a code developed by Shawn Westerdale called MaxPatch, which employs a more detailed calculation of the exclusion curve. This code accounts for the impacts of the ROI shape on the signal acceptance, while QWimp uses a simpler approach, taking signal acceptance as an input parameter. Work has been done to recreate the MaxPatch 231 live day curve using QWimp, and agreement between the two is consistent, and good for this preliminary study.

A portion of the increased WIMP sensitivity between the previous result and this thesis comes from the increase in livetime. The impact of this increase is displayed in Figure 6.13. It is further increased when using the new optimized event selection. Displayed is the exclusion curve for the full 802 day livetime if no background subtraction is applied, as well as the potential impact of background subtraction down to one event as an example.

The improvement to sensitivity is notable, even without any applied subtraction. These are preliminary values that do not account for potential uncertainties in the model and signal acceptances. The expected upper limits at 90% CL to a 100 GeV/c<sup>2</sup> (1 TeV/c<sup>2</sup>) WIMP in the 231 live day curve is  $3.9 \times 10^{-45} \text{ cm}^2$  ( $1.5 \times 10^{-44} \text{ cm}^2$ ) [16]. With the new event selection and larger livetime, the upper limits go to  $1.9 \times 10^{-45} \text{ cm}^2$  ( $6.6 \times 10^{-45} \text{ cm}^2$ ), assuming no background subtraction. If we assume background subtraction down to 1 event in the dark matter search, the upper limits go to  $7.4 \times 10^{-46} \text{ cm}^2$  ( $2.6 \times 10^{-45} \text{ cm}^2$ ). For direct comparison, one can also consider the sensitivity using the new event selection, scaled down to 231 live days. In this case, the limit goes to  $3.1 \times 10^{-45} \text{ cm}^2$  ( $1.1 \times 10^{-44} \text{ cm}^2$ ) assuming no background subtraction.

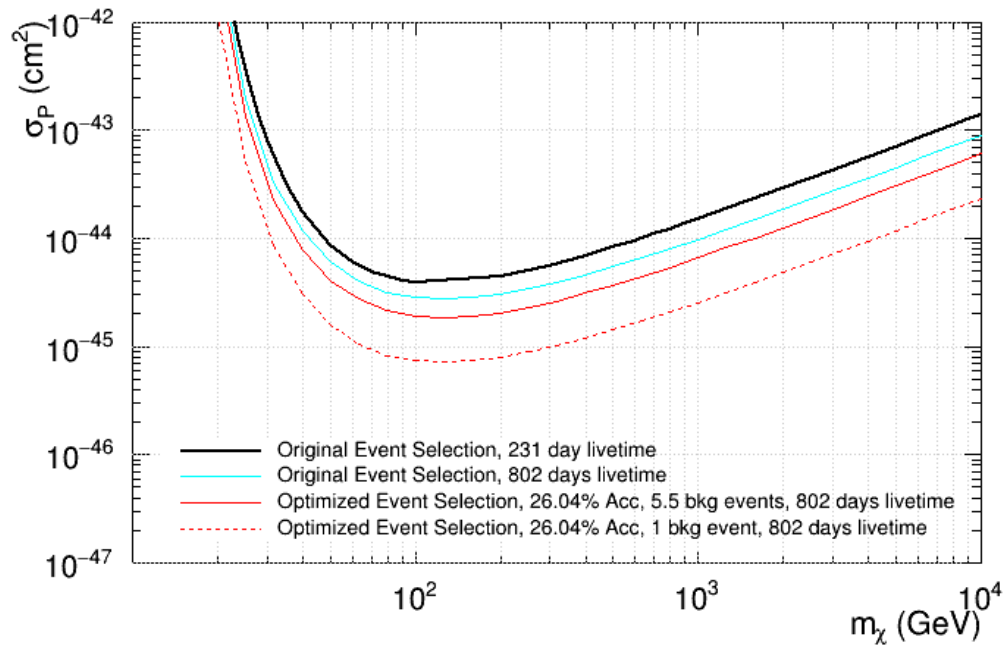


Figure 6.13: Preliminary exclusion curves comparing the impacts of the optimized event selection (red) and increased livetime (cyan) to the previous result (black). This previous result uses 231 live days compared to 802 live days for the new analysis. The potential impact of background subtraction is shown in broken line, subtracting to 1 background event in the ROI. This study does not account for uncertainties on acceptance and background model.

# Chapter 7

## Conclusion

While evidence for dark matter continues to grow, the actual nature of this matter is still unknown. The DEAP-3600 detector is a single-phase liquid argon direct detection experiment that uses scintillation light to track potential WIMP particles passing through the detector mass. As WIMPs interact weakly, that is at low cross-section, direct detection experiments require an extremely low background level. If this level is not reduced in situ, it must be mitigated through analysis. The dominant background in the DEAP-3600 dark matter search region of interest are attenuated alphas from  $^{210}\text{Po}$  decays occurring in materials around the liquid argon.

One of the main goals of this thesis was to quantify the current alpha background contribution to the WIMP search in the DEAP-3600 experiment. Alpha decay events originating from the acrylic vessel inner surface and acrylic neck flowguide are each treated individually. Improvements to the fitting process for both types of alpha backgrounds were made, including redefined control regions and improved models. An activity of  $0.22 \pm 0.02$  mBq/m<sup>2</sup> was calculated for the surface component of the acrylic vessel alphas. An activity of  $3.68 \pm 0.06$  mBq was calculated for the bulk component. The neck flowguide alphas were found to have a total event rate of  $53.5^{+30}_{-4.6}$   $\mu\text{Hz}$ .

In this thesis, it was shown that the surface alpha background is largely mitigated through radial cuts, with rejection on the order of  $10^{-5}$  when reducing the positional acceptance to 58.5%. However, there is still some potential for leakage coming from gaps in PMT coverage around the detector. The current surface alpha contribution is negligible, however in the future, work can be done on refining the position reconstruction around these gaps. If consistent angular reconstruction within the gaps can be attained, a new conical cut can be defined to remove any events originating from these areas.

The neck alpha model was improved with optimized control regions and the inclusion of the dust background in the fit. The simulated samples were generated with a  $50\ \mu\text{m}$  LAr film around the flowguides to allow for scintillation light. This film could possibly be a liquid argon mist, with scintillation light produced from droplets. Work is underway on exploring this mist hypothesis, and its agreement with data in the neck control regions.

Appendix A outlines the current treatment of the alpha quenching factor, and a potential improvement is proposed. Future work should incorporate this new model in simulated attenuated alpha samples. This will likely further improve the current activity and dark matter search estimates.

An estimate of the alpha background yield in the dark matter search was made for all three major alpha background components. Due to the disagreement in the pulse-shape discrimination variable for surface alphas, a conservative approach was taken. Surface events were isolated in the dataset, and treated as surface alpha candidates. In this way, an upper limit was calculated. Future work exploring and potentially correcting this disagreement would allow for a more precise measurement of the surface alpha yield using simulated samples. Improvements to the alpha quenching model in Appendix A could improve this distribution.

This alpha background model was combined with the rest of the background

templates and new background rejection techniques to generate an optimized event selection. This event selection, based around machine-learning algorithms aimed at rejecting neck events, resulted in a factor 2.7 improvement in WIMP acceptance. This translated to a preliminary 90% CL cross-section upper limit of  $1.9 \times 10^{-45}$  cm<sup>2</sup> for a WIMP mass of 100 GeV/c<sup>2</sup> assuming no background subtraction, an improvement on the previously published analysis results [16]. This optimized event selection is designed for background subtraction. If we assume subtraction down to 1 background event in the dark matter search, the expected limit goes down to  $7.4 \times 10^{-46}$  cm<sup>2</sup>. The previous zero background analysis was found to be inefficient given the presence of the dust alpha background.

The work presented in this thesis, and new rejection techniques, allow for an efficient mitigation of surface and neck alpha backgrounds. As a result of this, dust alphas become the dominant background source in the experiment. A large portion of current work by the DEAP collaboration is on finding an efficient way to reject this background, including with likelihood techniques and machine-learning algorithms. Having an efficient method of removing dust would allow for a much more comprehensive scan of potential event selections, and a hopefully much stronger WIMP sensitivity.

# Bibliography

- [1] Planck Collaboration. Planck 2018 results. *Astronomy & Astrophysics*, 641:A6, Sep 2020.
- [2] J. Billard et al. Direct detection of dark matter – APPEC committee report, 2021.
- [3] H. Andernach and F. Zwicky. English and Spanish translation of Zwicky’s (1933) The redshift of extragalactic nebulae, 2017.
- [4] F. Zwicky. On the Masses of Nebulae and of Clusters of Nebulae. *The Astrophysical Journal*, 86:217, 1937.
- [5] F. Zwicky. On the large scale distribution of matter in the universe. *Physical Review*, 61:489–503, 1942.
- [6] V. C. Rubin, D. Burstein, W. K. Ford, and N. Thonnard. Rotation velocities of 16 SA galaxies and a comparison of Sa, SB and SC rotation properties. *The Astrophysical Journal*, 289:81–104, 1985.
- [7] V. C. Rubin and W. K. Ford. Rotation of the Andromeda Nebula from a Spectroscopic Survey of Emission Regions. *The Astrophysical Journal*, 159:379, 1970.
- [8] Y. Friedman and J. M. Steiner. Gravitational deflection in relativistic Newtonian dynamics. *Europhysics Letters*, 117(5):59001, Mar 2017.

- [9] D. Clowe et al. A direct empirical proof of the existence of dark matter. *The Astrophysical Journal*, 648(2):L109–L113, 2006.
- [10] J. L. Feng. Dark matter candidates from particle physics and methods of detection. *Annual Review of Astronomy and Astrophysics*, 48(1):495–545, 2010.
- [11] A. Weltman et al. Fundamental physics with the Square Kilometre Array. *Publications of the Astronomical Society of Australia*, 37, 2020.
- [12] T. Bringmann and C. Weniger. Gamma ray signals from dark matter: Concepts, status and prospects. *Physics of the Dark Universe*, 1(1-2):194–217, 2012.
- [13] M. Felcini on behalf of the ATLAS and CMS Collaborations. Searches for dark matter particles at the LHC. In *Proceedings of the 53rd Rencontres de Moriond on Cosmology*, 2018.
- [14] Super-Kamiokande Collaboration. Indirect search for dark matter from the Galactic Center and halo with the Super-Kamiokande detector. *Physical Review D*, 102(7), 2020.
- [15] ANTARES Collaboration and IceCube Collaboration. Combined search for neutrinos from dark matter self-annihilation in the Galactic Center with ANTARES and IceCube. *Physical Review D*, 102(8), 2020.
- [16] DEAP Collaboration. Search for dark matter with a 231-day exposure of liquid argon using DEAP-3600 at SNOLAB. *Physical Review D*, 100(2), 2019.
- [17] XENON Collaboration. Dark matter search results from a one ton-year exposure of XENON1T. *Physical Review Letters*, 121:111302, 2018.
- [18] PandaX-II Collaboration. Dark matter results from 54-ton-day exposure of PandaX-II Experiment. *Physical Review Letters*, 119:181302, 2017.

- [19] LUX Collaboration. Results from a search for dark matter in the complete LUX exposure. *Physical Review Letters*, 118:021303, 2017.
- [20] DarkSide Collaboration. DarkSide-50 532-day dark matter search with low-radioactivity argon. *Physical Review D*, 98:102006, 2018.
- [21] DEAP Collaboration. Design and construction of the DEAP-3600 dark matter detector. *Astroparticle Physics*, 108:1–23, 2019.
- [22] H. Araújo and V. Chepel. Liquid noble gas detectors for low energy particle physics. *Journal of Instrumentation*, 8(04):R04001–R04001, 2013.
- [23] E. Segreto. Properties of liquid argon scintillation light emission. *Physical Review D*, 103(4), 2021.
- [24] E. Doke, A. Hitachi, J. Kikuchi, K. Masuda, H. Okada, and E. Shibamura. Absolute scintillation yields in liquid argon and xenon for various particles. *Japanese Journal of Applied Physics*, 41:1538, 02 2002.
- [25] F. Duncan, A.J. Noble, and D. Sinclair. The construction and anticipated science of SNOLAB. *Annual Review of Nuclear and Particle Science*, 60(1):163–180, 2010.
- [26] C. Jillings for the DEAP Collaboration. Control of contamination of radon-daughters in the DEAP-3600 acrylic vessel. *AIP Conference Proceedings*, 1549(1):86–89, 2013.
- [27] Hamamatsu Photonics K.K. *Large Photocathode Area Photomultiplier Tube*, 2019. Available at [https://www.hamamatsu.com/resources/pdf/etd/LARGE\\_AREA\\_PMT\\_TPMH1376E.pdf](https://www.hamamatsu.com/resources/pdf/etd/LARGE_AREA_PMT_TPMH1376E.pdf).
- [28] DEAP Collaboration. In-situ characterization of the Hamamatsu R5912-HQE photomultiplier tubes used in the DEAP-3600 experiment. *Nuclear Instruments*

- and Methods in Physics Research Section A: Accelerators, Spectrometers, Detectors and Associated Equipment*, 922:373–384, 2019.
- [29] V.M. Gehman, S.R. Seibert, K. Rielage, A. Hime, Y. Sun, D.-M. Mei, J. Maassen, and D. Moore. Fluorescence efficiency and visible re-emission spectrum of tetraphenyl butadiene films at extreme ultraviolet wavelengths. *Nuclear Instruments and Methods in Physics Research Section A: Accelerators, Spectrometers, Detectors and Associated Equipment*, 654(1):116–121, 2011.
- [30] DEAP Collaboration. Application of the TPB wavelength shifter to the DEAP-3600 spherical acrylic vessel inner surface. *Journal of Instrumentation*, 12(04):P04017–P04017, 2017.
- [31] P. Giampa for the DEAP Collaboration. *Identification and Reduction of the Alpha Background, From  $^{238}\text{U}$  and  $^{232}\text{Th}$  Decay Chains, in the DEAP-3600 Experiment*. PhD thesis, Queen’s University, Kingston, ON, 2017.
- [32] P. Amaudruz et al. The data acquisition architecture for the “dark matter experiment using argon pulse-shaped discrimination” — DEAP-3600. In *2016 IEEE-NPSS Real Time Conference (RT)*, pages 1–7, 2016.
- [33] T. Caldwell. Simulation of noble liquid detectors using RAT. Presented at AARM Meeting at Fermilab, 2014.
- [34] DEAP Collaboration. Pulse shape discrimination against low-energy  $\text{Ar-39}$  beta decays in liquid argon with 4.5 tonne-years of DEAP-3600 data, 2021. Submitted. arXiv:2103.12202.
- [35] DEAP Collaboration. DEAP-3600 dark matter search. *Nuclear and Particle Physics Proceedings*, 273-275:340–346, 2016.

- [36] J. Calvo et al. Backgrounds and pulse shape discrimination in the ArDM liquid argon TPC. *Journal of Cosmology and Astroparticle Physics*, 2018(12):011–011, 2018.
- [37] DEAP Collaboration. Electromagnetic backgrounds and potassium-42 activity in the DEAP-3600 dark matter detector. *Physical Review D*, 100(7), 2019.
- [38] J. A. Formaggio and C.J. Martoff. Backgrounds to sensitive experiments underground. *Annual Review of Nuclear and Particle Science*, 54(1):361–412, 2004.
- [39] Berkeley Nuclear Forensics Website. Th-232 and U-238 decay chains. Available at <https://metadata.berkeley.edu/nuclear-forensics/Decay%20Chains.html>.
- [40] T. Pollmann for the DEAP Collaboration. *Alpha backgrounds in the DEAP Dark Matter search experiment*. PhD thesis, Queen’s University, Kingston, ON, 2012.
- [41] J. Bonatt for the DEAP Collaboration. Radioreduction and radiopurity of acrylic in the DEAP-3600 dark matter experiment. Master’s thesis, Queen’s University, Kingston, ON, 2017.
- [42] J. McLaughlin for the DEAP Collaboration. Corrections to signal saturation on the DEAP-3600 dark matter search. Master’s thesis, Queen’s University, Kingston, ON, 2018.
- [43] C. Mielnichuk for the DEAP Collaboration. A likelihood ratio algorithm for removing localized alpha particle backgrounds in the DEAP-3600 detector. Master’s thesis, University of Alberta, Edmonton, AB, 2017.
- [44] A. Grobov and A. Ilyasov for the DEAP-3600 collaboration. Boosted decision trees approach to neck alpha events discrimination in DEAP-3600 experiment. *Physica Scripta*, 95(7):074007, 2020.

- [45] P. Gorel. Revisiting the target mass, 2021. Internal communication.
- [46] A. Butcher et al. A method for characterizing after-pulsing and dark noise of PMTs and SiPMs. *Nuclear Instruments and Methods in Physics Research Section A: Accelerators, Spectrometers, Detectors and Associated Equipment*, 875:87–91, 2017.
- [47] T. Pollmann, M. Boulay, and M. Kuźniak. Scintillation of thin tetraphenyl butadiene films under alpha particle excitation. *Nuclear Instruments and Methods in Physics Research Section A: Accelerators, Spectrometers, Detectors and Associated Equipment*, 635(1):127–130, Apr 2011.
- [48] E. Grace, A. Butcher, J. Monroe, and J. Nikkel. Index of refraction, Rayleigh scattering length, and Sellmeier coefficients in solid and liquid argon and xenon. *Nuclear Instruments and Methods in Physics Research Section A: Accelerators, Spectrometers, Detectors and Associated Equipment*, 867:204–208, 2017.
- [49] M. Babicz, S. Bordoni, A. Fava, U. Kose, M. Nesi, F. Pietropaolo, G. L. Raselli, F. Resnati, M. Rossella, P. Sala, F. Stocker, and A. Zani. Light propagation in liquid argon. Submitted. arXiv:2002.09346, 2020.
- [50] G. Louppe. *Understanding Random Forests: From Theory to Practice*. PhD thesis, University of Liege, Liege, Belgium, 2015.
- [51] T. Chen and C. Guestrin. XGBoost. *Proceedings of the 22nd ACM SIGKDD International Conference on Knowledge Discovery and Data Mining*, Aug 2016.
- [52] L. Shiloh-Perl and R. Giryes. Introduction to deep learning. arXiv:2003.03253 [cs.LG], 2020.

- [53] G. Cowan, K. Cranmer, E. Gross, and O. Vitells. Asymptotic formulae for likelihood-based tests of new physics. *The European Physical Journal C*, 71(2), 2011.
- [54] D.-M. Mei, Z.-B. Yin, L.C. Stonehill, and A. Hime. A model of nuclear recoil scintillation efficiency in noble liquids. *Astroparticle Physics*, 30(1):12–17, Aug 2008.
- [55] A. Hitachi. Luminescence response and quenching models for heavy ions of 0.5 keV to 1 GeV/n in liquid argon and xenon. *Instruments*, 5(1), 2021.
- [56] J. Lindhard, M. Scharff, and H. E. Schiøtt. Range concepts and heavy ion ranges (notes on atomic collisions, II). *Kgl. Danske Videnskab. Selskab. Mat. Fys. Medd.*, Vol: 33: No. 14, 1 1963.
- [57] J. Ziegler, M. D. Ziegler, and J. P. Biersack. SRIM - The stopping and range of ions in matter. *Nuclear Instruments and Methods in Physics Research B*, 268(11-12):1818–1823, 2010.
- [58] J. B. Birks. Scintillations from organic crystals: Specific fluorescence and relative response to different radiations. *Proceedings of the Physical Society. Section A*, 64(10):874–877, 1951.
- [59] J. LaVerne, A. Hitachi, J.J. Kolata, , and T. Doke. Scintillation and ionization in allene-doped liquid argon irradiated with  $^{18}\text{O}$  and  $^{36}\text{Ar}$  ions of 30 MeV/u. *Physical Review B - Condensed Matter and Materials Physics*, 54:15724–15729, 1996.
- [60] P. Agnes et al. Measurement of the liquid argon energy response to nuclear and electronic recoils. *Physical Review D*, 97(11), 2018.

- [61] DarkSide Collaboration. Simulation of argon response and light detection in the DarkSide-50 dual phase TPC. *Journal of Instrumentation*, 12(10):P10015–P10015, 2017.
- [62] H. Cao et al. Measurement of scintillation and ionization yield and scintillation pulse shape from nuclear recoils in liquid argon. *Physical Review D*, 91(9), 2015.
- [63] M.J. Berger, J.S. Coursey, M.A. Zucker, and J. Change. Stopping-power & range tables for electrons, protons, and helium ions. *NIST Standard Reference Database 124*, 2017. Available at <https://dx.doi.org/10.18434/T4NC7P>.

# Appendix A

## Alpha Quenching in Liquid Argon

### A.1 Review of Alpha Quenching in LAr Scintillation Detectors

One of the key parameters for noble liquid scintillators is the scintillation efficiency. Only a portion of the energy deposited by an incoming particle results in ionization and excitation that leads to scintillation light: this effect is called quenching. The quenching factor (as the particle is "quenched" as it passes through the medium) is defined as

$$q_f = \frac{E_{scint}}{E} \tag{A.1}$$

Where  $E$  is the full energy deposited by the nuclear recoil, and  $E_{scint}$  is the energy that contributes to the scintillation process.

Quenching is dependent on the recoiling particle type. In the case of electronic recoils from  $e$  and  $\gamma$ , the scintillation efficiency is assumed to be close to 1, as energy loss is converted into scintillation light through electron-ion recombination [54]. For nuclear recoils from WIMPs and alphas, however, this parameter is less than 1, and is

dependent on the incoming particle energy. There are two main classes of quenching, each with their own model and treatment. These are named nuclear quenching, and luminescent quenching.

Along the incoming particle's track it collides with electrons and nuclei within the detector. Some energy is transferred to transitional motion. In this way, energy is lost to the medium that does not result in scintillation light, similar to heat loss. After a scatter, the target Ar nucleus can also transfer some energy this way. Both of these are components of nuclear quenching. This effect is more pronounced at lower nuclear recoil energies, especially the WIMP region of interest. It is proportional to the energy of the incoming nucleus, and its atomic mass and number.

The second class of quenching is luminescent quenching. This form of quenching is a result of ionic processes that do not result in the emission of a scintillation photon. As the incoming particle passes through, a number of free excitons are created in the target material. Exciton-exciton collisions can occur [55], in the form of:



The outgoing electron carries some kinetic energy that is lost before recombination. This results in a lost exciton without scintillation light. These excitons can also undergo Penning ionization, where the exciton interacts with a ground state argon nucleus, but creates an ionized atom and an emitted electron [55]. Again, energy lost to this electron is not converted to scintillation, and is another form of quenching. While nuclear quenching is dependent on the nuclear stopping power, luminescent quenching depends on the electronic stopping power.

The two classes of quenching are handled separately, and the total quenching factor  $q_f$  is a combination of the two,  $q_n \times q_l$ . This appendix focuses on the effects of these quenching factors on alpha particles in the DEAP-3600 liquid argon detector. The current parameterization of these two factors, and their role in simulations of the

detector are described. From this some attempts to improve the model are made. The work done in this appendix is a combination of work between the author and two other collaboration members, David Gallacher, and Michael Perry, whose contributions are attributed below.

## A.2 Alpha Quenching in DEAP-3600 Simulations

Simulations in the DEAP-3600 experiment are performed using the RAT software, described in Section 2.2. Alpha quenching is currently recreated in RAT with the treatment described in Mei et al. (2008) [54]. In this paper, separate prescriptions are used, one for the nuclear quenching, and one for the luminescent quenching. The resulting quenching factor (the product of the two) is directly applied to the energy deposited at each point in the alpha particle track.

Nuclear quenching is handled using the analytical "Lindhard Equation", designed in 1963 [56]. This form uses the atomic mass, number, and energy of the incoming particle to calculate  $q_n$ . In its full form the equation is:

$$q_n = \frac{kg(\epsilon)}{1 + kg(\epsilon)} \quad (\text{A.3})$$

$$g(\epsilon) = 3\epsilon^{0.15} + 0.7\epsilon^{0.6} + \epsilon \quad (\text{A.4})$$

Where  $\epsilon$  is a dimensionless measurement of the incoming particle energy:

$$\epsilon = E \frac{a_0 0.8853 (Z_1^{2/3} + Z_2^{2/3})^{-1/2} M_2}{Z_1 Z_2 e^2 (M_1 + M_2)} \quad (\text{A.5})$$

and  $k$  is a constant dependent on the types of particles interacting:

$$k = 0.0793 \frac{Z_1^{3/5} Z_1^{1/2} Z_2^{1/2} (A_1 + A_2)^{3/2}}{(Z_1^{2/3} + Z_2^{2/3})^{3/4} A_1^{3/2} A_2^{1/2}} \quad (\text{A.6})$$

In these equations,  $E$  is the incoming particle energy in MeV,  $a_0$  is the Bohr radius in fm,  $e$  is the elementary charge in MeV\*fm units, and  $Z_{1/2}/A_{1/2}$  are the atomic number/mass of the incoming particle and material.

This treatment is an effective quenching model. The value of  $q_n$  is calculated at the beginning of the alpha track, using the starting energy for  $E$ . This effective value is applied to the energy deposited at each point in the track to model nuclear quenching.

This equation, in its full form, is directly implemented in the simulation. Work is being done to verify that this analytical solution is accurate for alphas. This work includes using the computer program SRIM (Stopping and Range of Ions in Matter) [57] to numerically calculate the nuclear quenching factor. The simulation was performed by Michael Perry over a range of alpha starting energies. This was compared directly to the full analytical solution, and an approximation of the equation where the incoming particle and material nucleus are assumed to be the same. The results of Michael's simulations, compared to a plot of the analytical form, is shown in Figure A.1. There is a roughly 5-10% difference between SRIM and the Lindhard equation, with SRIM predicting stronger quenching effects. In both cases, they converge to no effect at higher energies. This difference will be revisited in the next section.

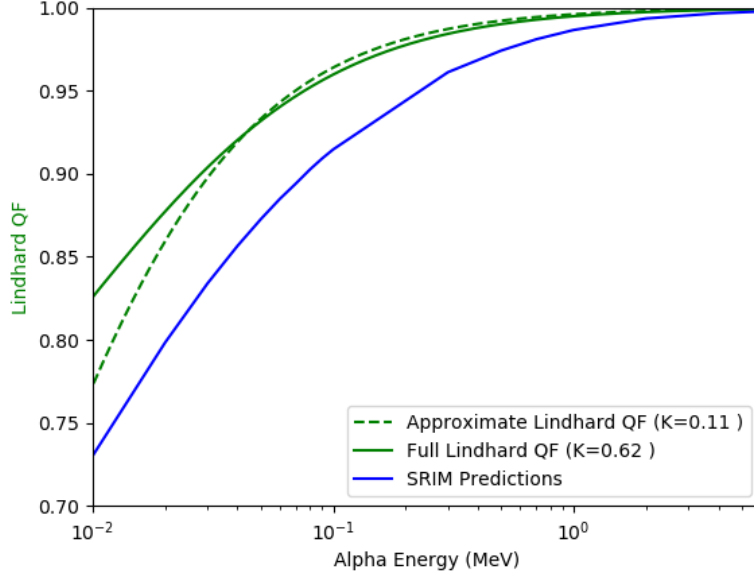


Figure A.1: Nuclear quenching factor in liquid argon for a range of alpha starting energies. The green lines use the analytical Lindhard solution, and an approximation of it. The blue line is the result of a SRIM simulation performed by Michael Perry. SRIM predicts a roughly 5-10% lower quenching factor than the Lindhard equation.

As for luminescent quenching, the treatment comes from Birk's Law [58]. This form is completely dependent on the electronic stopping power of the incoming particle in the scintillation material. Combining this stopping power with a free parameter ( $kB$ ) gives the equation for luminescent quenching:

$$q_l = \frac{1}{1 + kB \frac{dE}{dx}} \quad (\text{A.7})$$

$kB$  is a parameter of units  $\text{g}/\text{MeV}/\text{cm}^2$ , and is called the Birk's Constant. This equation is calculated at every step in the track of the alpha particle, and the value is applied to the energy deposited. The Mei et al. paper goes on to calculate this  $kB$  value for liquid argon. This is done using measurements from experiments done in the Michigan State University Cyclotron Laboratory [59]. These experiments involved calculating quenching factors for different large nuclei in a range of scintillator materials. For liquid argon,  $^{36}\text{Ar}$  atoms at  $31.9\text{MeV}/\text{u}$  were fired into the material,

and a quenching factor of 0.46 was found. This value, along with a calculated stopping power, was used to calculate a  $kB$  value of  $7.4 \times 10^{-4}$  g/MeV/cm<sup>2</sup> [54]. This value of  $kB$  is the one currently implemented in the DEAP-3600 simulation, along with the Birk's Law equation.

There is some concern that this value of  $kB$  is not appropriate for the lighter ions. While theoretically it should be independent of particle type, previous experiments have indicated otherwise. Multiple measurements of lighter particles in liquid argon have been performed, with the intention of measuring the luminescent quenching. Measurements using neutrons by the Aris collaboration and fit to Birk's Law quoted a  $kB$  of  $5.2 \pm 0.6 \times 10^{-4}$  g/MeV/cm<sup>2</sup> [60]. DarkSide-50k also performed a fit using neutron nuclear recoil data, measuring a  $kB$  of  $4.66^{+0.86}_{-0.94} \times 10^{-4}$  g/MeV/cm<sup>2</sup> [61]. Even with heavier ions discrepancy with the Mei et al. measurement is found. The SCENE collaboration used <sup>83</sup>Kr nuclear recoils to measure the value of  $kB$ , fitting out  $5.0 \pm 0.2 \times 10^{-4}$  g/MeV/cm<sup>2</sup> [62].

To validate the Birk's model in the DEAP simulation, a quenching factor fit is performed with the DEAP-3600 dataset. As the focus of this thesis is on attenuated alphas, it would be beneficial to use a range of starting alpha energies to fit out the Birk's Constant. The inputs and results of this fit are detailed in the next section.

There is an alternative parameterization of Birk's Law, from Hitachi (2021) [55]. This second version introduces a normalization constant, to allow for a larger range of energy dependencies in the fit. The new equation is:

$$q_l = \frac{A}{1 + kB \frac{dE}{dx}} \quad (\text{A.8})$$

Where A is the new unitless normalization constant. A fit is also performed with this version.

## A.3 Fitting Birk's Constant to DEAP-3600 Alpha Data

To effectively model alpha quenching in liquid argon, it would be best to use alpha data points in the Birk's Law fit. A final luminescent quenching factor is required for a range of alpha starting energies to be able to perform the fit. To find the quenching of an alpha event, the reconstructed energy from photoelectrons will be compared to the theoretical starting energy of the alpha. Because the amount of attenuation that occurs in surfaces can not be measured, degraded alphas can not be used in this analysis. Instead, the full energy bulk alphas emitted in the liquid argon bulk can be used. These alphas are emitted during the decay of  $^{214}\text{Po}$ ,  $^{218}\text{Po}$ , and  $^{222}\text{Rn}$  (see Figure 3.1 for the decay chain). These decays occur within the liquid argon bulk, so all of the starting alpha energy is deposited into the scintillation material. This means any difference from the starting energy and reconstructed energy from PE is due to quenching. The distribution of these alpha events in Reconstructed R:PE space can be seen in Figure 4.3.

Taking the central point of each peak gives a measurement of the total scintillation light from each alpha event. Using the measured light yield of liquid argon, this can be converted to an energy, and compared to the starting energy of the alpha. That ratio would be equivalent to the total quenching  $q_f$ . Because these alphas are at very high energy ( $>5$  MeV), the nuclear quenching factor is assumed to be equal to 1 (see Figure A.1). In this way, these quenching factors are entirely from luminescent quenching, and can be approximated as  $q_f = q_l$ . A table of these measured quenching factors is presented in Table A.1.

Work done by David Gallacher combines these quenching factor measurements with the electronic stopping power, and the fit is performed by David to get a Birk's Constant value. This is done for three different electronic stopping powers. The

Table A.1: Measured quenching factor of high energy alpha decays in liquid argon. The starting energy comes from Figure 3.1. The PE comes from isolating the high energy alpha peaks in Figure 4.3 and taking the mode of the PE distribution. A light yield of 6.1 PE/keV<sub>ee</sub> is used from [16].

Alpha	Starting Energy (keV)	PE	$q_f$
<sup>222</sup> Rn	5590	26600	0.768
<sup>218</sup> Po	6115	29300	0.773
<sup>214</sup> Po	7883	38000	0.778

current electronic stopping power is calculated in RAT using GEANT4 macros. This version is used in the fit, along with stopping powers calculated in SRIM [57], and stopping powers taken from a NIST (National Institute of Science and Technology) reference table [63]. The result of David’s work using RAT stopping powers gives a Birk’s Constant of  $kB = 5.27 \times 10^{-4}$  g/MeV/cm<sup>2</sup>. Uncertainties on this value still need to be developed. This is comparable to the values found in the other liquid argon quenching measurements. However, the fit still does not match well with data. Simulated alpha samples are generated using this new fit value and plotted against data in Figure A.2.

The PE distribution is lower than that in data. More importantly, this difference is not constant between the three peaks. The current form of Birk’s Law is too energy dependent, and causes an overprediction of the quenching factor for the high energy <sup>214</sup>Po peak. This is found fitting with all three different stopping powers, and with two different PE estimators. This form of Birk’s Law is not a good representation of the DEAP-3600 dataset.

The Hitachi version of Birk’s Law with normalization constant A (Equation A.8) results in a better fit. David repeated the fit with this change, resulting in less energy dependence in the Birk’s Law curve. In turn, this creates much better agreement at higher energy. The final result of this fit is shown in Figure A.3.

This form results in a Birk’s Constant of  $kB = 1.70 \times 10^{-4}$  g/MeV/cm<sup>2</sup> and a

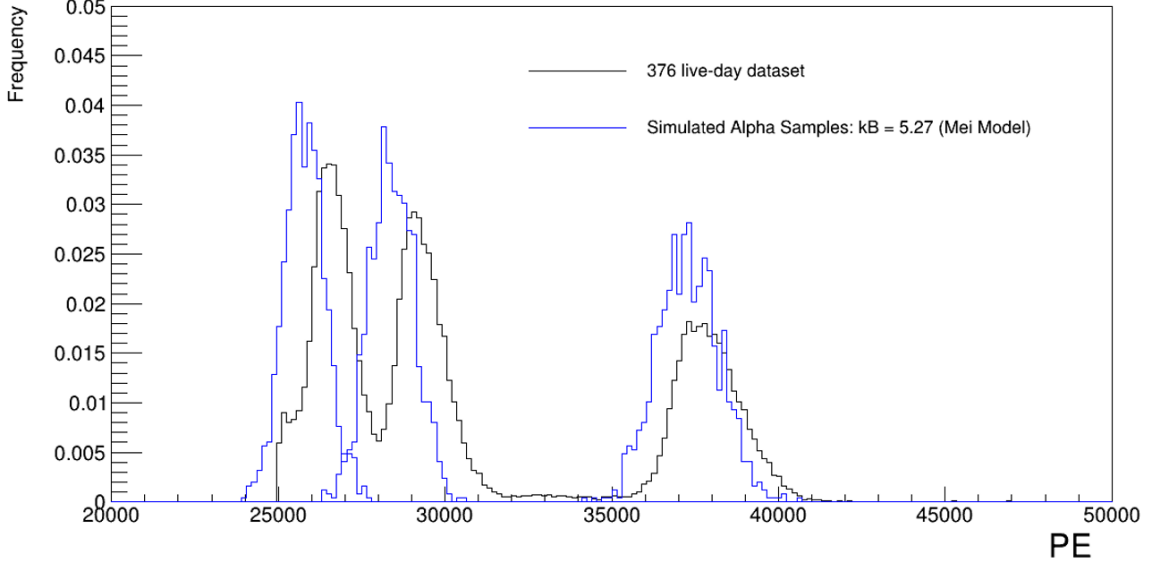


Figure A.2: PE distribution of alphas using best fit result (blue) of  $kB = 5.27$  mg/MeV/cm<sup>2</sup>. This fit is applied to the Mei et al. luminescent quenching model, using parameters from Table A.1. Data is also plotted in black for comparison.

normalization factor of  $A = 0.86$ . It should be noted that this model is an effective model, much like the nuclear quenching factor. This result is the preferred parameterization of the luminescent quenching factor, and has now been implemented into DEAP-3600 simulations.

## A.4 Validation and Summary

The recommended new model for alpha quenching combines some of the improvements found in this appendix. For the luminescent quenching, this means using the Hitachi version of Birk's Law [55] with the fitted parameters  $kB = 1.70 \times 10^{-4}$  g/MeV/cm<sup>2</sup> and  $A = 0.86$ . For nuclear quenching, this means using the SRIM calculated values from Figure A.1 instead of the analytical model. The two quenching models are combined together using  $q_f = q_n \times q_l$ . Simulated high alpha samples are generated using this new quenching factor model, and are plotted against data in Figure A.4. These new samples show much better agreement than the best fit of the

Mei et al. model in Figure A.2.

More validation will be completed, but going forward, these changes will be released in a newer version of RAT. These changes should have a strong impact on the alpha PE distributions, both at high and low energies. When the validation is complete, the alpha analysis in this thesis will have to be updated, in order to reach even more accurate values for the calculated activities and background yields to the dark matter search.

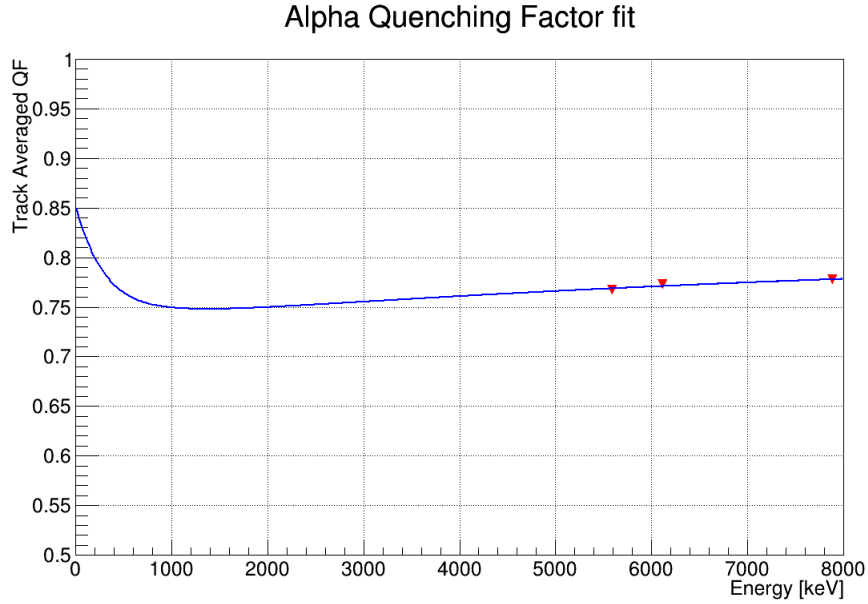


Figure A.3: Hitachi luminescent quenching model fit to high energy alpha quenching data from Table A.1. Best fit parameters are  $kB = 1.70 \times 10^{-4} \text{ g/MeV/cm}^2$  and  $A = 0.86$ . Uncertainties on the data points are arbitrary.

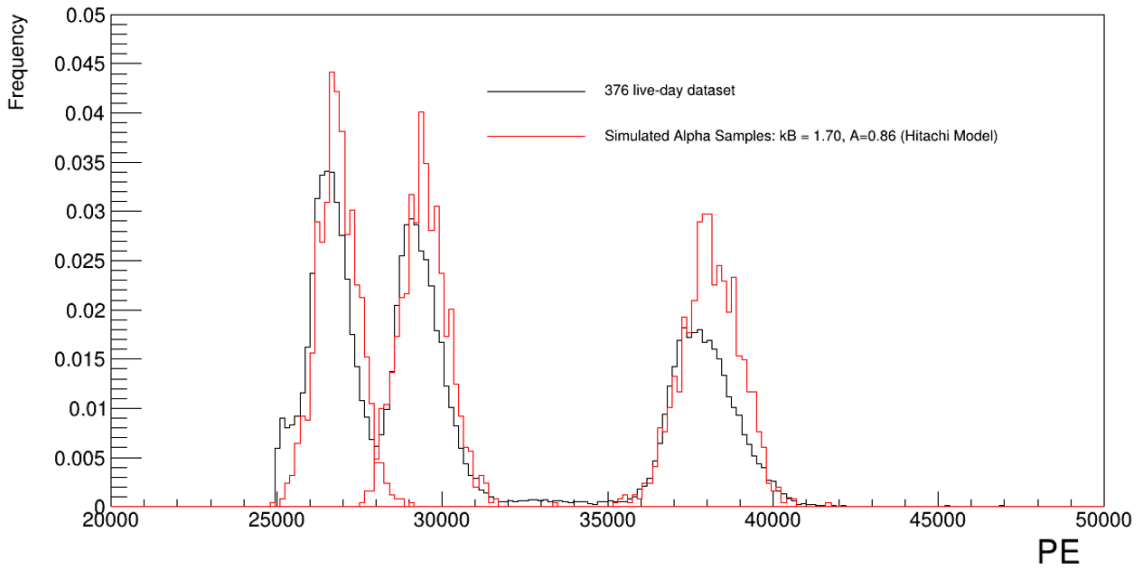


Figure A.4: PE distribution of alphas using the best fit result (blue) of  $kB = 1.70 \text{ mg/MeV/cm}^2$  and  $A = 0.86$ . This fit is applied to the Hitachi luminescent quenching model, using parameters from Table A.1. Data is also plotted in black for comparison.

# Appendix B

## Event Selection Optimization Heat Maps

The work in Chapter 6 revolves around introducing the new MVA estimators to the dark matter event selection. These estimators are designed to efficiently reject neck alphas, and accept WIMP signals. Three different versions of these estimators, each based on a different algorithm, were generated and applied to simulations and data.

To find which estimator to use, and the optimized event selection for it, a grid scan was performed. The details of the scan's range and results can be found in Chapter 6. Attached here are the resulting heat maps containing the optimized event selection for each combination of estimators. The y-axis contains one estimator score, the x-axis is a different score, repeated over different ROI options. The z-axis is the Asimov significance approximation (Equation 6.1), and in each cell is the number of background events and signal events yielded in the event selection.

Significance For Varying Cutflows (MBR = 720.0, PIFGAR = 2.0, RCUT = 100.0, MVA Type = RF)

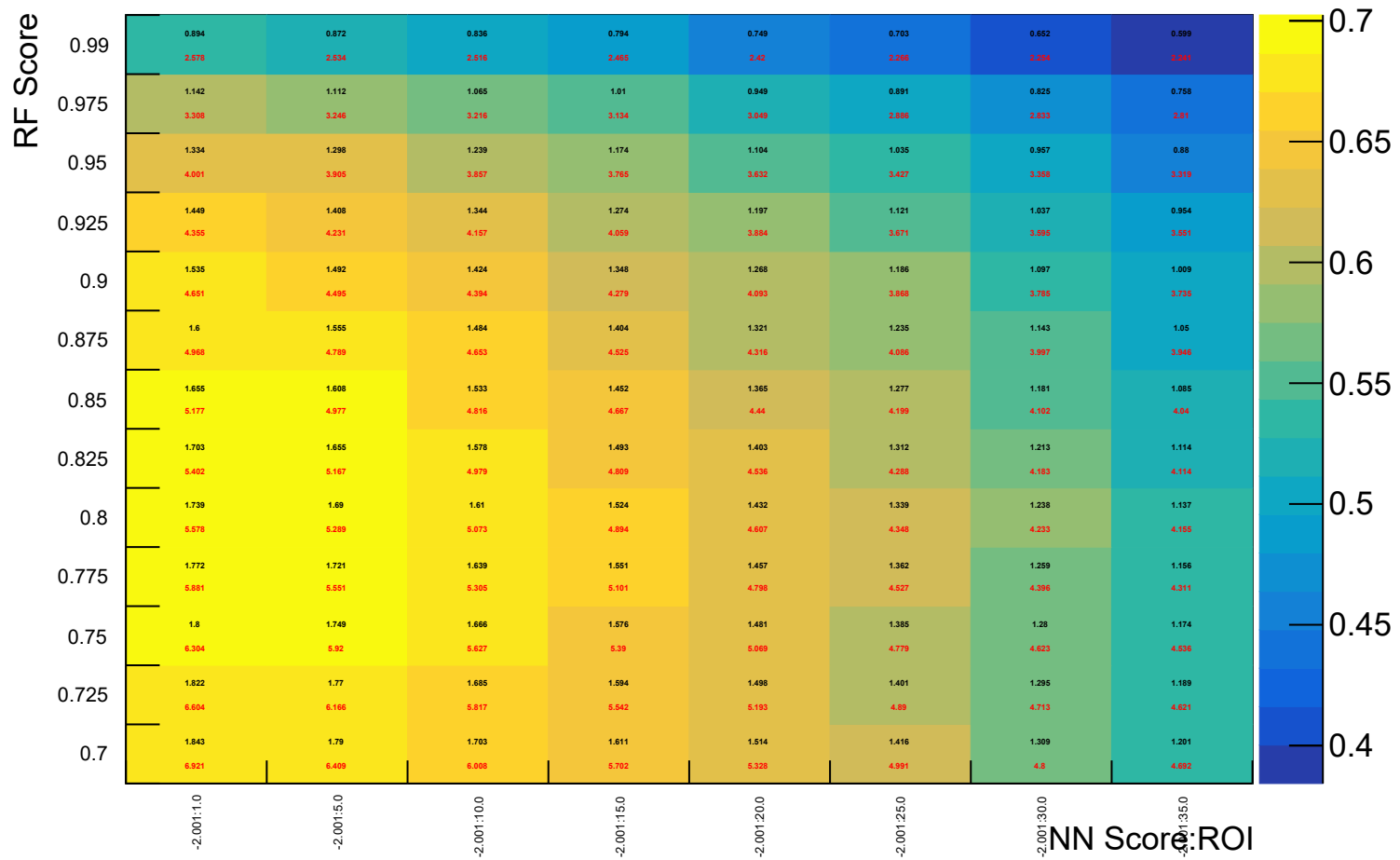


Figure B.1: Event selection optimization grid scan results for RF estimator, optimizing for Asimov significance approximation. Asimov significance in Z-axis. Text within boxes shows signal events (red) and background events (black). The y-axis is the RF score, while the x-axis is the neural network score (in this case set to -2 for omission) repeated over different ROI options.

Significance For Varying Cutflows (MBR = 720.0, PIFGAR = 2.0, RCUT = 100.0, MVA Type = XGB)

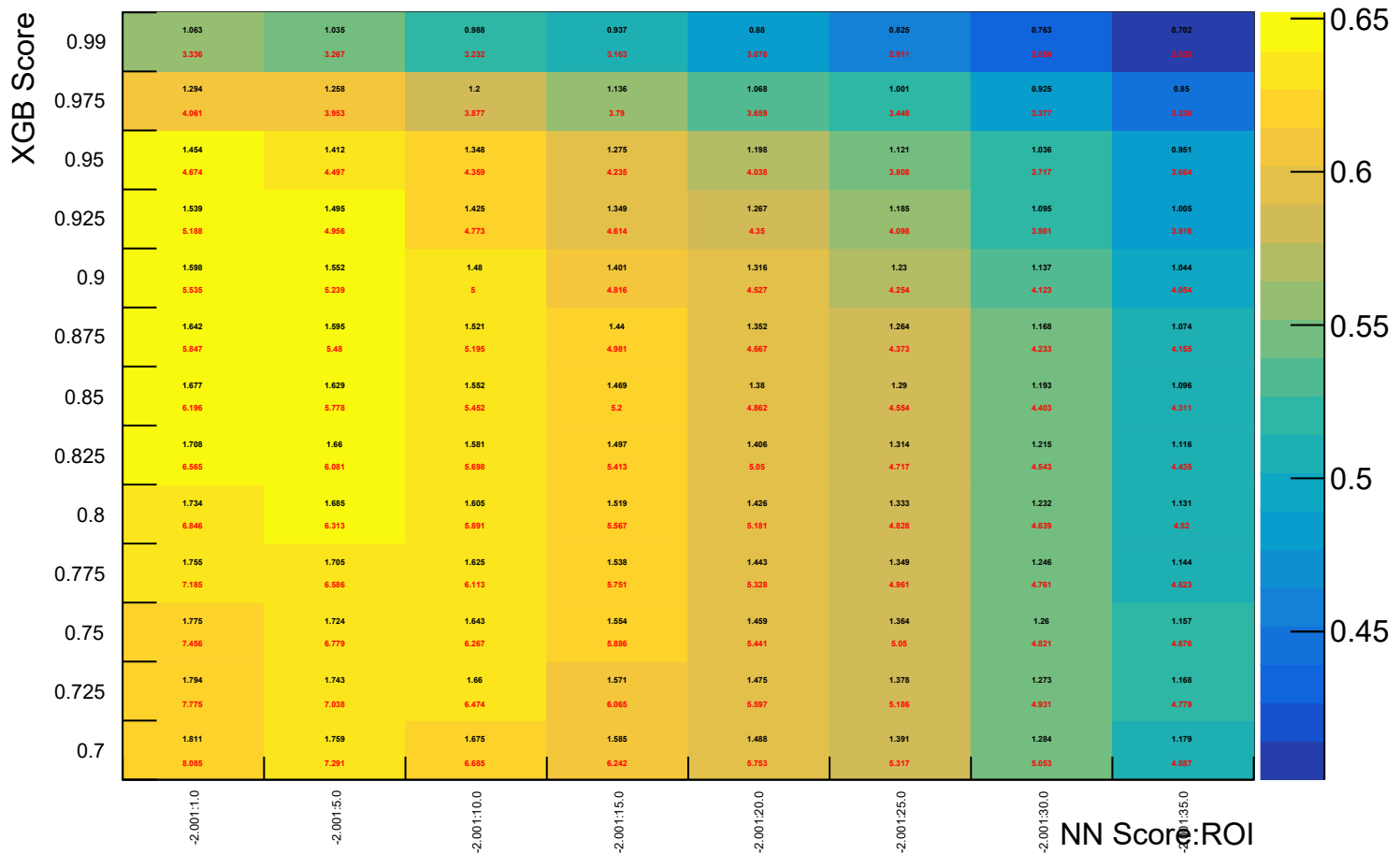
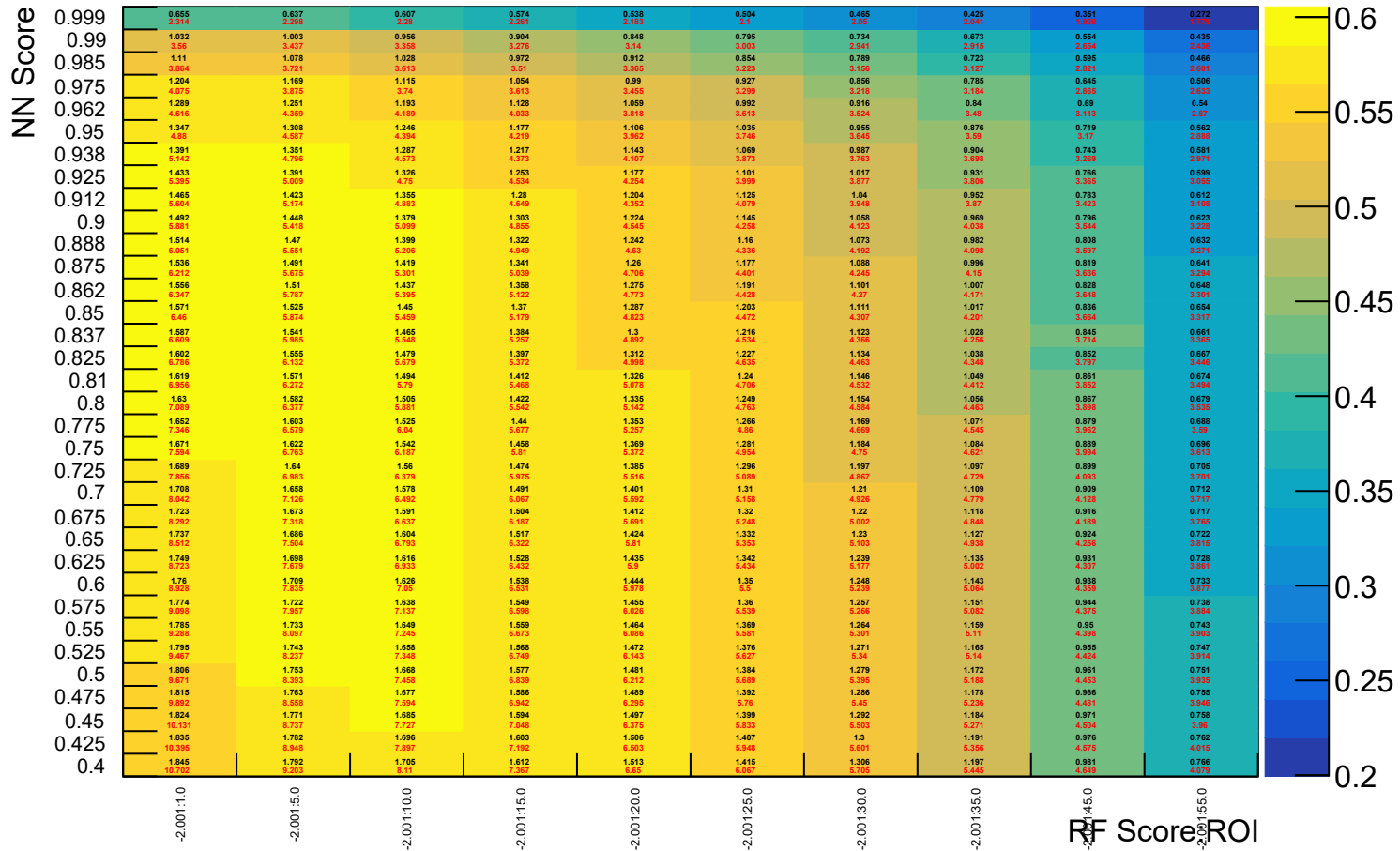


Figure B.2: Event selection optimization grid scan results for XGB estimator, optimizing for Asimov significance approximation. Asimov significance in Z-axis. Text within boxes shows signal events (red) and background events (black). The y-axis is the XGB score, while the x-axis is the neural network score (in this case set to -2 for omission) repeated over different ROI options.

Significance For Varying Cutoffs (MBR = 720.0, PIFGAR = 2.0, RCUT = 100.0, MVA Type = NN)



130

Figure B.3: Event selection optimization grid scan results for NN estimator, optimizing for Asimov significance approximation. Asimov significance in Z-axis. Text within boxes shows signal events (red) and background events (black). The y-axis is the NN score, while the x-axis is the random forest score (in this case set to -2 for omission) repeated over different ROI options

# Appendix C

## Systematic Variation Shape Analysis for Dust Alphas

Section 6.2 includes calculating the amount of each alpha event in the dark matter search region of interest for a given livetime. Part of this analysis includes incorporating the effect of systematic variations on the RAT simulation software in the uncertainties of the estimate. This was done in different capacities for all three alpha sources. The systematic variations considered are listed in Section 4.2.2.

In the case of dust alphas, new sets of simulated samples are generated for each variation. The resulting estimate with these new samples are considered a systematic uncertainty on the yield, and are combined together for all variations. To fully explore these samples, they are plotted in  $F_{\text{prompt}}$ , PE, and reconstructed R space, and compared to the original, nominal sample. These comparisons are plotted here, with the low-level and positional cuts applied (see Table 6.2). In the end all variations behave as expected, with no major changes.

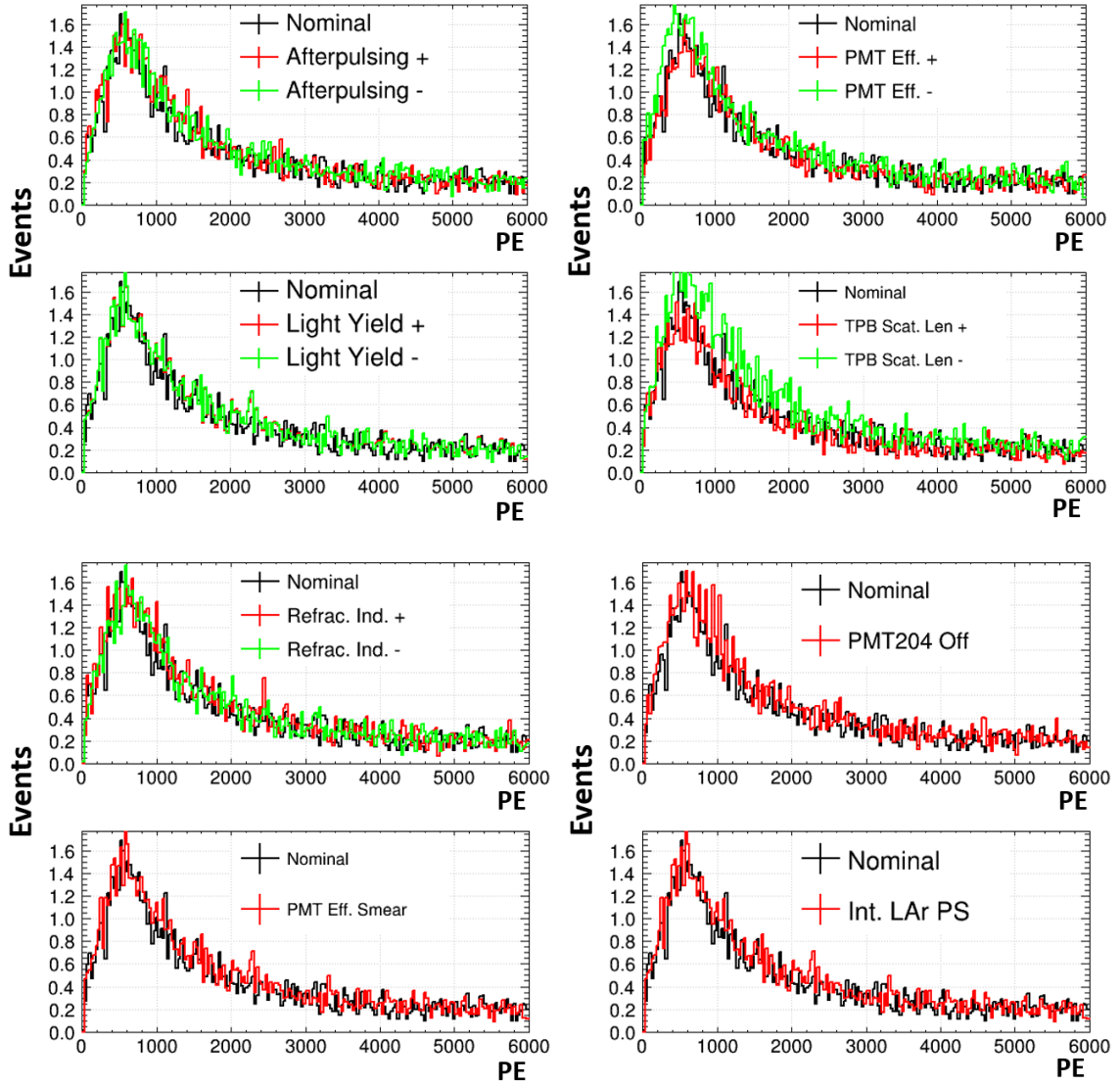


Figure C.1: Comparison of nominal (black) to systematic variations (red/green) for PE, scaled to the expected number of triggers over the 3 year live time for each systematic. Shapes match when normalized. Only noticeable change from reducing TPB scattering length, which is accounted for in estimate.

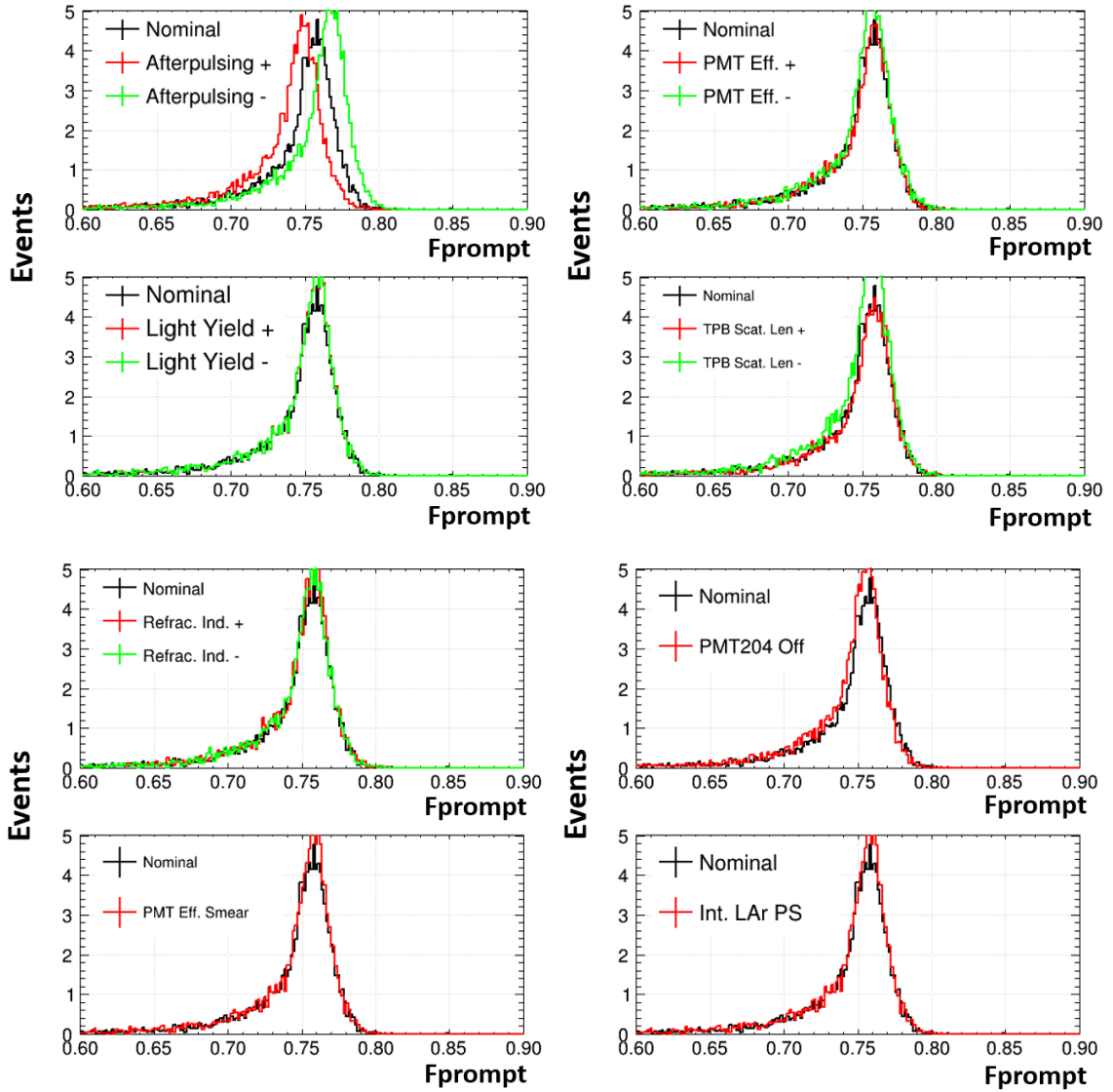


Figure C.2: Comparison of nominal (black) to systematic variations (red/green) for  $F_{\text{prompt}}$ , scaled to the expected number of triggers over the 3 year live time for each systematic. Shapes match when normalized. Only noticeable change from reducing TPB scattering length, which is accounted for in estimate.

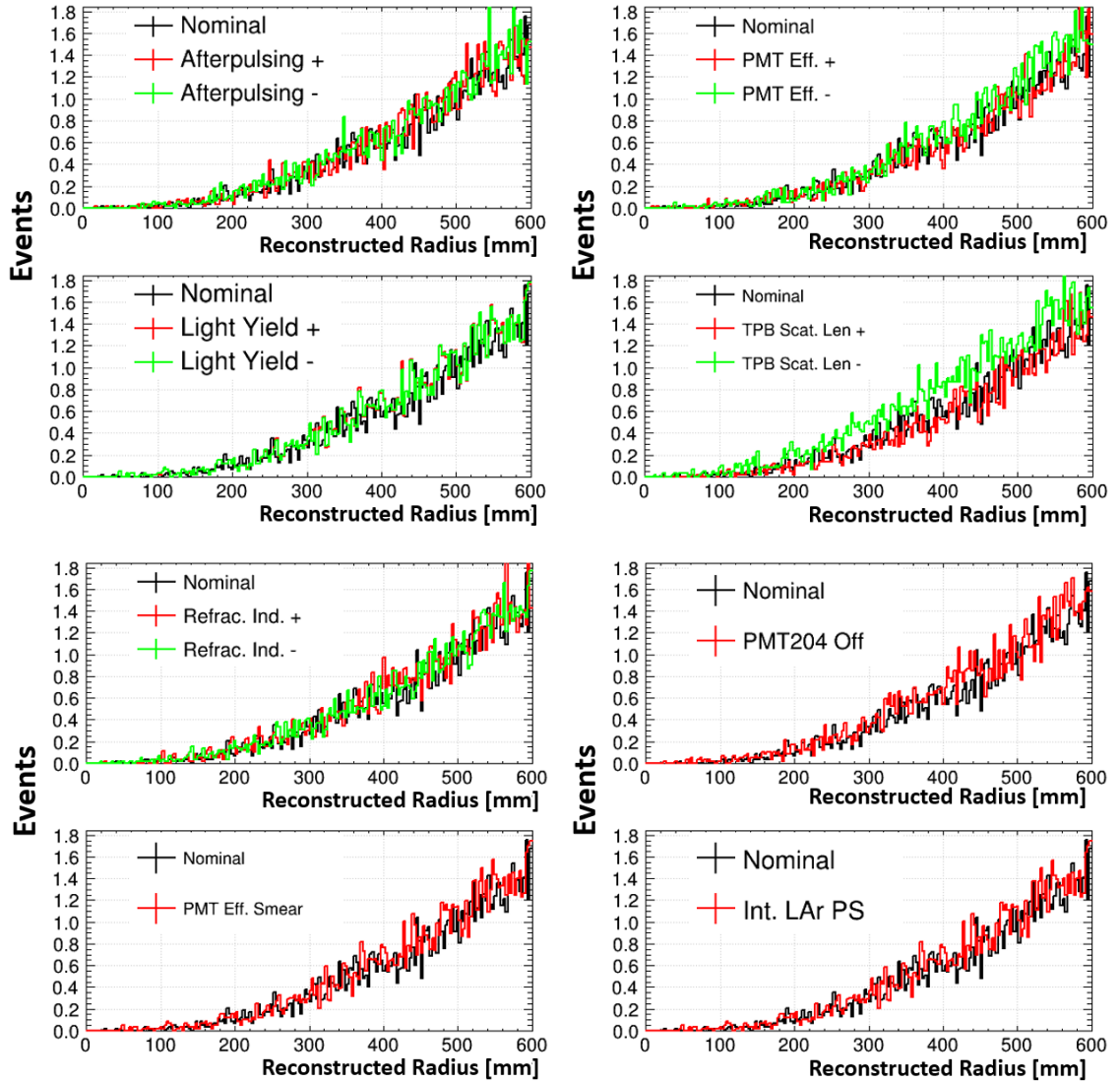


Figure C.3: Comparison of nominal (black) to systematic variations (red/green) for reconstructed radius, scaled to the expected number of triggers over the 3 year live time for each systematic. Shapes match when normalized. Only noticeable change from reducing TPB scattering length, which is accounted for in estimate.